STRUCTURE OF PARTIALLY PREMIXED FLAMES USING DETAILED CHEMISTRY SIMULATIONS

A Dissertation

by

CELINE DELPHINE KLUZEK

Submitted to the Office of Graduate Studies of
Texas A&M University
in partial fulfillment of the requirements for the degree of

DOCTOR OF PHILOSOPHY

August 2009

Major Subject: Aerospace Engineering

STRUCTURE OF PARTIALLY PREMIXED FLAMES USING DETAILED CHEMISTRY SIMULATIONS

A Dissertation

by

CELINE DELPHINE KLUZEK

Submitted to the Office of Graduate Studies of
Texas A&M University
in partial fulfillment of the requirements for the degree of

DOCTOR OF PHILOSOPHY

Approved by:

Chair of Committee,	Adonios N. Karpetis
Committee Members,	William S. Saric
	Othon Rediniotis
	Don Collins
Head of Department,	Dimitris Lagoudas

August 2009

Major Subject: Aerospace Engineering

ABSTRACT

Structure of Partially Premixed Flames Using Detailed Chemistry Simulations.

(August 2009)

Celine Delphine Kluzek, B.S., Florida Institute of Technology;

M.S., Purdue University

Chair of Advisory Committee: Dr. Adonios N. Karpetis

State-of-the-art reacting-flow computations have to compromise either on the detail of chemical reactions or on the dimensionality of the solution, while experiments in flames are limited by the flow accessibility and provide at best a limited number of observables. In the present work, the partially premixed laminar flame structure is examined using a detailed-chemistry, one-dimensional simulation. The computational results are compared to unpublished single-point multiscalar measurements obtained at Sandia National Labs in 2001. The study is focused on axisymmetric laminar partially-premixed methane/air flames with varying premixture strength values of 1.8, 2.2, and 3.17. The combination of computational and experimental results is used to analyze the spatial and scalar flame structure under the overarching concept of flamelets. The computations are based on the Cantera open-source software package developed at CalTech by D. Goodwin, and incorporating the GRI 3.0 chemical kinetic mechanism utilizing 325 chemical reactions and 53 species for methane combustion. Cross-transport effects as well as an optically-thin radiation model are included in the calculations. Radiation changes the flame profiles due to its effect on temperature, and the attendant effects on a number of species. Using the detailed analysis

of different reaction rates, the adiabatic and radiative nitric oxide concentrations are compared. The cross-transport effects, i.e. Soret and Dufour, were studied in detail. The Soret term has a small but important effect on the flame structure through a reduction of the hydrogen mass fraction, which changes the conserved scalar values. Based on the flamelet approach and a unique formulation of the conserved scalar, the flame thermochemistry can be analyzed and understood. A number of interesting effects on the flame thermochemistry can be discerned in both experiments and computations when the premixture strength is varied. An increase in premixing results in a counterintuitive decrease in intermediate species such as carbon monoxide and hydrogen, as well as an expected increase in nitric oxide concentrations. Good agreement is found between experiments and calculations in scalar space, while the difference in dimensionality between axisymmetric measurements and opposed jet computations makes comparison in physical space tentative.

To Felix and Regine

ACKNOWLEDGMENTS

The completion of this work would not have been possible without the support and enthusiasm of Adonios Karpetis. He always showed great interest in every detail of the research and helped me build a great understanding of the physics of the problem. Always encouraging, pushing for better results, he never showed temper. His dedication towards fundamental research and to the transfer of knowledge to his students inspired me.

I would like to recognize here my first godfather, William Saric, who encouraged me in the pursuit of a Ph.D. degree. Without his support, his integrety, I would not be the engineer that I am today. I would like to thank him and his wife, Helen Reed, for their kindness, for giving me so many opportunities and so many responsibilities. I also would like to thanks Don Collins for his involvement. His door was always open to share his knowledge of the field of Atmospheric Science. I learned precious skills with the inter-discipllinary research project performed under his guidance. I also would like to thanks Othon Rediniotis for his sharp questions and valuable comment to improve the quality of this work. His teaching and wits, will always be remembered. I will always be thankful to Mike Nolan and Steve Heister, professors at Purdue University, for their encouragement to pursue this path and for the role models they are to me.

This thesis contains the inputs from two experimentalists: Adonios Karpetis and Robert Barlow. I would like to thanks both of them for providing the results of extensive experiments performed at Sandia National Laboratories. It's the combination of data and computations that made this thesis possible.

I thank my family for their unconditional love and support. Finally, I would

like to recognize the team of graduate students with which I worked. All had an important role as friends, supporters or even critics who made this work only better: Andrew Carpenter, Shane Schouten, Adam Johnson, Alex Bayeh, Tetsu Nakamura, Tyler Neale, Shalom Johnson, Crystal Reed and Andy Glen, Nicole Donato, Mike Belisle, and Cecil Rhodes. I will never forget the lessons learned at the Flight Research Lab and with the combustion research's team. They improved the quality of my work and will continue to do so.

This work was supported by A.F.O.S.R. (FA9550-081-0333) and program manager John D. Schmisseur.

TABLE OF CONTENTS

Page

Page

LIST OF TABLES

LIST OF FIGURES

FIGURE Page

FIGURE Page

FIGURE Page

NOMENCLATURE

A_K	Arrhenius pre-exponential factor
a	Cold strain rate, s^{-1}
$a_{p,i}$	Planck's absorption coefficient of species i
C_j or N_i	Concentration of species j, mol/m^3
c_p	Specific heat at constant pressure, kJ/(kg K)
$D_{T,i}$	Thermal diffusion coefficient, m^2/s
$D_{i,j}$	Multicomponent diffusion coefficient from species i to j, m^2/s
$\mathcal{D}_{i,j}$	Binary diffusion coefficient from species i to j, m^2/s
$D_{i,mix}$	Mixture-averaged diffusion coefficient of species i into the mixture, m^2/s
E_a	Activation energy, kcal/mol
e	Internal energy, Watts
$\bar{f}_i$	External force on species i, kg m/s^2
h	Total enthalpy, kJ/kg
h^s	Sensible/thermal enthalpy, kJ/kg
h_i^o	Formation enthalpy, kJ/kg
k_b	Reaction rate backward, kmol/(m^3s)
k_f	Reaction rate forward, kmol/(m^3s)
K_c	Equilibrium constant
K_p	Equilibrium constant based on component pressure (ideal gas)
$Le_{i,j}$	Lewis number
MW_i	Molecular weight of species i, kg/kmol

M	Mach number
M_o	Reference Mach number
M_i	Molecule or species i
$\bar{\bar{P}}$	Pressure tensor
p	Pressure, atm
p_o	Reference pressure, atm
$\widehat{p}$	Normalized pressure, atm
q_k	Heat of reaction k, J/kg
$\bar{q}$	Heat flux, W/m^2
$\bar{q_r}$	Radiative heat flux, W/m^2
R^o	Ideal gas constant, 8314 J/(kmol K)
Re	Reynolds number
T	Temperature, K
$\bar{u}$	Flow velocity, m/s
u_o	Reference Velocity, m/s
$\widehat{u}$	Normalized velocity, m/s
u	Velocity component in the z plane
v	Velocity component in the r plane
V	Scaled velocity, s^{-1}
$\bar{V_i}$	Molecular velocity, m/s
$\bar{v_i}$	Individual or peculiar velocity of species i, m/s
X_i	Mole fraction of species i
Y_i	Mass fraction of species i

z or d	Distance, m
(r, z)	Axisymmetric coordinates

Symbols

α_o	Cold strain rate, s^{-1}
α	Thermal diffusion coefficient, m^2/s
γ	Ratio of specific heats, c_p/c_v
Γ_i	Mass diffusion
Γ_s	Soret effect
ϵ	Emissivity
$\pounds$	Linear operator
λ	Thermal conductivity, W/(mK)
μ	Dynamic viscosity, kg/(m s)
ν	Kinematic viscosity, m^2/s
ν_j'	Stoichiometric coefficient of reactant species j
$\nu_j^{"}$	Stoichiometric coefficient of product species j
ϵ or Z_H	Conserved scalar
ρ	Density, kg/m^3
$\widehat{\rho}$	Normalized density, kg/m^3
ρ_o	Reference density, kg/m^3
σ	Stefan Boltzman constant, 5.6704 $\times 10^{-8} W/(m^2 K^4)$
ϕ	Equivalence ratio
ξ	Scalar dissipation, s^{-1}

Ψ	Stream function
ω'_k	Progress of reaction variable for reaction k, kmol/(m^{3}s)
$\widehat{\omega}_{i,K}$	Molar reaction rate of species i for reaction k, kmol/(m^3 s)
$\widehat{\omega}_i$	Molar production/destruction rate of species i, kmol/(m^3 s)
$\dot{\omega}_k$	Net mass production/destruction rate of species i, kg/(m^3 s)

Subscript

b	Indicates background property
i	Indicates species i from 1, 2, 3 ... to N
k	Indicates reaction k from 1, 2, 3 ... to M
$fuel$	Defines fuel property
ox	Defines oxidizer property

CHAPTER I

INTRODUCTION

Reacting flows in practical applications such as burners, powerplant combustors, or aircraft engines are often complex in nature. Such engineering systems combining unsteady, turbulent or rotating flows with multiple chemical reactions are difficult to study experimentally as well as computationally. Researchers are limited by the physical enclosure of combustion chambers and the use of non-intrusive measurement techniques. Even with the latest laser diagnostic systems, experiments are resolved in one dimension sometimes in two dimensions and the number of species studied is limited. The complexity of reaction mechanisms makes the 2-dimensional (2-D) and 3-dimensional (3-D) simulations unaffordable with present day computational capabilities, while detailed-chemistry calculations in one spatial dimension (1-D) are easily achieved. Combustion researcher have to compromise either on the dimensionality of the problem or the detail of the chemical kinetics.

At the same time, experimental investigation of reacting flows in a closed combustion chamber is only possible with the use of complicated and expensive laser diagnostics, which gives at best 1-D or 2-D results and provides information on a limited number of species. At present, detailed-chemistry simulations in two dimensions are rarely attempted (e.g. Bennett et al. (2000)). In order to understand combustion and optimize the process for more efficient, cleaner automotive and aircraft engines, scientists have to compromise either on the dimensionality of the problem or the detail of the chemical kinetics. Without the hindrance of enclosures and windows, the

---

The journal model is *Combustion Science and Technology*.

fundamentals of combustion can be studied in open air using the existing state of the art measurement techniques in simpler laboratory flames.

Although what follows is not an exhaustive review, some previous literature concerning experiments, simulations, and theory of flames will be discussed here as background for the present work. Some of the first experiments on laminar flames were performed by Yamaoka and Tsuji in the late 70s (Yamaoka and Tsuji, 1974, 1976). While studying flammability limits of partially premixed methane-air flames, they were the first to mention a double flame, i.e. the flames portrayed two distinct combustion zones, a subject that will be discussed in later chapters. Numerous experiments on laminar as well as turbulent flames were also performed over the years at the Combustion Research Facilities[1] (CRF). Noticeably, Tsuji burner experiments were performed in 2001 by Barlow et al. (2001) to study partially premixed methane-air flames. The authors applied multi-scalar laser diagnostic techniques to measure major and some minor species. Experimental results which included nitric oxide (NO) were compared to detailed chemistry computations using Chemkin (Kee and Miller, 1978).

Most often, experiments are used to validate the computational calculations. Development of the latter involves the precise understanding of detailed-chemistry mechanisms. As explained in Glassman (1996) the results of these studies enabled the understanding of initiation, oxidation, branching and termination reactions, and the tabulation of reaction-rate parameters for various fuels. Several researchers have tried to minimize the number of chemical reactions used in the simulations in order to reduce the computational time. Westbrook and Dryer (1981) were the first to

[1]The Sandia National Laboratories CRF is funded by the Department of Energy. It furthers research in basic as well as applied combustion science and technology.

systematically develop reduced chemical mechanisms for various hydrocarbon fuels[2]. Work by Seshadri and Peters (1990) examined the structure of partially premixed methane flames using a four-step reaction mechanism. Among others, Xue and Aggarwal (2001) investigated the effects of various reaction mechanisms on the structure of partially premixed methane-air flames. More recently, Sutton and Fleming (2008) modified the GRI 3.0 (Smith et al., Accessed July 2008) reaction mechanism to include several more reactions leading to NO formation. The simulations were performed with ChemKin using a burner stabilized flame configuration with a premixed methane-air system. Their calculations were compared to experimental data from other studies such as Berg et al. (2000); Pillier et al. (2005); Gasnot et al. (1999); Williams and Fleming (2007); Van Essen et al. (2007).

Efficiency and pollutant emission control for engines is also a primary objective for a lot of combustion studies, driven by the increasing regulations on automotive and aircraft engine exhausts. A consequential work by Li and Williams (1999)[3] used partially premixed methane-air flames to study a two stage combustion process. By adding water or carbon dioxide to the partially premixed methane flames, a reduction in NO was achieved for certain equivalence ratios. This work used ChemKin and a chemistry mechanism including 31 elementary steps and 177 reactions, adapted from earlier studies (Rightley and Williams, 1997). An optically-thin radiation model including emission of CO_2 and H_2O was used.

During the last decade the scientific community, guided by the International workshop on measurement of Turbulent Non-premixed Flames (TNF), investigated the effect of radiation in flames in an attempt to improve the numerical simulations.

---

[2]Lawrence Livermore National laboratory, California, and the Department of Mechanical and Aerospace engineering at Princeton University respectively.

[3]University of California, San Diego, La Jolla.

Radiation emission and self-absorption in flames were studied in detail by Zhu et al. (2002) in partially premixed methane-air flames. The calculations were compared to Tsuji-type flame experiments from Sandia (Barlow et al., 2001). An important study of radiative transfer in premixed flames was conducted by Daguse et al. (1996). During that work two types of non-premixed flames were studied in detail, namely H_2-O_2 and propane-air systems. Work at Purdue University, e.g. Kim et al. (2003), studied non-premixed and partially premixed opposed jet flames. Using an optically-thin radiation model that accounts only for emission they proved that self-absorption had a negligible effect on flame structure even at low strain.

To investigate the effect of gravity and radiation in non-premixed methane flames Charest (2008) used the Cantera thermodynamic transport and chemical managers into a solver for the governing equations that was developed in-house. The reaction mechanism used, i.e. GRI 3.0, was modified to 219 equations and 36 species and excluded the NO reaction pathway. The solution was found with a 2-D scheme and in many respects this study points to a possible continuation of the present work.

The capabilities of software packages such as ChemKin and Cantera are constantly improved, more recently with the inclusion of kinetics for soot formation. This is due to a combination of increasing regulation and advances in computational capabilities to treat more complex systems. Several recent studies at Stanford University concentrated on soot formation and its inclusion in reacting flow simulations of turbulent flames for fire suppression (Pepiot-Desjardins et al., 2008; Pitsch et al., 2009; Blanquart et al., 2009; Mueller et al., 2009). A group from University of Michigan Ann Arbor (Mungekar and Atreya, 2006) investigated soot emission and NOx levels in partially premixed methane flames in an opposed-jet configuration. More recently, Dworkin et al. (2009) used numerical simulations to analyze the effect of thermal diffusion on soot formation in ethylene-air flames.

In an attempt to include more physical effects in the reacting flow simulations, a number of studies examined thermal diffusion and cross-transport effects in flames (Vranos and Hall, 1993; Pitsch and Peters, 1998; Rosner et al., 2000; Palle et al., 2005). The work of Grçar et al. (2008) continued this line of research with calculations of lean premixed hydrogen-air propagating flames.

A brief review of the literature shows that hydrogen-fuel related research is prominent in the field. The reason behind this is the simplicity of the hydrogen oxidation reactions compared to hydrocarbon fuels. For example, twenty reactions suffice to capture hydrogen combustion while the simulations of the simplest hydrocarbon fuel, methane, may require more than tree hundred. Despite rapid advances in computer development, present-day combustion researchers still have to compromise between a complete reaction mechanism which is currently feasible only in 1-D and a skeletal or reduced chemical mechanism in more than one spatial dimension.

The group at Yale University (Smooke et al., 1992) made a consequential contribution on methane-air flames by computing, for the first time, a non-premixed laminar flame in two dimensions. Ern and Giovangigli (1998) investigated the cross-transport effects and thermal diffusion using 2-D calculations. At that time, a low-level kinetics mechanism was used that included only hydrogen and oxygen bearing species. The more recent studies by (Bennett et al., 2000) used a similar simplified reaction mechanismto compare calculations with experiments of axisymmetric coflow partially-premixed methane-air flames. The latest two dimensional computational research was performed by Grçar et al. (2008) who studied axisymmetric jet flames in two dimensions, as well as Dworkin et al. (2009) who studied soot formation in ethylene flames including thermal diffusion and multicomponent ransport[4].

[4]Ethylene chemistry was studied using the modified GRI mechanism previously used by Sung et al. (1996).

The Cantera software package that will be used in the present study has also been used in the past for the calculation of various reacting flows. Work at California Institute of Technology by Bergthorson (2005) and Benezech (2006) used the code for jet impinging reacting flows. Bergthorson (2005) used experimental data to validate certain reaction mechanisms with premixed methane-air, ethane-air and ethylene-oxygen-nitrogen flames. The San Diego mechanisms (Williams, Accessed March 2008) were compared to GRI 3.0 (Smith et al., Accessed July 2008) and the C_3-Davis mechanisms (Davis et al., 1999). Later Benezech (2006) researched the extinction of planar methane-air flames with the same three reaction mechanisms, this time including a variation in premixture strength. Bergthorson compared experimental results from particle-streak velocimetry and planar laser-induced fluorescence to the Cantera calculations (Bergthorson et al., 2005a,b; Bergthorson and Dimotakis, 2007). Cantera is an open source software package recently developed and yet rarely used in research publications. The aforementioned publications from Caltech and the following studies are the only ones currently available: a proton-exchange membrane hydrogen fuel cell (Shields, 2007); a catalytic converter application (Arrighetti et al., 2007); and the previously cited work in 2-D microgravity flames (Charest, 2008).

To the best of my knowledge this study represents the first time Cantera is used to compare detailed-chemistry calculations to multi-scalar experiments of laminar axisymmetric flames from Sandia Nat'l Labs. Partially premixed methane-air flames were chosen in order to contribute to the literature where simulations including both radiation and cross-transport effects are lacking. The state-of-the-art software package provides a chemical manager that can use detailed chemical kinetics, such as GRI 3.0, with 53 species and 325 reactions, and an advanced transport manager for multi-component diffusion. I augmented the calculations with an optically-thin radiation model using emission from only four species (CH_4, H_2O, CO, CO_2). In order to com-

plete the full transport properties calculation, I included the higher order Soret and Dufour terms. The main novelty of the present work lies in the detailed-chemistry calculations including radiation and higher order cross-transport effects. Although the physical problem is solved in one dimension the experimental data are two dimensional. Indeed, the dimensionality of the axisymmetric flames will be discussed in later chapters and future work will include a boundary-layer 2-D scheme using detailed-chemistry and full transport.

In the present work, the theory of flamelets will also be discussed. The flamelet approach enables the examination of the scalar flame structure and its characteristics. It was originally developed for the understanding of turbulent flames. The flamelet mappings were introduced in combustion by Peters (1984, 1998, 1988) based on theoretical developments by Bilger (1976a,b, 2000). Pitsch and Peters (1998) studied laminar non-premixed hydrogen-air flames using transient flamelets. Unsteady flamelet models have also been used to simulate turbulent non-premixed jet flames and to compared with experimental results (Pitsch and Steiner, 2000; Pitsch et al., 2009). The results of the former study showed that the conditional statistics in the turbulent flow field (temperature and mass fractions) were strongly dependent on the level of partial premixing in the flame. Motivated by this finding, the present work will utilize the flamelet approach to analyze the flame scalar structure under varying premixture.

Partially premixed flames have attracted a lot of attention because they combine some of the positive aspects of both premixed and non-premixed flames. The choice of partially premixed flames will be explained in more detail in the first chapter. The experimental data set will then be introduced. The physics of the reacting flow and the governing equations will be discussed, followed by the subset of equations pertinent to the 1-D opposed jet flames. The software package, as well as the modifications to

the existing code will be described. Lastly, the results of simulations and experiments are divided in two chapters: the spatial and scalar structure of the flame. The effects of radiation and cross-transport will be discussed. The novelty of this study is based on the fact that for the first time high-quality multi-scalar measurements in partially premixed flames are compared to accurate Cantera calculations in 1-D.

CHAPTER II

LAMINAR PARTIALLY PREMIXED METHANE-AIR FLAMES

Experiments are easier to set up as open system compared to a closed, complex-geometry, 3-D combustion system such as an engine combustion chamber. The different type of flames are obtained with different geometrical arrangements, and the manner of mixing between fuel and oxidizer. This results in various thermodynamic properties and velocity for each flame type. The flames may be premixed or non-premixed, laminar or turbulent. The specific subject of the present work is laminar partially premixed methane-air flames. I will explain the choice of partially premixed flames. Briefly, I will introduce the experimental apparatus, data set and laser diagnostics used on laminar flames at Sandia National Laboratories. Finally, I will explain the one-dimensional flame representation.

Non-premixed versus premixed flames

There are different reasons to choose a partially premixed flame over a non-premixed or premixed flame. As seen in figure 1, non-premixed flame, the fuel stream comes from the center of a burner, nozzle[1] and air takes the role of oxidizer supplied by entrainment or by a co-flowing stream. The ignition is usually produced by an initial spark at the base of the stream and then the flames are self-sustained. The reaction zone (represented by a red line in figure 1) is located around the maximum temperature where the fuel and air react at the stoichiometric value. The oxidizer/air concentration is decreasing from the outside towards the flame front while the fuel

[1] A candle is an example of a non-premixed flame where the wax is the fuel.

concentration is decreasing from the center of the stream to meet in the reaction zone where the product concentration peaks.

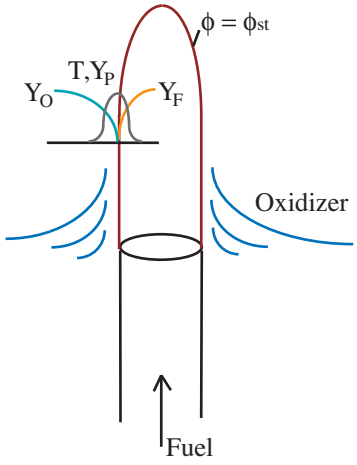

Figure 1. Non-premixed flame schematic.

In figure 1, Y's represent mass fraction, $m_i/\sum m_i$, where m_i is the mass of species i over the total mass. To characterize the richness of the flame, the equivalence ratio or premixture strength is defined as:

$$\phi = \frac{(Fuel/Air)}{(Fuel/Air)_{stoichiometric}} \tag{2.1}$$

Represented in Figure 2, are the two other types of flames. In the premixed flame, case c, fuel and oxidizer are mixed together at the molecular level before ignition. The best example of premixed flames is found in the carburetor engines. The partially premixed flame set up, case b, is achieved by premixing fuel and oxidizer before ignition and adding oxidizer/air by entrainment or with a co-flow. It combines some of the advantages of non-premixed and premixed flames:

- Robustness: the partially premixed flame is slightly more robust than the non-

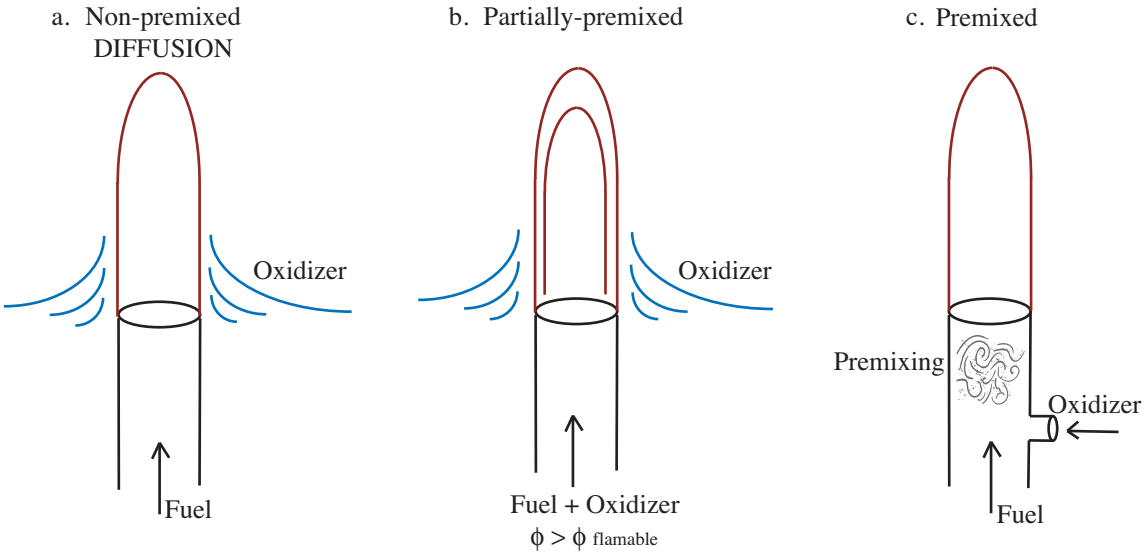

Figure 2. Flame types classification.

premixed flame. The non-premixed flame has heat loss both towards the oxidizer and the fuel side. It is easily extinguished. While the premixed flame is considered more robust than the non-premixed system because the heat loss is directed only towards the fuel side.

- Economy: in a laboratory, a careful variation of the fuel and air mass flows is necessary in order to stay within the flammability limits of the non-premixed flame. This process is not economical. In contrast the premixed and partially premixed set up can achieved a better fuel economy.

- Safety: the partially premixed flames are considered safer than the premixed flames which are susceptible to backfire, when the flame front reaches back to the fuel source.

The fundamental difference between the three flames is the equivalence ratio, ϕ. For a partially premixed flame, ϕ is too rich and above the rich flammability interval

of a premixed flame. For example the flammability limit for methane-air combustion is experimentally determined in the range: $0.53 < \phi < 1.6$ (Glassman, 1996). If a premixed flame is set up with an equivalence ratio of 1.8, with a co-flow of inert gas such as Argon, the mixture would not burn. But if the same flame allows for air entrainment it will survive. The richness of the mixture creates a special condition for a second reaction zone in the flame. In the even more advanced configuration where fuel is injected in the co-flow three reaction zones appears, giving rise to the triple flame structure introduced by Plessing et al. (1998); Aggarwal et al. (2001); Qin et al. (2004). The second reaction zone is represented here in Figure 2b by the second red line lying inside the line of stoichiometric value, in the rich zone. The careful examination and detailed understanding of this second reaction zone are some of the major motivating factors for the present study.

As explained by (Xue and Aggarwal, 2001) partially premixed flames are relevant and useful for engine combustion since "a partially premixed flame is capable of achieving both high-energy supply and low pollutant emissions simultaneously".

The choice of methane as fuel is motivated by the scientific community understanding of the methane oxidation characteristics. Methane reaction mechanisms are fairly well modeled[2] compared to more complex higher order hydrocarbons. Although hydrogen fuel would be simpler to model and analyzed, experimentalist prefer using methane for its minimal soot formation.

Experimental approach

The following section will describe the laboratory experiments to obtain laminar flames and the chemical species measured. Experiments were conducted at the Com-

[2]Certain reaction mechanisms are still under investigation such as higher order hydrocarbon formation, cabonaceous chains C-1 to C-6, and oxidation mechanisms.

bustion Research Facilities (CRF), Sandia National Laboratories by Karpetis and Barlow (2003); Kluzek, Karpetis and Barlow (2009). A previously unpublished data set will be used in the present work for comparison with the numerical calculations.

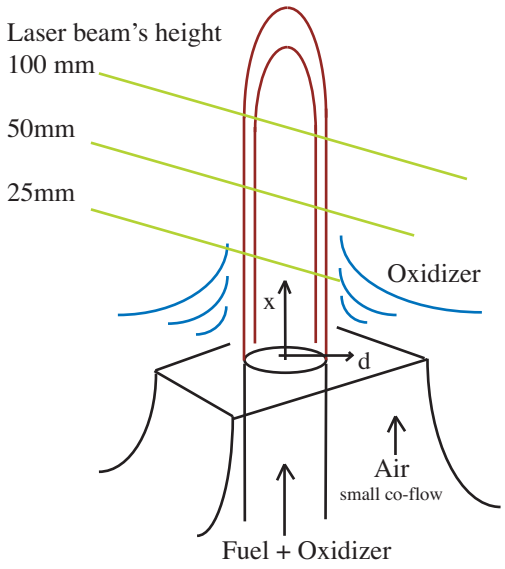

Figure 3. Schematic of laminar flame experimental set up used in Sandia Nat'l Lab.

Table I. Flow parameters of the three jet flames used in the present study

ϕ	Air-in-Fuel (slm)	Fuel (slm)	Co-flow (slm)
1.80	6.73	1.27	0.9
2.20	6.50	1.50	0.9
3.17	6.00	2.00	0.9

Figure 3 is a schematic of the generic experimental set up used in Sandia for measurements in laminar axisymmetric flames. In the original experimental set up,

the annular piloted burner had a main jet diameter of 7.72 mm. The jet was located in the center and slightly above the exit of a wind tunnel of section 30x30 cm (exit of a contraction ratio of 9:1). The jet velocity was in the order of 2 m/s, and the co-flow velocity approximately 0.9 m/s. The volumetric flow-rates issuing from the nozzle exit are listed in Table I. The purpose of the co-flowing air was to stabilize the flame, by reducing the variation or flickering of the flame-tip. The flames were attached to the nozzle exit thus premixing with coflow air was negligible. The level of premixing (air-in-fuel) was accurately controlled by using mass-flow controllers to achieve equivalence ratios of $\phi = 1.8$, 2.2, 3.17 for the three flames under study. The cold Reynolds number for the jet was approximatively 1100, ensuring a laminar jet flow. More detail of the experimental set-up as well as a discussion of measurement accuracies can be found in Barlow et al. (2001, 2000).

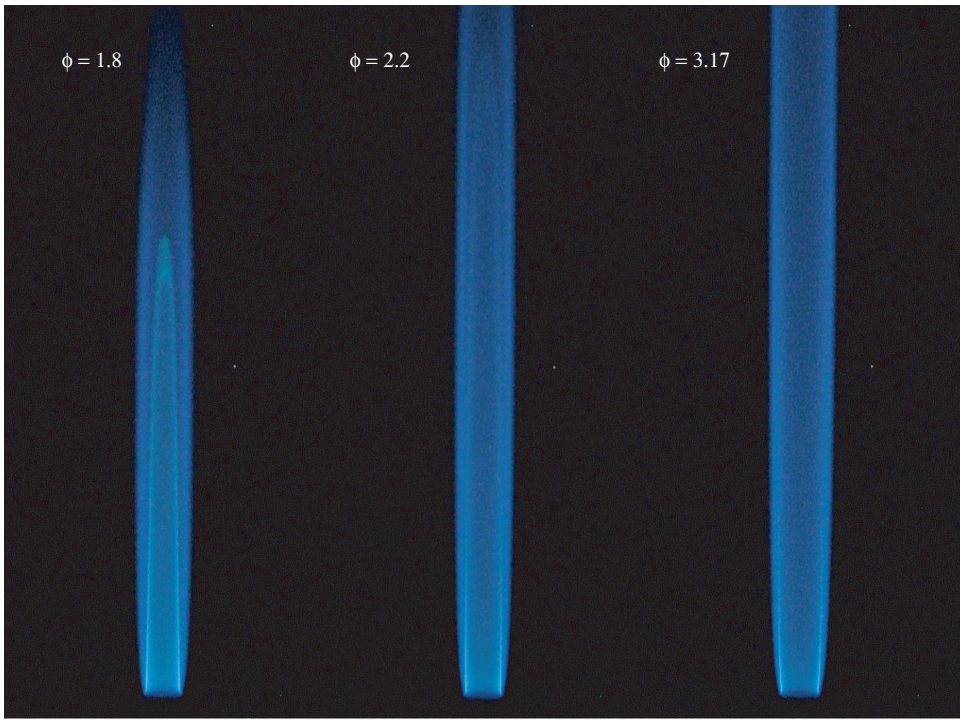

Figure 4. Photograph of Sandia laminar flames at varying premixing strength. With permission of Adonios Karpetis.

Figure 4 shows a composite image of chemiluminescence emanating from the three flames. The double zone structure, which will be discussed in Chapter IV is evident for both of the leaner flames ($\phi = 1.8, 2.2$).

The main limitation of experiments is the number of species that can be measured. A more complete picture of the combustion process can be obtained by using detailed-chemistry computations. The specific reaction mechanism used here, GRI 3.0 (Smith et al., Accessed July 2008), will give information on 53 species and 325 reactions simultaneously. It will enable the extraction of reaction rates and analysis of detailed thermochemistry.

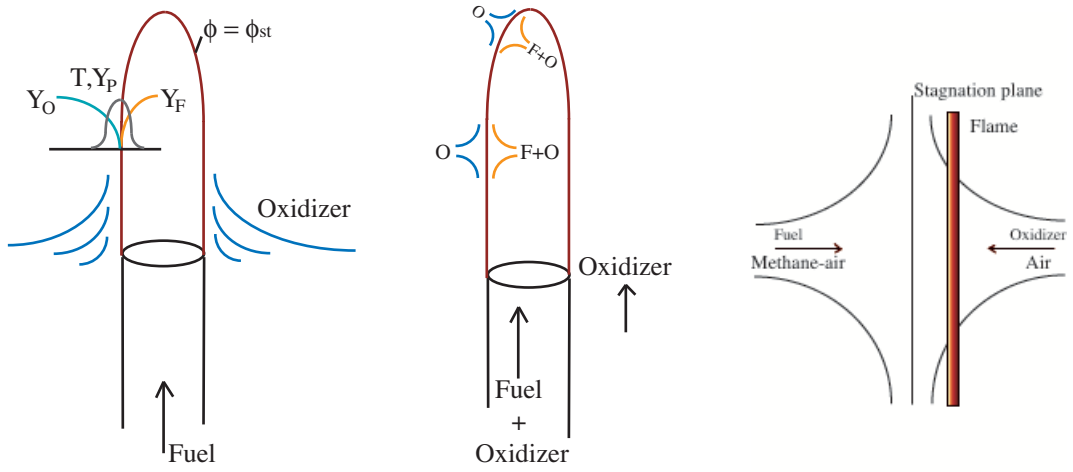

Figure 5. Flame representation in 1-D. The figure on the left represent an axisymmetric flame which contains several flames. The reaction can be seen as a fuel jet opposing an oxidizer jet, leading to the representation of the flame with an opposed jet flame.

A 2-D configuration is needed to increase the fidelity of the computations and to better match the experimental data . A 2-D treatment has been accomplished in the past by Smooke and co-workers, e.g. Bennett et al. (2000). Due to the computational cost of detailed chemistry calculation, skeletal mechanisms are often use instead. To keep the numerical solutions within runtime of one hour or less, a 1-D treatment

is preferred. As depicted by figure 5, oxidizer and fuel/air mixture face each other everywhere. As a result, the flame can be seen as a collection of laminar opposed jet flames. This assumption is valid locally but we will see in the results section how difficulties arise with this approach and investigate in more detail the differences and improvement possible with a 2-D simulation.

CHAPTER III

NUMERICAL CALCULATIONS

The opposed jet flow configuration takes advantage of the existence of a similarity solution which reduces the 2-D system to an 1-D problem. Numerically solving the reacting-flow equations in 1-D allows for the use of detailed chemistry and full transport in reasonable computational time. The physics and equations are described, and the numerical code and modifications are explained throughout the chapter. The calculations are augmented with a radiation treatment and the inclusion of cross-transport effect.

Reacting flow equations

In vector form, the conservation equations that apply to the general reacting flow are:
Mass conservation:

$$\frac{\partial \rho}{\partial t} + \nabla \cdot (\rho \bar{u}) = 0 \tag{3.1}$$

Species conservation:

$$\rho \frac{\partial Y_i}{\partial t} + \nabla \cdot (\rho \bar{u} Y_i - \rho D \nabla Y_i) = \dot{\omega}_i \tag{3.2}$$

where $\bar{u}$ is the flow velocity, Y_i the mass fraction, $\dot{\omega}_i$ the net mass production/destruction rate of species i, D the diffusion coefficient.
Momentum conservation:

$$\rho \frac{D\bar{u}}{Dt} = -\nabla \cdot \bar{\bar{P}} + \rho \sum_{i=1}^{N} Y_i \bar{f}_i \tag{3.3}$$

Energy conservation:

$$\rho \frac{De}{Dt} = -\nabla \cdot \bar{q} - \bar{\bar{P}} : \nabla \bar{u} + \rho \sum_{i=1}^{N} Y_i \bar{f}_i \cdot \bar{V}_i \tag{3.4}$$

where $\bar{\bar{P}}$ is the pressure tensor, $\bar{f}_i$ are external body forces, e the internal energy and $\bar{q}$ the heat flux vector. The presence of chemical reaction is denoted in the species equation by the source term $\dot{\omega}_i$. All of the reacting flow equations are implicitly affected through the change in density.

The caloric and thermal equations of state are respectively:

$$h = \sum_{i=1}^{N} Y_i h_i = \sum_{i=1}^{N} Y_i h_i^o + \sum_{i=1}^{N} Y_i h_i^s \tag{3.5}$$

$$P = \rho R^o T \sum_{i=1}^{N} \frac{Y_i}{MW_i} \tag{3.6}$$

For the present case the governing equations are specialized for a cylindrical coordinate system. The opposed jet configuration leads to an axisymmetric problem where the flow is considered in the (z,r) plane only (figure 6). The flow is assumed in steady state and isobaric. Figure 6 illustrates the opposed jet flow configuration.

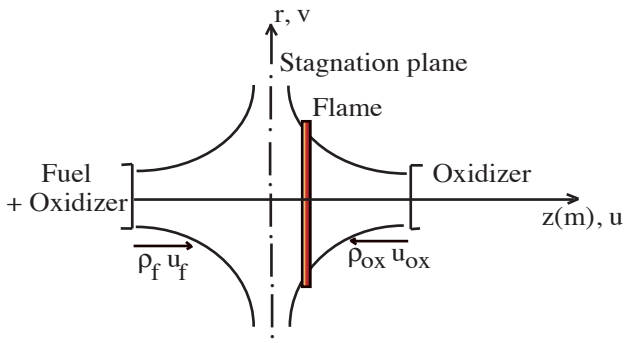

Figure 6. Schematic of opposed jet flow configuration. The flame is represented as an opposed jet where the stream of fuel impinges on a stream of air. A stagnation plane is formed in the center, when the mass flow are equal. The flame is located towards the oxidizer side.

The continuity equation becomes:

$$\frac{\partial(\rho u)}{\partial z} + \frac{1}{r}\frac{\partial(r\rho v)}{\partial r} = 0$$

where $(\bar{u}, \bar{v})$ are the two components of velocity in the (z,r) plane. As explained in the literature, e.g. Kee et al. (2003), a streamfunction can be defined for the flow field in cylindrical coordinates:

$$\Psi(z, r) = r^2 U(z)$$

where U is an unspecified function of z alone. The stream function has to satisfy the definition $d\Psi = 0$. Thus two relationship are obtained:

$$\begin{aligned} \frac{\partial \Psi}{\partial r} &= \rho u r = 2rU(z) \\ -\frac{\partial \Psi}{\partial z} &= \rho v r = -r^2 \tfrac{\partial U}{\partial z} \end{aligned}$$

These relationships are used in the radial momentum equation, which is then combined with the continuity equation, and after some simplifications[1], the momentum equation becomes an eigenvalue problem for the pressure curvature. The term $\partial p/\partial z$ is a function of z alone so its radial derivative must vanish:

$$\frac{\partial}{\partial r}\left(\frac{1}{r}\frac{\partial p}{\partial z}\right) = \frac{\partial}{\partial z}\left(\frac{1}{r}\frac{\partial p}{\partial r}\right) = 0 \quad \Longrightarrow \quad \frac{1}{r}\frac{\partial p}{\partial r} = \Lambda_r \tag{3.7}$$

Derivation of the 1-D equations

The preceding derivation leads to a significant simplification of the reacting flow equations from two dimensions to one dimension. The similarity solution is an exact solution of the stagnation flow problem. The final equations for this configuration read as follows:

[1]For more detail on the derivation see Kee et al. (2003), chapter 6.2.

Mass conservation:

$$\frac{d(\rho u)}{dz} + 2\rho V = 0 \tag{3.8}$$

From this point on, the physical velocities are function of z alone and the vector signs are omitted: u the flow velocity, and V a scaled velocity which is related to strain by equation 3.8.

$$V(z) = \frac{u}{r} \tag{3.9}$$

Species Conservation:

$$\rho u \frac{dY_i}{dz} = -\frac{d}{dz}(\rho Y_i V_i) + \dot{\omega}_i \tag{3.10}$$

where V_i is the molecular or diffusion velocity of species i (V_i is the magnitude of $\bar{V_i}$) which is defined as the peculiar velocity minus the flow velocity (Williams, 1985; Law, 2005):

$$\bar{V_i} = \bar{v_i} - \bar{u}$$

The radial momentum equation is reduced to an eigenvalue problem:

$$\rho u \frac{dV}{dz} + \rho V^2 = \frac{d}{dz}(\mu \frac{dV}{dz}) - \Lambda_r \tag{3.11}$$

For chemically reacting flow the energy equation has the general vector form:

$$\rho \frac{De}{Dt} = -\nabla \cdot \bar{q} - \bar{\bar{P}} : \nabla \bar{u} + \rho \sum_{i=1}^{N} Y_i \bar{f_i} \cdot \bar{V_i} \tag{3.12}$$

where e is the internal energy, $\bar{q}$ the heat flux vector, $\bar{\bar{P}}$ the pressure tensor, $\bar{u}$ the mass-average velocity, $\bar{V_i}$ the molecular diffusion velocity, Y_i the mole fraction of species$i$, and $\bar{f_i}$ external body forces. In order to explain some of the assumptions used in this problem, a short derivation of the conservation of energy is given here to obtain the final scalar form used by the numerical calculation. The following derivation, is based on the nomenclature of Williams (1985) and following Law (2005). In the

present problem external body forces such as gravity are neglected. The contraction of the pressure tensor with the velocity gradient is replaced by:

$$\bar{\bar{P}} : \nabla \bar{u} = -p(\nabla \cdot \bar{u})$$

Based on the approximation of low speed flow, energy dissipation through viscous effect is assumed negligible. In the inviscid momentum equation:

$$\rho u \frac{du}{dz} = -\frac{dp}{dz}$$

Each variable is nondimensionalized by an equivalent reference value, e.g. $\widehat{u} = u/u_o$, to obtain:

$$\frac{\rho_o u_o^2}{p_o}(\widehat{\rho}\widehat{u}\frac{d\widehat{u}}{dz}) = -\frac{d\widehat{p}}{dz}$$

The Mach number is introduced as M = u/a where a is the isentropic speed of sound, $a_o^2 = \gamma p_o \rho_o$.

$$\gamma M_o^2(\widehat{\rho}\widehat{u}\frac{d\widehat{u}}{dz}) = -\frac{d\widehat{p}}{dz}$$

In low-speed subsonic flows, $M_o^2 \ll 1$, and the changes in pressure are of the same order as the Mach number squared, thus the pressure variation can be considered negligible when compared to temperature, density, and concentration variation (see Kee et al. (2003) for a detailed explanation).

$$\Delta\widehat{p} \sim O(M_o^2)$$

Using the enthalpy definition:

$$e = h - \frac{p}{\rho}$$

and the total derivative definition to separate $\rho De/Dt$ into two terms, the energy

equation becomes:

$$\begin{aligned} \rho\frac{\partial e}{\partial t} + \nabla\cdot(\rho\bar{u}e) &= -\nabla\cdot\bar{q} - p(\nabla\cdot\bar{u}) \\ \frac{\partial}{\partial t}(\rho h) - \frac{\partial p}{\partial t} + \nabla\cdot(\rho\bar{u}h) + \nabla\cdot(\bar{u}p) &= -\nabla\cdot\bar{q} - p(\nabla\cdot\bar{u}) \end{aligned}$$

Using the isobaric assumption one can prove after some rearrangement that:

$$\frac{\partial}{\partial t}(\rho h) + \nabla\cdot(\rho\bar{u}h) = -\nabla\cdot\bar{q}$$

The caloric equation of state defines the enthalpy as being composed of sensible and formation parts:

$$h = \sum_{i=1}^{N} Y_i h_i = \sum_{i=1}^{N} Y_i h_i^o + \sum_{i=1}^{N} Y_i h_i^s \tag{3.13}$$

The energy equation then becomes:

$$\frac{\partial}{\partial t}(\rho\sum_{i=1}^{N} Y_i h_i^o) + \frac{\partial}{\partial t}(\rho\sum_{i=1}^{N} Y_i h_i^s) + \nabla\cdot(\rho\bar{u}\sum_{i=1}^{N} Y_i h_i^o) + \nabla\cdot(\rho\bar{u}\sum_{i=1}^{N} Y_i h_i^s) = -\nabla\cdot\bar{q}$$

In order to eliminate some terms, the species conservation equation 3.10 is multiplied by h_i^o and summed over all species to obtain:

$$\frac{\partial}{\partial t}(\rho\sum_{i=1}^{N} Y_i h_i^o) + \nabla\cdot(\rho\bar{u}\sum_{i=1}^{N} Y_i h_i^o) = \sum_{i=1}^{N} h_i^o\dot{w}_i$$

Replacing the first and third term in the energy equation:

$$\frac{\partial}{\partial t}(\rho\sum_{i=1}^{N} Y_i h_i^s) + \nabla\cdot(\rho\bar{u}\sum_{i=1}^{N} Y_i h_i^s) = -\nabla\cdot\bar{q} - \sum_{i=1}^{N} h_i^o\dot{w}_i$$

In the present problem, for multi-component transport in which radiation is important, the heat flux vector can be written as:

$$\bar{q} = -\lambda\bar{\nabla}T + \rho\sum_{i=1}^{N} h_i^s Y_i\bar{V}_i + R^oT\sum_{i=1}^{N}\sum_{j=1}^{N}(\frac{X_j D_{T,i}}{W_i D_{i,j}})(\bar{V}_i - \bar{V}_j) + \bar{q}_r \tag{3.14}$$

This constitutive equation includes Fourier heat flux, heat transfer due to property variation, Dufour cross-transport term, and radiative heat flux respectively. The multi-component diffusion coefficients, $D_{i,j}$ and thermal diffusion coefficient $D_{T,i}$, as well as the Dufour effect, will be discussed in section . For the present derivation the Dufour term will be neglected.

Replacing $\bar{q}$ in the energy equation, the following form is obtained:

$$\frac{\partial}{\partial t}(\rho \sum_{i=1}^{N} Y_i h_i^s) + \nabla \cdot (\rho \bar{u} \sum_{i=1}^{N} Y_i h_i^s) = -\nabla \cdot (-\lambda \bar{\nabla} T + \rho \sum_{i=1}^{N} h_i^s Y_i \bar{V}_i + \bar{q_r}) - \sum_{i=1}^{N} h_i^o \dot{w}_i$$

Using the following assumptions:

- Steady state

- Species-independent specific heat: $c_{p,i} = c_p$

it leads to two identities:

$$\nabla h_i^s = \nabla h^s = c_p \nabla T \tag{3.15}$$

$$\sum_{i=1}^{N} Y_i \bar{V}_i = 0 \tag{3.16}$$

The energy equation then becomes:

$$\nabla \cdot (\rho \bar{u} h^s) = \rho \bar{u} c_p \nabla T = -\nabla \cdot (-\lambda \bar{\nabla} T + \bar{q_r}) - \sum_{i=1}^{N} h_i^o \dot{w}_i$$

After re-arranging the terms:

$$-\rho \bar{u} c_p \nabla T + \nabla \cdot (\lambda \bar{\nabla} T) - \nabla \cdot \bar{q_r} - \sum_{i=1}^{N} h_i^o \dot{w}_i = 0 \tag{3.17}$$

The first term is heat transfer due to convection. The second term is heat transfer due to conduction, or Fourier heat flux. The third term is molecular energy transfer due to enthalpy fluxes. The fourth is heat transfer due to radiation, and the fifth is

the energy produced from the chemical reactions of all species i. In the simplified 1-D form used here, the derivatives are taken with respect to the z flow axis with the units of W/m^3.

Energy equation:

$$-\rho u c_p \frac{\partial T}{\partial z} + \frac{\partial}{\partial z}(\lambda \frac{\partial T}{\partial z} - \frac{\partial q_r}{\partial z}) - \sum_{i=1}^{N} h_i^o \dot{w}_i = 0 \tag{3.18}$$

Chemistry source term

The complexity of the calculations comes from the source term. To understand the formulation of this highly non-linear term a derivation is presented here. Starting from the Arrhenius formulation of the reaction rate (forward):

$$k_f = A_{k,f} T^n e^{-\frac{E_a}{RT}}$$

where k = 1,2,3...M number of elementary reactions, $A_{k,f}$ is the pre-exponential factor, n the temperature exponent, E_a the activation energy, R the universal gas constant and T the gas temperature. For multiple reversible reactions with M_i molecules:

$$\sum_{i=1}^{N} \nu_{i,k}^{'} M_i \leftrightharpoons \sum_{i=1}^{N} \nu_{i,k}^{"} M_i$$

The progress of reaction variable, in kmol/m^{3}s, is calculated:

$$w_k^{'} = w_{k,f} - w_{k,b} = [k_{k,f} \prod_{j=i}^{N} C_j^{\nu_j^{'}} - k_{k,b} \prod_{j=i}^{N} C_j^{\nu_j^{"}}]$$

where i = j = 1,2,3...N species, C_j the concentration of the j^{th} species, $\nu_j^{'}$ the stoichiometric coefficient of the j^{th} reactant species, $\nu_j^{''}$ the stoichiometric coefficient of the j^{th} product species. It is multiplied by the product of the stoichiometric coefficients

to give the molar reaction rate of species i for reaction k:

$$\widehat{w}_{i,k} = (\nu_i^{"} - \nu_i^{'})[k_{k,f} \prod_{j=i}^{N} C_j^{\nu_j^{'}} - k_{k,b} \prod_{j=i}^{N} C_j^{\nu_j^{"}}]$$

The result is summed up for each reaction giving the molar production/destruction rate of species i in kmol/m^{3}s:

$$\widehat{w}_i = \sum_{k=1}^{M} (\nu_i^{"} - \nu_i^{'})[k_{k,f} \prod_{j=i}^{N} C_j^{\nu_j^{'}} - k_{k,b} \prod_{j=i}^{N} C_j^{\nu_j^{"}}]$$

The equation is multiplied by the molecular weight. The final equation for net mass production/destruction rate of species i, $\dot{w}_i$ in kg/m^{3}s, is:

$$\dot{w}_i = MW_i \sum_{k=1}^{M} (\nu_i^{"} - \nu_i^{'})[k_{k,f} \prod_{j=i}^{N} C_j^{\nu_j^{'}} - k_{k,b} \prod_{j=i}^{N} C_j^{\nu_j^{"}}]$$

The final term is evaluated for each species. Its non-linearity is source of complexity in reacting flow problems.

Boundary conditions

The flanges, where the fuel and oxidizer are issued from, are separated by a distance *d*. The origin of the physical axis is z, at the fuel side. The following boundary conditions apply:

$$z = 0, \quad u = u_{fuel}, \qquad V = 0, \quad T = T_{fuel}$$
$$z = d, \quad u = u_{oxidizer}, \quad V = 0, \quad T = T_{oxidizer}$$

In addition, gradient of velocity, mass flux, and temperature are all forced to zero at the boundaries.

Numerical code

The reacting flow problem is solved using Cantera, an open-source software package developed by David Goodwin at California Institute of Technology (Goodwin, 2003).

The equations, seen above, are discretized and derivatives are calculated with finite differences. The solution propagates forward from j to j+1 in the domain (j = 0, 1, 2....n), i.e. from the left boundary to the right. Only the continuity equation is solved using backward differences and the derivatives of the momentum equation are calculated using central differences. When the gradient and curvature of the dependent variables exceeds certain refinement criteria, an adaptive grid algorithm is used to refine the solution and to increase the number of grid points. A damped Newton method is used to solve the steady-state boundary value problem. If no steady solution can be found, a time marching scheme is used to achieve a solution. Both steady state and time step tolerances can be controlled by the user (see table page 44).

Thermodynamics properties such as temperature, pressure, and chemical potentials are calculated by the appropriate equations of state. The mixture gas properties are computed constantly throughout the iterations and the final solution gives the properties at each grid point.

The transport manager evaluates viscosity, thermal conductivity, diffusion coefficients, etc. The user has the choice between a mixture average or a multi-component transport manager. Using the former give a draft solution. Using the later subsequently, gives a refined solution.

The kinetics are also calculated simultaneously for each iteration and each grid point. Kinetics properties such as reaction rates of progress (ω_k) and equilibrium constants are calculated for each reactions. Here the GRI 3.0 (Smith et al., Accessed

July 2008) chemical mechanism[2] is used for methane oxidation which includes kinetics for 325 reactions and 53 species.

Past research has showcased the capability of the softare package to simulate impinging flows and stagnation flames in a premixed configuration (Bergthorson, 2005; Bergthorson et al., 2005a,b; Benezech, 2006). To my knowledge, this study marks the first time that the modified code has been used for the calculation of non-premixed flames using radiation and cross-transport effects.

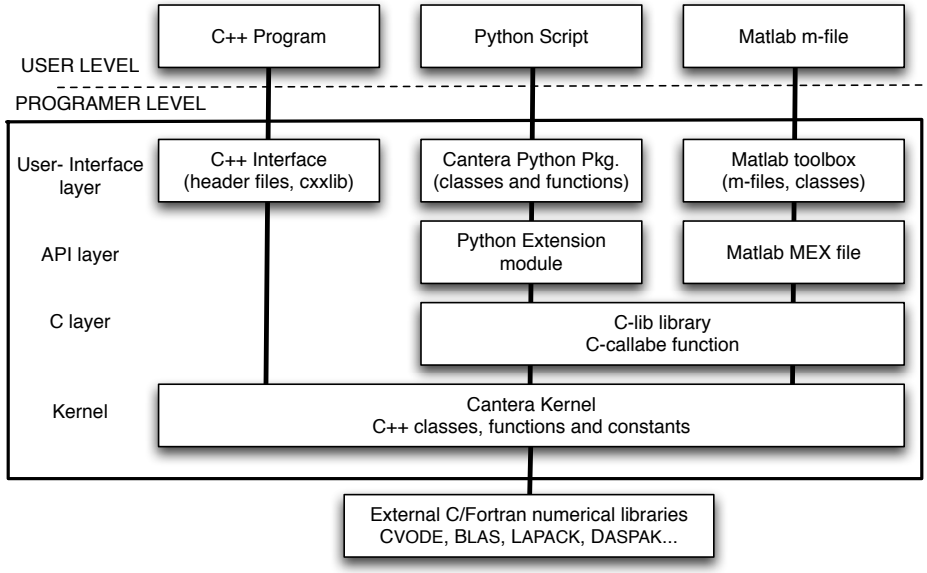

Figure 7. Cantera program layering (Goodwin, 2003).

The kernel of the program was written in C++. The user has a choice of interface: Python, Matlab or Fortran. Figure 7 illustrates the different layers of the program. During the present work, the original kernel was modified to include radiation in the energy equation. Additionally cross-transport terms were included in the transport

[2]Chemical mechanisms can be interchanged easily in the user code, allowing for different fuel or reduced mechanism to be used.

manager. The code was compiled using the Mac OS X Leopard, version 10.5, on a personal computer. In the following sections the different inclusions and modifications to the original source code will be explained.

Inclusion of radiation model

For different reacting flow problems, the code solves a set of PDEs equations 3.8, 3.10, 3.11 and 3.18. A precise solution to the opposed-jet reacting flow is progressively found using transport models of varying complexity: a mixture averaged diffusion followed by a multi-component diffusion model. In the same way the solution is first found without calculating the energy equation followed by a full calculation. The energy equation is discretized in the exact same terms as equation 3.18 but for the divergence of the radiation heat transfer term. As of the latest code compilation (version 1.7, 2007), radiative heat flux was not included.

As shown in past studies, radiation, i.e. absorption and/or emission through the flame has a strong effect on flame temperature (Grosshandler, 1990), as well as certain species concentrations and overall flame structure (Daguse et al., 1996; Barlow et al., 2001; Zhu et al., 2002; Kim et al., 2003; Sutton and Fleming, 2008). The study of Zhu et al. (2002), concluded that a simulation including radiative heat transfer provided a better match to experimental data than the adiabatic calculations. The study examined flames with an equivalence ratio of $\phi = 1.8$. Three different models were compared: adiabatic, optically thin and optically thick. A noticeable radiation effect was observed in the flame spatial structure. When examining species concentrations such as NO and CO, these models provided an over-prediction, under-prediction and good prediction of thermochemistry respectively. While analyzing scalar profiles of NO formation in partially premixed methane/air flame Barlow et al. (2001) also

stressed the significance of including radiation effect in order to capture the partially premixed flame structure. It should be noted that these previous studies compared experimental data set from Sandia laminar flames to numerical simulations using Chemkin with the GRI 2.11 detailed-chemistry mechanism. The present study was motivated by the need of an open-source software to substitute Chemkin in similar detailed-chemistry/multiscalar measurements comparisons.

In order to provide a more accurate simulation that better matches the experimental data, I include in the code the calculation of radiative heat transfer, i.e. the third term in the energy equation 3.18. Two models were implemented, one that treated the radiative heat flux as a function of temperature only, while the other included species dependency. Both models calculated radiative heat loss using an optically-thin aproximation for the flame.

Temperature-dependent radiation model

The first model uses the simple radiation law, radiative heat loss from every grid cell to the environment is accounted for the mixture in general without any consideration of the particular chemical composition. The Stefan-Boltzmann law describes the divergence of heat transfer as:

$$\nabla \cdot \bar{q_r} = \varepsilon\sigma(T^4 - T_b^4) \tag{3.19}$$

where σ is Stefan Boltzmann constant ($\sigma = 5.6704 \times 10^{-8} W m^{-2} K^{-4}$). Background temperature ($T_b = 300K$) is included in order to avoid the unrealistic effect of temperature dropping below its boundary value. The mixture is treated as a grey body, i.e. $0 \leq \varepsilon < 1$. The emissivity (ε) of the mixture signifies the portion of radiation emitted when compared to the equivalent black-body emission. An ethane flame, for example, will have a value of ε varying from 0.4 to 0.7, based on the CO_2 absorption

band at 4.3 μm for the following range of temperature: 800 to 1100 K. This was found by Brahmi et al. (1999) while performing experiments in microgravity to determine global emissivity for thin laminar diffusion flame and validate IR images against thermocouple readings. As a first approximation and to induce a small effect, a small constant value of $\varepsilon = 0.2$ was chosen. Results of this radiation model are detailed in Chapter V.

RADCAL-based model

Guided by the proceeding of the Turbulent Non-premixed Flames workshop (Smith et al., Accessed November 2008), model 2 is formed based on radiation loss due to specific species i. Emission from the following main species is considered: H_2O, CO_2, CO, CH_4. The model for this approach is based on the narrow band model RADCAL (Grosshandler, 1993) with the assumption that self-absorption is negligible in the flame. Past studies (Zhu et al., 2002) have shown that this assumption produces an adequate description of the flame. Also the results of this model produce a somewhat lower temperature than the physical reality.

The RADCAL model was originally developed by W.L. Grosshandler (1993). The original code calculates spectral intensity from four select species, includes soot, and calculates emission and absorption in a finite element volume. Instead of using the original RADCAL Fortran code, it is easier here to integrate the divergence of heat flux in the energy equation as described below, where the coefficients a_i are curve fits of the original RADCAL routine:

$$\nabla \cdot \bar{q_r} = 4\sigma \sum a_{p,i} p_i (T^4 - T_b^4) \tag{3.20}$$

where $a_{p,i}$ is the Planck mean absorption coefficient of species i, which is in general

dependent on temperature and wavelength[3]. The curve fits of the coefficients $a_{p,i}$ have been published for the main emitters in the flame, i.e. methane, water, carbon monoxide and carbon dioxide, on the Turbulent Non-premixed Flames (TNF) workshop web-site (Smith et al., Accessed November 2008). They are reproduced here (Table II) and can be seen as a function of temperature in figure 8. The curve fit are valid from 300 K to 2500 K below a pressure of 1 MPa (9.8 atm). Partial pressure of species, p_i, can be replaced by the local pressure times the mole fraction of the species, $X_i P$. Since the problem is isobaric, the pressure P is one atmosphere.

Table II. Temperature polynomials and coefficients from Turbulent Non-premixed Flames (Smith et al., Accessed November 2008)

CH_4			
$a_{p,CH_4} = 6.6334 - 0.0035686T + 1.6682E^{-8}T^2 + 2.5611E^{-10}T^3 - 2.6558E^{-14}T^4$			
H_2O and CO_2			
$a_{p,CO_2} = a_{p,H_2O} = c_o + c_1(1000/T) + c_2(1000/T)^2 +$			
$+c_3(1000/T)^3 + c_4(1000/T)^4 + c_5(1000/T)^5$			
Coefficients:		H_2O	CO_2
	c_o	-0.23093	18.741
	c_1	1.12390	-121.310
	c_2	9.4153	273.500
	c_3	-2.998800	-194.050
	c_4	0.51382	56.310
	c_5	$-1.86840e^{-5}$	-5.8169
CO			
$a_{p,CO} = c_o + c_1T + c_2T^2 + c_3T^3 + c_4T^4$			
		$300 \leq T \leq 750K$	$750 < T \leq 2500K$
Coefficients:	c_o	4.7869	10.09
	c_1	-0.06953	-0.01183
	c_2	$2.95775E^{-4}$	$4.7554E^{-6}$
	c_3	$-4.25732E^{-7}$	$-5.87209E^{-10}$
	c_4	$2.02894E^{-10}$	$-2.5334E^{-14}$

[3]The Planck coefficients have been determined for a temperature range and integrated over the broad-band of wavelengths leading to $a_i = f(T)$.

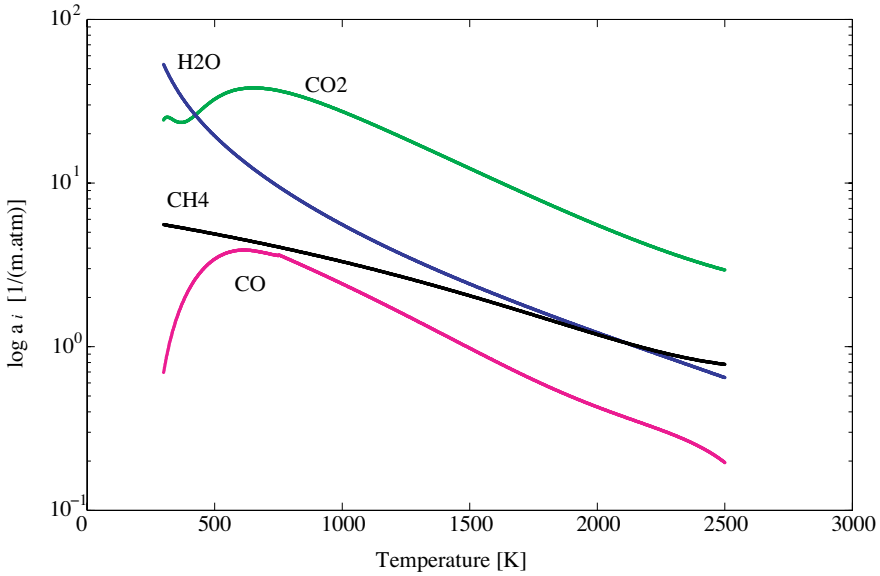

Figure 8. Planck mean absorption coefficients dependency on Temperature, curve fits based on RADCAL (Smith et al., Accessed November 2008).

The numerical solution of the energy equation includes the extra term for radiative heat flux[4]. As will be shown in Chapter V, the radiation effects are important for the calculation of flame thermochemistry.

Higher order cross-transport terms

Another area where previous research has indicated that numerical simulations should be expended is the physics of cross-transport phenomena. These higher-order terms are sometimes neglected in reacting-flow computations, even though they may affect heat and mass transport in certain flame types (Giovangigli, 1999), such as premixed and non-premixed flames with hydrogen fuel (Ern and Giovangigli, 1998; De Charentenay and Ern, 2002; Arias-Zugasti and Rosner, 2008; Grçar et al., 2008). This study

[4]A copy of the implementation of this model in the source code is available upon request to the author.

will demonstrate their effects on laminar partially premixed methane-air flames.

The different processes that take place in flames are accumulation, convection, diffusion and reaction. For high speed flow, in the main reaction zone convection balances reaction. For low speed laminar flames diffusion is essential. Indeed in subsonic processes, in the main reaction zone convection balances reaction. This is apparent in the species conservation equation 3.2:

$$\begin{aligned} \rho\frac{\partial Y_i}{\partial t} + \nabla\cdot(\rho\bar{u}Y_i - \rho D\nabla Y_i) \qquad &= \dot{w}_i \\ \text{accumulation} + \text{convection} + \text{diffusion} \quad &= \text{reaction} \end{aligned}$$

Siimilarly, the conservation energy equation 3.17 shows similar balancing terms:

$$\begin{aligned} -\rho\bar{u}c_p\nabla T + \nabla\cdot(\lambda\bar{\nabla}T) - \nabla\cdot\rho\sum_{i=1}^{N}h^s Y_i\bar{V}_i - \nabla\cdot\bar{q_r} - \sum_{i=1}^{N}h_i^o\dot{w}_i = 0 \\ \text{convection} + \qquad\qquad \text{diffusion} \qquad + \text{reaction} = 0 \end{aligned}$$

Kinetic theory of gases (Hirschfelder et al., 1954; Vincenti and Kruger, 1965; Chapman and Cowling, 1970; Williams, 1985) defines energy transfer to be dependent on molecules collision processes. A summary of the major and minor gradients, mass, momentum and energy transfer equations is given in Table III.

The thermal diffusion coefficient, $D_{T,i}$, the binary $\mathcal{D}_{i,j}$, and the multi-component diffusion coefficient, $D_{i,j}$ of species i into j, units are m^2/s. Dynamic viscosity ($\mu_{i,j}$) units are $\mathrm{kg.m^{-1}s^{-1}}$, and thermal conductivity (λ) units are $\mathrm{Jm^{-1}K^{-1}s^{-1}}$. The term $\bar{V}_i$ denotes the molecular velocity of species i. The numerical simulations models the multi-component diffusion coefficient $D_{i,j}$ after the binary diffusion coefficient $\mathcal{D}_{i,j}$ which itself is based on the kinetic theory of gases. Multi-component diffusion coefficients are difficult to observe and/or measure, even for the simplest multi-component system, the ternary system. Thus approximations are made from the well-known

Table III. Molecular transport phenomena

Diffusion	*Gradients*	*Fluxes*	*Equation*
Mass	Concentration	Fick's law	$\bar{\Gamma}_i = -D_{i,j}\frac{dN_i}{dx}$
	Temperature	Soret effect	$\bar{\Gamma}_S = \sum_{j=1}^{N} \frac{X_i X_j}{\mathcal{D}_{i,j}} \frac{1}{\rho}(\frac{D_{T,j}}{Y_j} - \frac{D_{T,i}}{Y_i})\frac{\nabla T}{T}$
Momentum	Velocity	Newton's law	$\tau = -\mu_{i,j}\frac{dv}{dx}$
Energy	Temperature	Fourier's law	$\dot{q}_F = -\lambda\frac{dT}{dx}$
	Concentration	Dufour effect	$\bar{q}_D = R^o T \sum_{i=1}^{N}\sum_{j=1}^{N}(\frac{X_j D_{T,i}}{MW_i D_{i,j}})(\bar{V}_i - \bar{V}_j)$

binary diffusion coefficients. Another diffusion coefficient available through the simulations, is the mixture average coefficient $D_{i,mix}$ calculated for diffusion of a species i into the mixture.

Dufour term

Usually a temperature gradient gives rise to energy transfer from hot to cold region. The heat flux, or conduction, is usually described by Fourier's constitutive law. This is considered the main energy transfer in the flame, yet in certain cases when heat transfer driven by concentration gradient or mass flux is possible (hence the term cross-tranpsort). This physical effect is called the Dufour effect. The term may work with or against the Fourier term. The equation used for the Dufour effect, $\bar{q}_D$ (see Table III) appears in the total heat flux vector (section , equation 3.14):

$$\bar{q} = -\lambda.\bar{\nabla}T + \rho\sum_{i=1}^{N} h_i^s Y_i \bar{V}_i + R^o T \sum_{i=1}^{N}\sum_{j=1}^{N}(\frac{X_j D_{T,i}}{MW_i D_{i,j}})(\bar{V}_i - \bar{V}_j) + \bar{q}_r$$

The Dufour effect arises when there is difference in molecular velocity between species. Molecules with a higher molecular velocity, or kinetic energy, will tend to move towards a region where the kinetic energy is low. Thus molecules in high-concentration cold region could rise to low concentration warm regions, a process which opposes the Fourier heat flux from hot to cold. The following schematic (figure 9) shows the gradient of temperature ∇T and the Dufour counter-gradient.

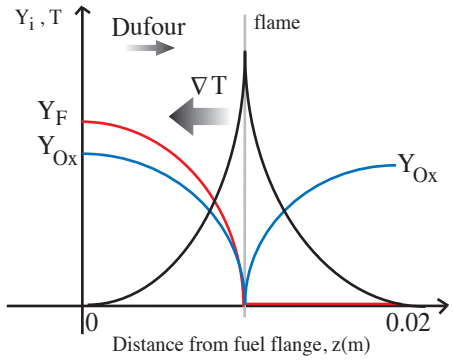

Figure 9. A schematic of Dufour effect in 1-D flame geometry. The spatial structure shows simplified temperature, fuel and oxidizer profiles. The gradient of temperature is counter to the "Dufour" heat transfer.

The term is usually assumed to be negligible in the flame compared to the Fourier diffusion term. I implemented the Dufour term into the energy transport equation of the code for completeness. It is necessary to solve the energy equation with multi-component transport in order for the routine to go through the calculation of the Dufour term. The results will be presented in Chapter V.

Soret term

The major mass diffusion process is due to concentration gradients, and results in species moving from region of high to low concentration. This is Fick's law as described in Table III. In the case where the temperature gradient gives rise to mass

flux, a cross-transport effect arises. This is also a higher order term called Soret effect (Rosner, 1986) or thermophoretic force[5]. Depending on the flame configuration, the Soret flux term can be parallel or opposite to the Fick diffusion flux. As stated before, this is a higher order term because in proportion to the main flux, it is of a smaller order of magnitude.

The temperature difference drives light molecules (such as hydrogen) to hot region and heavy molecules to cold regions, i.e. temperature gradients induce molecular transport. The effect is dependent on species molecular weight. As shown in figure 10 high hydrogen concentration is present in the fuel side just before the temperature peak. The concentration gradient will tend to drive molecules towards the lowest concentration, while the Soret effect will drive the light hydrogen molecules towards the hottest region of the flame peak. The Soret effect will contributes or counteract the main Fick diffusion depending on the magnitude of the temperature gradient and the direction of the concentration gradient.

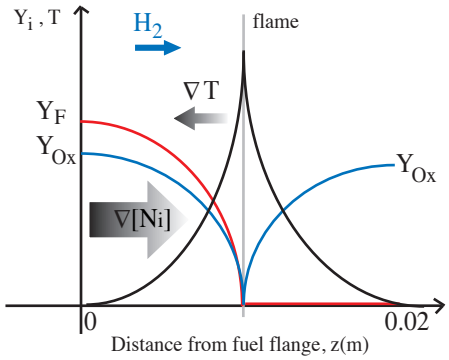

Figure 10. A schematic of Soret effect in a 1-D flame geometry. The simplified flame spatial structure shows temperature, fuel and oxidizer profiles. The gradient of concentration may be countered by the mass transport due to temperature gradient.

[5]Thermal diffusion is a physical process not to be confused with thermal conduction. Thermophoresis is defined as the movement of particles due to temperature gradient.

The thermal diffusion effect is included in the calculation of diffusion mass flux vector for each species ($\bar{\Gamma}_i$) using a multi-component formulation. Neglecting pressure diffusion (Kee et al., 2003; Williams, 1985):

$$\bar{\Gamma}_i = \rho Y_i \bar{V}_i$$

$$\bar{V}_i = \frac{1}{X_i \overline{MW}_i} \sum_{j \neq i}^{N} MW_i D_{i,j} \nabla X_i - \frac{1}{\rho T} \frac{D_{T,i}}{Y_i} \frac{\nabla T}{T} \tag{3.21}$$

where the first term is the multi-component diffusion and the second term represents the Soret effect. The first term gives rise to the classic Fick diffusion in the mixture-average formulation:

$$\bar{V}_i = -D_{i,mix} \nabla X_i / X_i \tag{3.22}$$

As the equation 5.10 shows, the term is important whenever molecular weight disparities - species having disparate molecular weights MW_i- coexist with large temperature gradients. The Soret effect is additionally dependent on the thermal diffusion coefficients of the species i. For most species, thermal diffusion and mixture average coefficient are of a different order of magnitude with the former being subsequentially lower than the latter. This is verified here by extracting both mixture average and thermal diffusion coefficients from one simulation.

Figure 11 shows the results for a test case calculation at an equivalence ratio of 1.8. The variation of diffusion coefficients is shown against the spatial axis. Figure 11a shows the mixture-average diffusion coefficients of species i into the mixture. They are assumed to be equal to the binary diffusion coefficient of species i in Nitrogen, since N_2 is abundant in the flame. Most of the 53 species have similar coefficients with values less than $2 \times 10^{-4} m^2/s$ even at high temperature, hence only the species with large coefficients are plotted. Figure 11b shows that the thermal diffusion coefficient

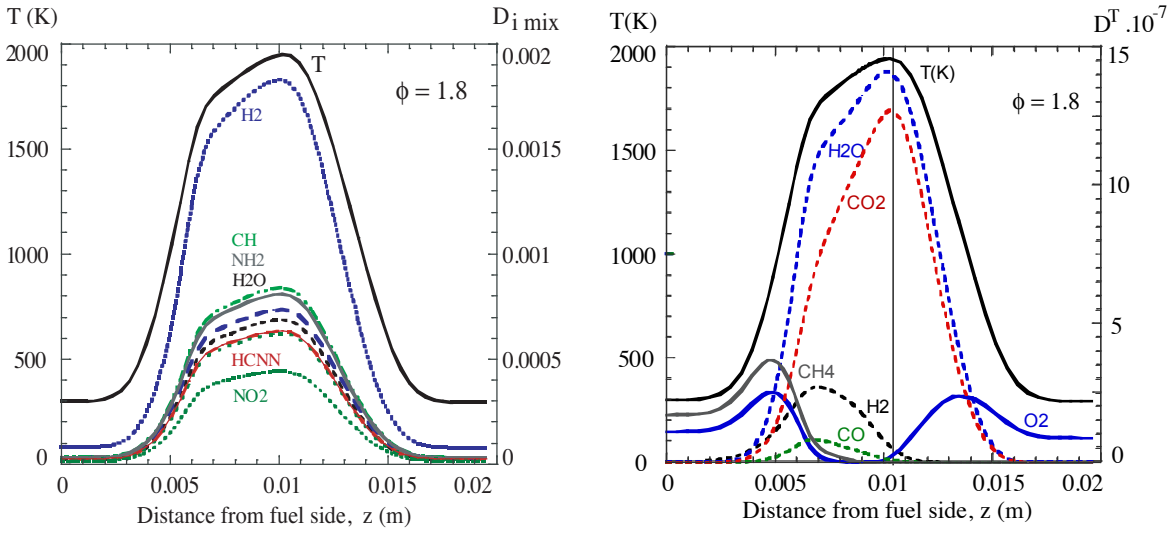

a) $D_{i,j}$ diffusion coefficients b)Thermal diffusion coefficients

Figure 11. Comparison of diffusion coefficients. Case(b), d= 1.95 cm, ϕ=1.8. The absolute values of thermal coefficients are plotted on the right.

for some specific species such as CO_2, H_2O, H_2 are in the order of magnitude 10^{-6} to 10^{-7} m^2/s, most species coefficients are not plotted here (the threshold for the figure is $D_{T,i} \geq 10^{-9}$ m^2/s). The figure shows the magnitude difference between thermal diffusion and Fick diffusion. The magnitude of the thermal coefficients justifies the usual assumption of negligible thermal diffusion in flames employed in computations. Yet some species, such as hydrogen, water, and carbon dioxide, have much higher thermal diffusion coefficients (order of 10^{-6} m^2/s). This implies that the Soret effect is most important when hydrogen is used as fuel, but may also be important in the case of hydrocarbon fuels in regions where hydrogen is generated as the intermediate product of fuel decomposition, as well as in regions where the high-molecular weight fuel experiences high temperature gradients (Rosner et al., 2000). Examining equation 5.10, the Soret effect will be important when $D_{T,i}$ and/or ∇T are large. Furthermore, when hydrogen is taken into consideration, its small molecular weight

leads to a smaller gradient diffusion term (first term in equation 5.10) and to an increased importance of the Soret term (second term in equation 5.10).

As explained by Williams (1985), the higher order terms are very often assumed to be negligible in flame calculations reported in the literature. This assumption has facilitated the development of the simulations until recent times. Analytically and computationally it is easier to neglect these terms and the solutions found for free propagating flames, jet and counterflow flames showed good agreement with experiments. Since the computational cost has decreased for systems involving multi-component transport schemes, Ern and Giovangigli (1998) have studied the effect of the both Soret and Dufour effect in hydrogen-air and methane-air laminar flames with a simplified mechanism. The inclusion of cross-transport had a higher effect on the hygrogen-air and in the methane-air rich burner stabilized flame than on the jet flame configuration, or a counterflow stoichiometric methane-air flame under high stretch: $a \simeq 500 s^{-1}$. Later, De Charentenay and Ern (2002) studied the effect of multi-component transport schemes on 2-D turbulent flames. The dimensionality led to an expected increased in computational time, affected the turbulent flame properties such as laminar flame speed by 50 %, but when considering mean quantities, the effects were lower (7 % increase only)[6]. Palle, Nolan and Miller (2005) examined the effect of cross-transport on laminar flames at high pressures (between 10 to 100 atmospheres) using a single-step reaction. The study concluded on the importance of including both cross-transport terms when the molecular weights of species in the flame were disparate. Arias-Zugasti and Rosner (2008) have studied the Soret effect on laminar flames for non-unity Lewis number cases. One interesting finding was that the flame temperature structure, both the maximum as well as the whole profile, was

[6]The origin of this work is due to the theoretical study of the cross-transport phenomena by Rosner and Gomez (1993).

affected by the molecular weight of the fuel investigated. For light fuel when mass diffusion coefficient $D_{i,j}$ is larger than the thermal diffusion coefficient, the structure was shift towards the oxidizer side, which reinforced the effect of nonunity Lewis number fuel.

More recently, Grçar, Bell and Day (2008) investigated the effect of full multi-component transport (including multi-component diffusion coefficients and higher order diffusion terms) on free propagating hydrogen-air flame. The study implication was the cross-transport processes, involving hydrogen, greatly enrich the fuel zone, affect extinction and division of flame structure, and provide better estimate of flame speed. The effect of the new computations seems greater on propagating flames than planar or conical flames. The latest work on the subject was demonstrated by Dworkin, Smooke and Giovangigli (2009) on ethylene/air flames. While most of the previous examples concerned premixed flames, the present study contributes to the understanding of cross-transport effect on partially premixed methane-air flame. Results of the augmented simulations for the opposed jet flow configuration, are described in the following chapter. It will be shown how the Soret effect had a significant impact on certain mass fraction profiles through the flame, and a lesser but substantial effect on the conserved scalar (Z_H) profile.

Convergence study

A convergence study was performed to examine the solution dependency on grid refinement. The software package uses a grid refinement that is controlled by three criteria: the ratio, slope, curve and prune. The ratio controls the maximum cell-length ratio between adjacent cells. When the ratio is decreased, the number of grid points increases. The slope and curve criteria add grid points when the difference in

slope and curve between two adjacent cells exceed the value selected by the user. The prune criterion removes points when slope and curve arguments are satisfied. The last criterion is not used in the present simulations.

Several test cases are computed with different grid refinement criteria for a partially premixed methane air flames at equivalence ratio of 2.2, and fuel/oxidizer inlet distance of 1.95 cm. Simulation output parameters such as maximum flame temperature, maximum mass fraction were compared to the final temperature and mass fraction of best resolved calculation with 186 grid points. The temperature as well as the mass fraction errors of methyl radical (%error of Y_{CH}), and formyl radical (%error of Y_{HCO}) are calculated. Their values are 1.3×10^{-7} and 5.7×10^{-7} respectively. These species were chosen for comparison to evaluate the effect of grid refinement on minor species concentrations. In addition, the formyl radical was chosen because its profile shows two peaks: one in the rich premixed zone, and one before the main reaction zone. The distance between the two zone is only slightly affected by the grid refinement process.

In figure 12, some error metrics are plotted as functions of the number of grid points. The solution for temperature is always constrained within 1 %, regardless of grid choice and the final calculated maximum flame temperature is within 1.7 % of the experimental determine values. The minor species CH and HCO fall in the 2 % error band if grids with more than 100 points are used. The simulation resulting in a 100-point grid had the following criteria: ratio of 3, slope of 0.2, and curve of 0.8, while the solution was obtained in 14 minutes. The final calculations were achieved with a grid of less than 100 points (80-90 points in general) due to the overhead computational time necessary for the Soret and radiation routines at lower equivalence ratios, especially ϕ of 1.8. Keeping a short run time allows the computations to be used for industrial applications where hundreds of iterations are

necessary to cover different combustion regimes.

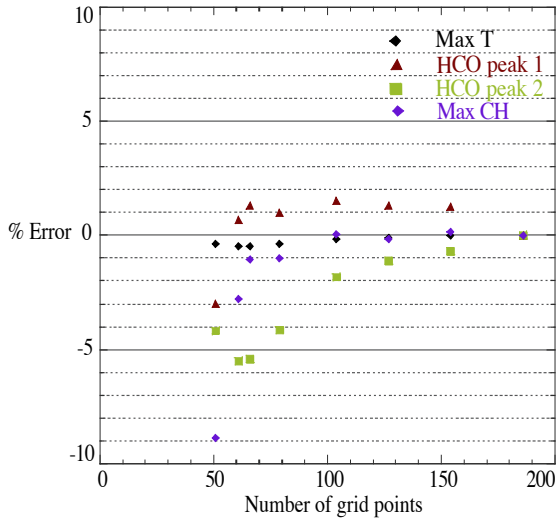

Figure 12. Computational convergence study. Case (b), d= 1.95cm, $\phi = 2.2$.

Finer grid resolution were not selected because of the cost on computational time. Although a solution falling within the one percent error band would have been more precise, the run time reaches 40 minutes for a 150-point grid and up to 60 minutes for a 200-point grid. Besides run time, convergence failure also increases as the complexity of the physical flame problem increases. The simulations tends to be longer and less likely to converge as the fuel amount in the air decreases (low ϕ) and the flame becomes closer to being premixed. The solution convergence is also dependent on the time steps for the time integration method. As the number of grid point increased, it was necessary to lower the time-step size or the simulation would fail to converge. Grid refinement problems and computational expense for each code modification that included Radiation, Soret and Dufour terms will be examined in detail in the following chapters.

CHAPTER IV

FLAME SPATIAL STRUCTURE

The inclusion of an optically-thin radiation model and the cross-transport effects calculations allow for detailed-chemistry computations that can be compared favorably to experimental data. The structure of partially premixed methane-air flames can be studied by presenting results in physical space. The goal of the present study is to analyze the structure of the flames at different equivalence ratios and explore their similarities. In this section, numerical results are validated with the experimental data presented in Chapter III. The comparison between the two is based on the assumption that an opposed jet flow (1-D) can reproduce the results obtained with single-point measurements in an axisymmetric laminar flame, as described in Chapter II. A discussion of the limitations of the 1-D numerical scheme when used to simulate a 2-D axisymmetric flame follows.

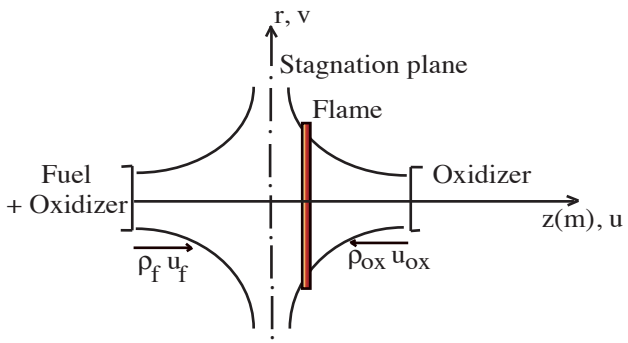

Figure 13. Opposed jet flow configuration.

Table IV. Cantera simulations parameters. Flange distance is specified for each case

Parameters	Case a *2 [cm]*	Case b *1.95 [cm]*	Case c *8 [cm]*
Premixture (methane and air)			
Mass flow rate [kg/m^{2}s]	0.084	0.084	0.18
Jet initial temperature[K]	294	294	294
Oxidizer			
Mass flow rate [kg/m^{2}s]	0.084	0.084	1.02
Jet initial temperature [K]	300	300	300
Cold strain rate [1/s][ϕ=1.8, 2.2, 3.17]			
α_o	[7.54, 7.42, 7.56]	[7.73, 7.61, 7.37]	[14.11, 13.75, 13.58]
a_{ox}	[7.2, 7.25, 7.27]	[7.37, 7.4, 7.46]	[13.05, 13.12, 13.3]
V	[27.6, 24, 22]	[23.7, 21.8, 20.8]	[28.1, 28.4, 30.6]
GRID			
Initial grid	10 points	10 points	40 points
Final grid	86 points	84 points	88 points
Tolerance			
Steady state problem	$[10^{-5}; 10^{-6}]$	$[10^{-5}; 10^{-6}]$	$[10^{-5}; 10^{-6}]$
Time stepping	$[10^{-5}; 10^{-2}]$	$[10^{-5}; 10^{-9}]$	$[10^{-4}; 10^{-9}]$
Grid refinement criteria, [ratio, curve, slope]			
Without the energy equation selected	[3, 1, 1]	[50, 0.4, 0.8]	[10, 0.3, 0.6]
With the energy equation	[3, 0.1, 0.1]	[10, 0.1, 0.2]	[20, 0.4, 0.8]
With Soret option	none	none	none

In the opposed jet flow configuration (figure 13) methane and air at an equivalence ratio ϕ are injected in the domain from the left side. It is opposed on the right side by a jet of air. The temperature and the composition at the two inlets are matched to the experimentally determined values. The mass flow rate of each stream as well as the distance between the jets or flange can be varied, and is adjusted to match at best the expected cold strain from the experiments[1]. The baseline

[1]The cold strain in axisymmetric flames is not easily determined from available experimental data

computations in this work are carried out in a spatial domain of 2 cm. The main reaction zone, as indicated by high temperatures, spans only a few millimeters. All the parameters for the calculations are reported in Table IV.

Strain rate parameter

The strain rate is usually the parameter of choice to match the experimental data with the computations. The strain rate tensor has nine components in a cylindrical coordinate system (r, θ, z). Since the flow is one dimensional, the strain rate here is a scalar. It can be defined as the gradient of the velocity in the z direction.

Figure 14 shows the variation of the velocity u and the location of the stagnation line and flame (location of maximum temperature). By definition of the flow axis z, the velocity is positive at the left boundary. In the cold flow case where no ignition is possible, it is easy to see that the velocity profile from one inlet to the other is continuous and monotonic. For the reacting case, the flow field is modified due to the presence of chemical reactions in the flame as displayed in figure 14. The effect of heat release and density variation in the flame creates a displacement (Kim et al., 1992) that affect the velocity and the strain rate. Recalling the mass conservation equation 3.1 in vector form:

$$\nabla \cdot (\rho \bar{u}) = \bar{u} \cdot \nabla \rho + \rho \nabla \cdot \bar{u}$$

where the second term (dilatation) balances the change in density due to the reactions. Figure 14, shows the displacement in the stagnation line or the effect of dilatation from the cold flow case to the reacting flow case.

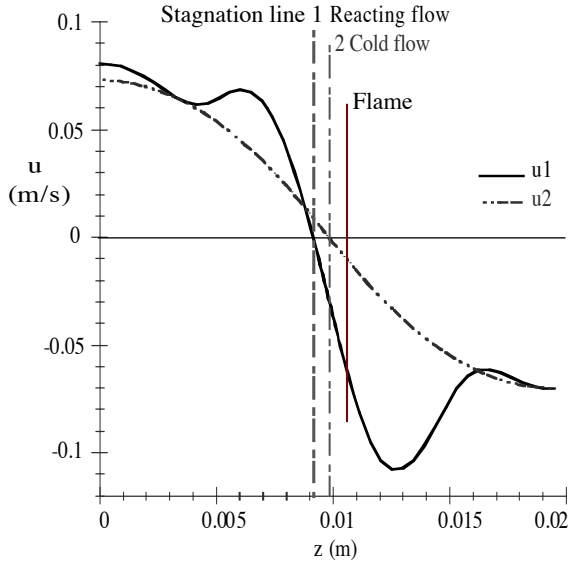

Figure 14. Opposed jet velocity profile. Cold flow velocity profile and stagnation line 1 are depicted in grey. Reacting flow velocity profile and stagnation line are depicted in black. Case (b), d=1.95 cm, ϕ=3.17.

The choice of a strain parameter is not unique as it is hardly possible to define a single strain rate applicable to the whole flame. Kim et al. (1992) proposed a cold-strain value for the counterflow configuration that takes into account the boundary (inlet) densities:

$$a_{ox} = \frac{u_{ox}}{d}(1 + \frac{u_f\sqrt{\rho_f}}{u_{ox}\sqrt{\rho_{ox}}}) \tag{4.1}$$

where d is the distance between the inlets. The value determined from equation 4.1 applies to the oxidizer side of the flame, yet a similar value can be determined for the fuel side. A simpler formula where the strain in dependent on both velocity fuel and oxidizer jets is found by setting ρ_f equal to ρ_{ox}, and used in the present work:

$$\alpha_o \sim \frac{|u_{fuel}| + |u_{ox}|}{d} \tag{4.2}$$

It has been used in previous study to describe laminar flames (Barlow et al., 2001).

I used a parametric variation of the mass flow rate to obtain the closest fit of the

temperature profile to the experimental data for the richest flame at $\phi = 3.17$. The final simulations (Case(c), d=8 cm, $\phi = 3.17$) correspond to a cold strain rate of 14 s^{-1} and a peak value of scaled velocity (V) of 30 s^{-1} at the maximum temperature in the flame.

Flange separation distance

The first cases studies were computed with a distance of 2 cm between the fuel and oxidizer stream (figure 15 case a). Several case studies were performed by varying the distance between the inlets, keeping the calculated cold strain value constant and changing the mass flow rates. In case b, the inlets are separated by 1.95 cm and in case c and d by 8 cm. Increasing the separation between the inlets simulates a potential flow condition near the flame instead of the original plug flow formulation. Moving the stagnation line away from the oxidizer or fuel inlet eliminates possible computations errors (unrealistic concentrations values) at the boundary. Yet the physical manipulations of the inlet distance does not succeed in representing the flame temperature and chemistry profile of the axisymmetric flame. For example, the experiments temperature profile on the rich side exhibits a steeper gradient than the calculations. The best calculation results that matches the experiments on the physical axis are achieved with configuration case (c). The comparison between the experiment data of axisymmetric flames and the simulation of opposed jet flames can be seen in Appendix A where the nine species and temperatures are plotted in physical space. The examination of the physical profiles of temperature and species shows more discrepancy at lower ϕ.

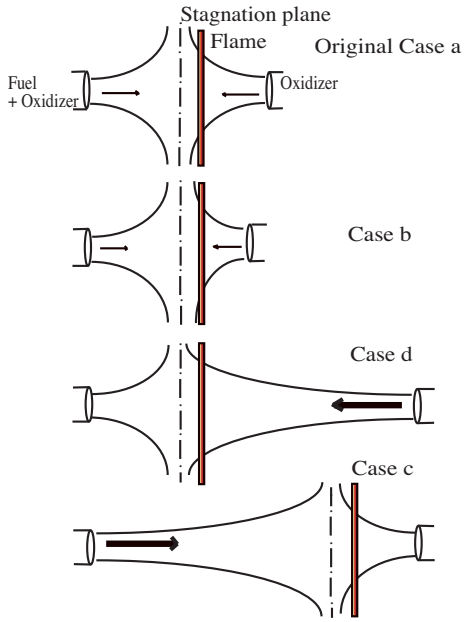

Figure 15. Flange distance variation to change the velocity profile.

The flame structure is affected by both the variation of ϕ and the variation of strain rate. The latter has a direct effect on the flame structure by reducing the distance between the reaction zones (main reaction corresponding to the maximum peak and second reaction zone in the rich premixed zone corresponding to the curvature change in the temperature profile). When the strain is increased, both the temperature profile and the temperature gradients are affected on both side of the flame. The variation of equivalence ratio naturally affects the chemical reactions everywhere thus changing the flame structure when fuel is added to the premixture. This confirms the findings of Xue and Aggarwal (2001).

Experimental results

The experimental data-set is detailed here in order to highlight the salient thermo-chemistry features of the flame. The data points were obtained with high-precision

laser diagnostics. Single-point multiscalar measurements were taken in the three partially premixed laminar jet flames of table I. The experimental apparatus consisted of a Raman/Rayleigh system for the measurement of major species (CH_4, CO_2, H_2, CO, O_2, H_2O, N_2) concentration and temperature. A two-photon Laser-Induced Fluorescence (LIF) system was used for an independent measurement of carbon monoxide concentrations with high accuracy, while additional LIF systems were used for the simultaneous measurement of OH and NO species concentrations. CO measurements were redundant but more accurate with the use of two-photon LIF than with the Raman system. The single-point measurements were taken at three different locations as shown in chapter II figure 3, i.e. at 25, 50 mm, and 100 mm above the nozzle exit. The optical resolution of the multi-scalar measurements was 500 μm. A full description of the system and a discussion of experimental accuracies as determined by calibration against known flames can be found in the references (Barlow et al., 2000, 2001). For complete detail on the measurement techniques and laser set up see Masri, Dibble and Barlow (1996).

In figure 16 through 19, the flames are photographed from the leaner ($\phi = 1.8$) on the left to the richer ($\phi = 3.17$). Only measurements at 50 mm and 100 mm are shown in the figures. Superposed on each image are the experimental measurements of thermochemistry. The first relationship that can be induced from theses figure relates the flame length to the equivalence ratios ϕ. With increasing premixture strength, the amount of air needed to diffuse inward to reach the stoichiometric value increases, the axial distance for the necessary diffusion increases, thus increasing the flame height as found by Bennett et al. (2000). In other words as the fuel axial convective flux increases while the oxygen radial flux remains constant, the axial distance needed to reach a stoichiometric mixture increases. Similar trends have been observed in laminar Gore and Zhan (1996) and turbulent Lyle et al. (1999) partially premixed

flames. In all cases, the flame length increases with ϕ for small values of ϕ. The trend disappears and the flame height remains constant for values of ϕ larger than some value (close to 3.) Such a 'transition' in flame behavior has been found in all aspects of partially premixed flames in the past. It is intuitively expected, since with increasing ϕ the flames should recover all the characteristics of non-premixed flames. The blue flame color seen in each flame is due to chemiluminescence, i.e. emissions from species such as OH, CH, C_2 and CO_2. When examining the reactants methane and oxygen (figure 16) the main reaction zone is marked by the fuel mass fraction going to zero and the oxygen being depleted for the combustion. At the 50 mm location for increasing premixture strength, the fuel mass fraction shows a flatter profile in the middle of the jet of the rich flame compared to the leaner flame. A similar trend can be seen when looking at the temperature profile (figure 17), demonstrating how the flame structure becomes thinner with increasing ϕ. Examining the OH profile (figure 17) the peak in concentration is located just outside the temperature peak of each flames. Hydroxyl radicals (OH) are good markers of heat release, thus indicating the outer region of the flame or primary non-premixed reaction zone. Similarities arise when comparing H_2O mass fractions (figure 18) and temperature profiles. Both profiles are wider at low equivalence ratios and include a change in curvature in the rich premixed zone. This leads to a double flame structure. Equivalently, the peak in CO and H2 concentrations (figure 18 and figure 19) at that same location in the rich premixed zone seems to indicate the presence of another reaction. This second reaction zone is possibly due to the partial oxidation of methane to produce CO and H_2 as previously mentioned in the studies by Bennett et al. (2000) and Barlow et al. (2001). The change in temperature profile between the rich and lean flames demonstrates the change in flame structure. As the premixing strength is increased, the partial oxidation of methane in the rich premixed zone decreases and the two

zones merge. Furthermore, in the non-premixed zone while CO and H_2 are depleted, H_2O and CO_2 concentrations stay high or slightly increase. It is possible that CO and H_2 are converted to H_2O and CO_2 through the equilibrium water-gas shift reaction. The water-gas shift reactions are defined as:

$$\begin{aligned} CO + OH &\leftrightarrow CO_2 + H \\ H + H_2O &\leftrightarrow OH + H_2 \end{aligned}$$

Combined to produce the following reaction:

$$CO + H_2O \leftrightarrow CO_2 + H_2$$

In summary, the analysis of experimental results (figures 16 to 19) enables the visualization of the flame structure and the identification a second reaction zone in leaner flame as well as the species involved.

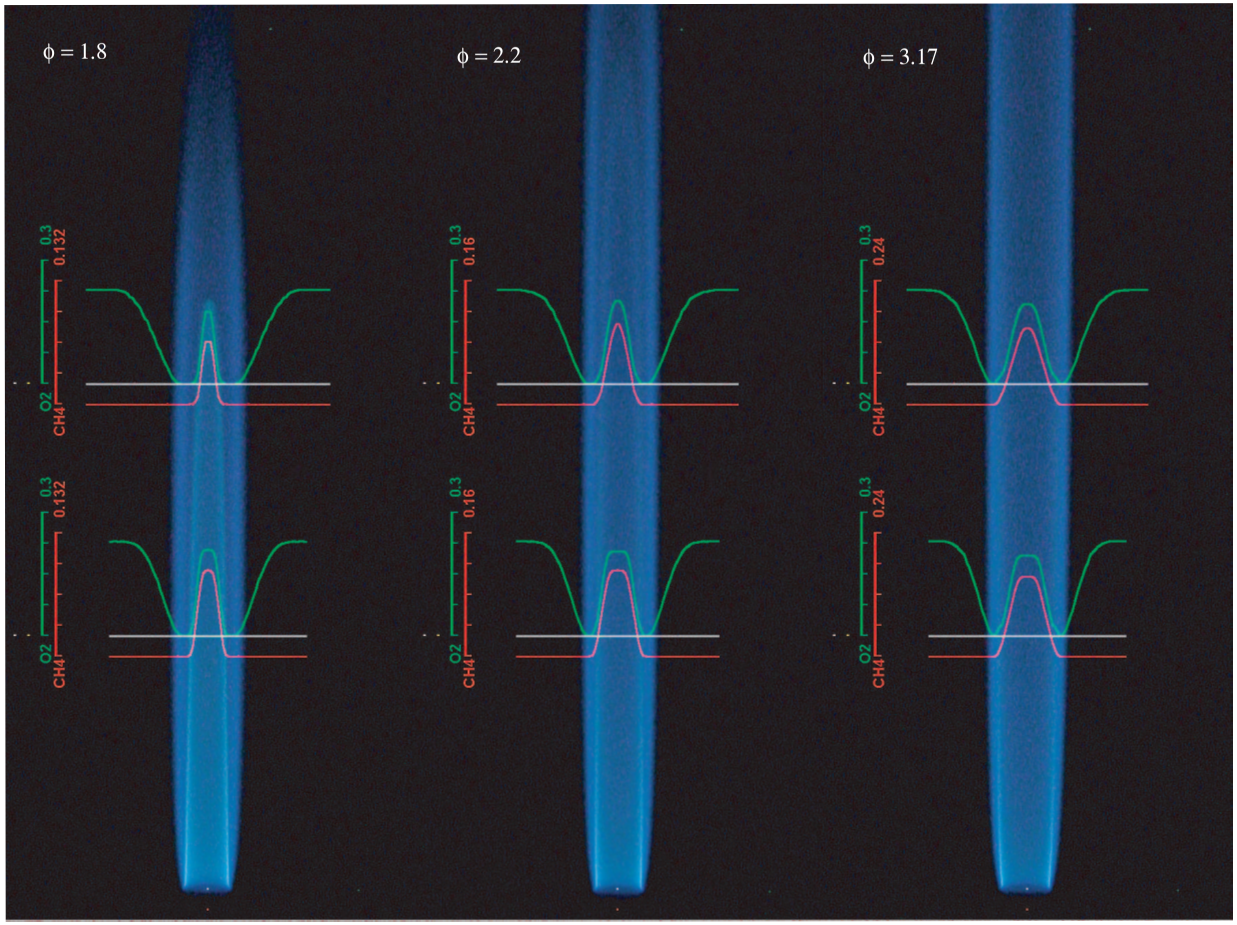

Figure 16. Experimental data product: CH_4 and O_2 mass fraction overlay onto flame photographs. Data from 50mm and 100 mm above the nozzle exit. Partially premixed flame from Combustion Research Facilities, with the permission of Adonios Karpetis.

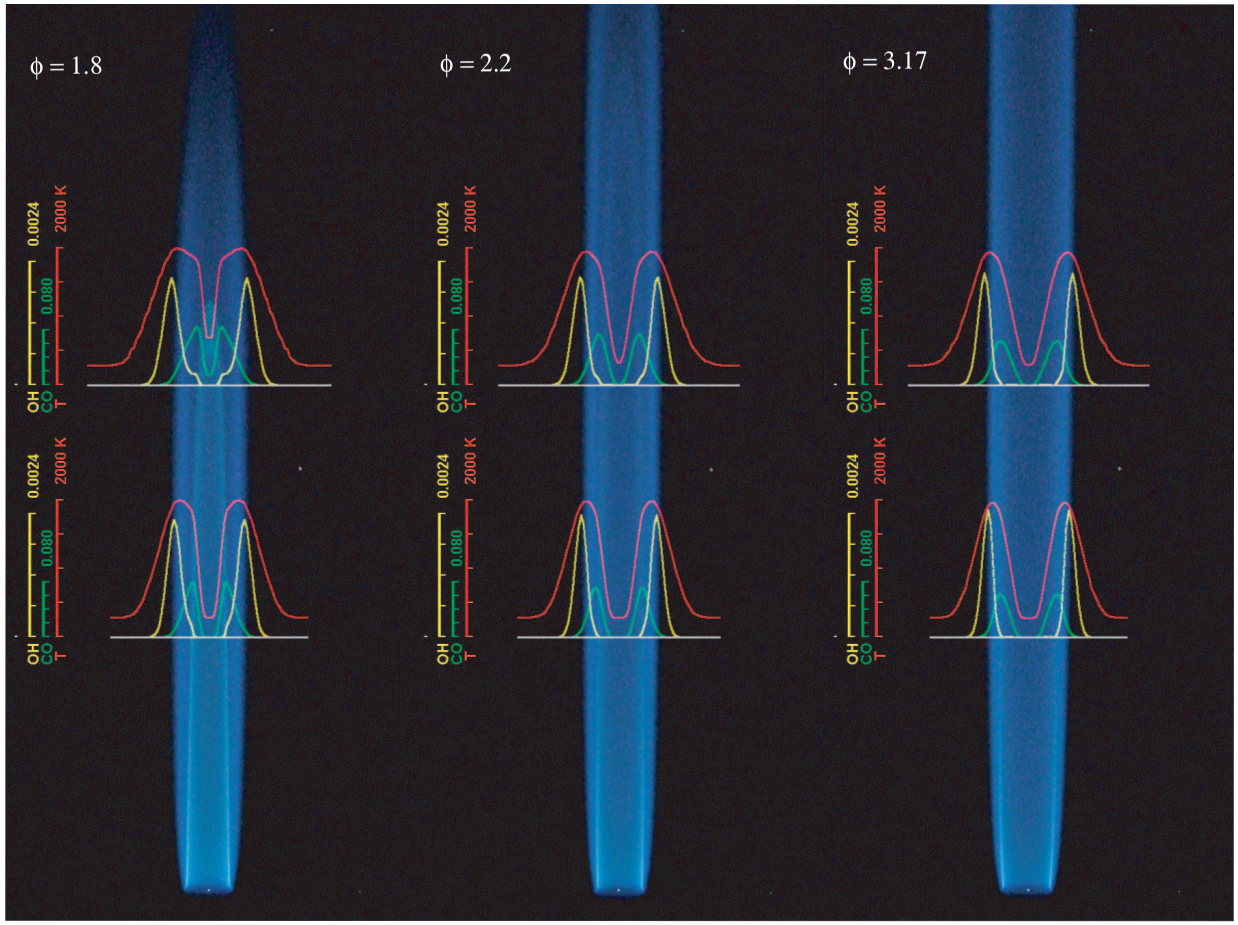

Figure 17. Experimental data product: temperature profile, CO and OH mass fraction overlay onto flame photographs. Data from 50mm and 100mm above the nozzle exit. Partially premixed flame from Combustion Research Facilities, with the permission of Adonios Karpetis.

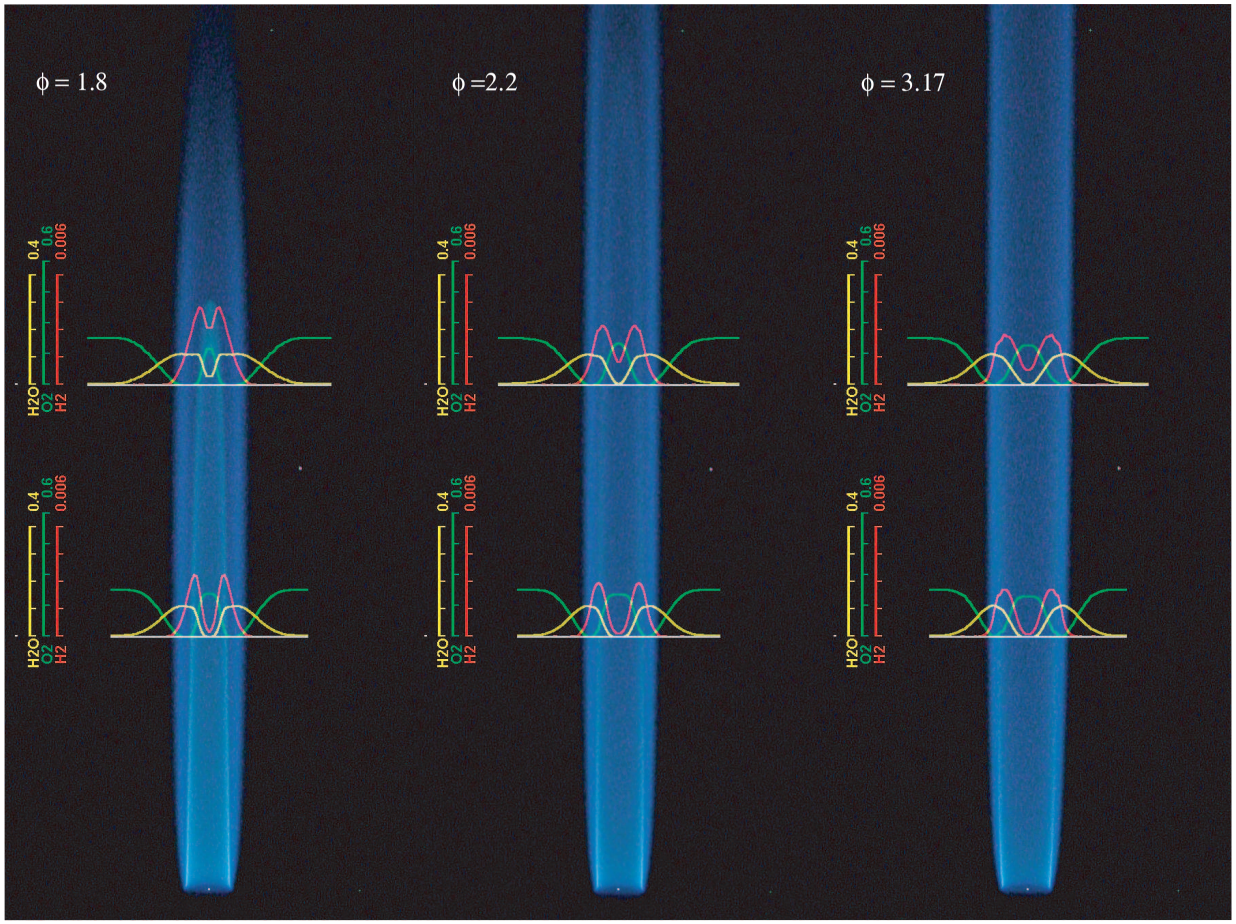

Figure 18. Experimental data product: H_2, O_2, and H_2O mass fraction overlay onto flame photographs. Data from 50 mm and 100 mm above the nozzle exit. Partially premixed flame from Combustion Research Facilities, with the permission of Adonios Karpetis.

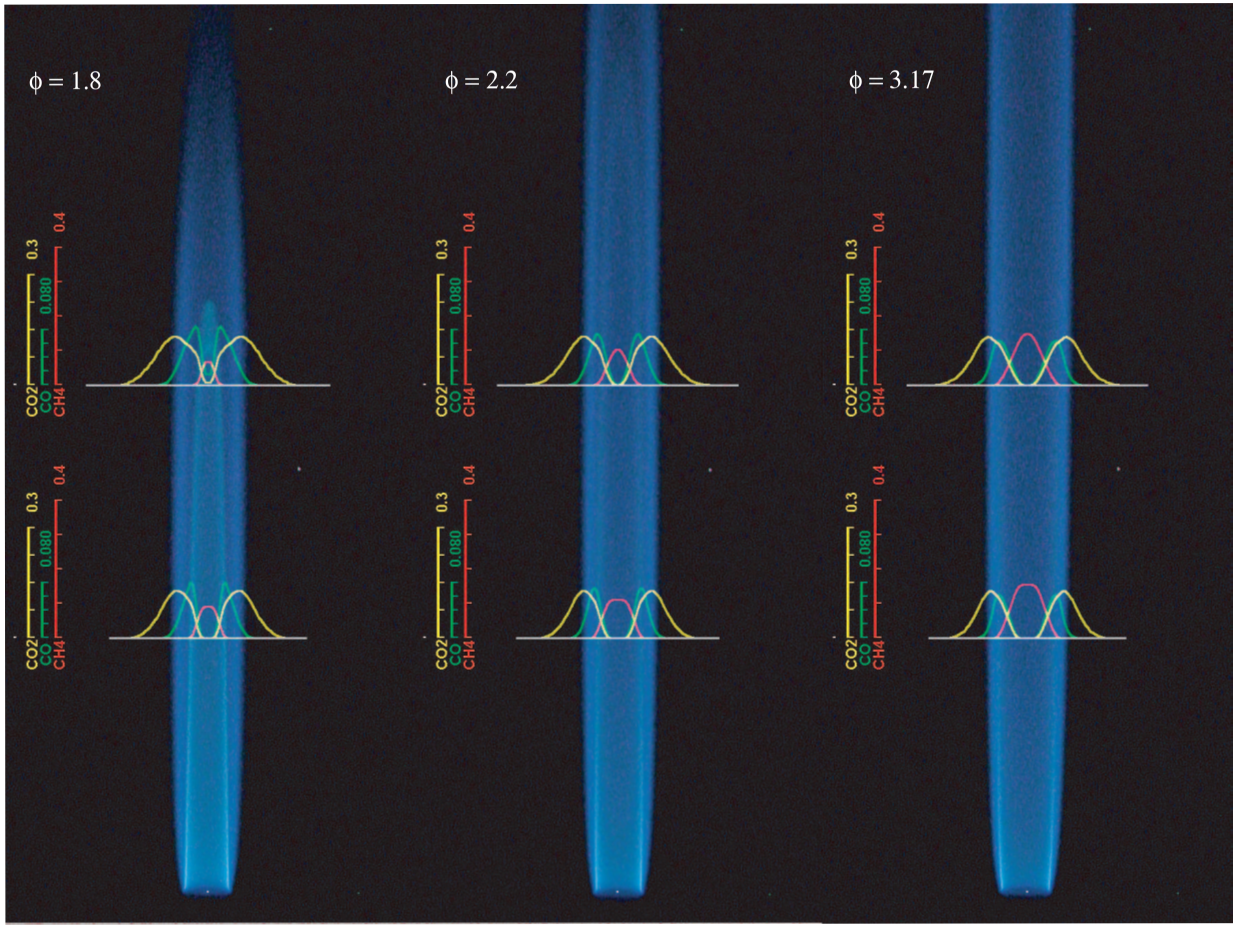

Figure 19. Experimental data product: CO, CO_2, and CH_4 mass fraction overlay onto flame photographs. Data from 50 mm and 100 mm above the nozzle exit. Partially premixed flame from Combustion Research Facilities, with the permission of Adonios Karpetis.

Axial convection

Nonetheless, the comparison of the experimental data and calculations in the physical space have some limitations. As seen above, the experiments are limited to phenomenology on a fixed number of species in the flow. The simulations are also limited as differences arise at low equivalence ratio. The differences between the opposed jet problem in one dimension and the axisymmetric flame from experiments are not due to the initial parameter such as cold strain rate, but to the neglected axial convection present in the axisymmetric case.

The similarity solution reduces the problem to one dimension. In the flame reactions are balanced with diffusion. Again examining the species equation from Chapter III, equation 3.10:

$$\begin{aligned} \rho u \frac{dY_i}{dz} + \frac{d}{dz}(\rho Y_i V_i) \quad &= \dot{\omega}_i \\ \text{convection} + \text{diffusion} \quad &= \text{reaction} \end{aligned}$$

Outside the flame convection balances diffusion. This is illustrated here with figure 20.

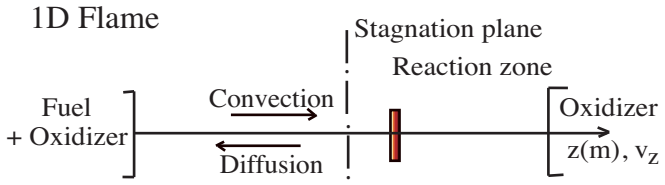

Figure 20. Convective and diffusive fluxes in a 1-D opposed jet flame. Convection balances diffusion outside the flame region.

When looking at the axisymmetric jet (figure 21), the fuel jet as a greater velocity than the oxidizer entrained from the outside. In two dimensions, convection and diffusion outside of the reaction zone are present in both the axial and radial direction.

Axial convection neglected with the 1D similarity solution may play an important role in the flame structure. It may be the reason why the temperature gradient on the fuel side could not be captured with the present 1D simulations.

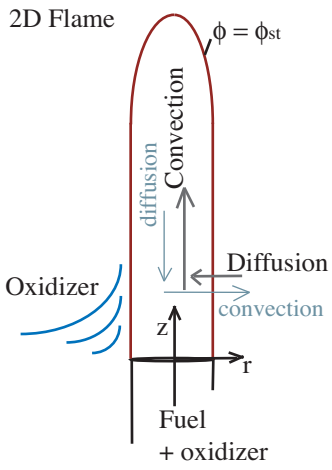

Figure 21. Convective and diffusive fluxes in a 2-D axisymmetric jet flame. Relative importance of convection versus diffusion in both axial and radial direction.

The equations in 2-D show convection and diffusion terms as function of both radial and axial direction. Using dimensional scaling arguments, it is shown that the axial diffusion can be neglected as well as radial pressure variations, Kee et al. (2003). The species conservation equation in axisymmetric coordinate system is:

$$\rho u \frac{\partial Y_k}{\partial z} + \rho v \frac{\partial Y_k}{\partial r} + \frac{1}{r} \frac{\partial (r \rho Y_k V_{k,r})}{\partial r} = \dot{\omega}_i \tag{4.3}$$

$$\text{axial convection} + \text{radial convection} + \text{radial diffusion} = \text{reaction}$$

where (u, v) are the two component of velocity in the (z,r) plane.

Originally, Burke and Schumann (1928) started to studied non-premixed flames in a coflow. In their experimental set up, the co-flow of air was varied to create over or under-ventilated flames. The analytical solution of this 2-D problem confirmed

that the flame height would vary with Peclet number, i.e. the ratio of convective to diffusive transport in the flame. When the mass flux of the jet stream is increased, convection in the streamwise direction dominates the diffusion in that direction. In the original Burke-Schumman formulation, the streamwise diffusion was simply neglected. Later, Chung and Law (1984) performed the same analysis without that assumption and achieved the same conclusions.

The ultimate treatment for axisymmetric flames would be to solve the PDEs in a two dimensional system. Excellent work has been done in this area by Bennett et al. (2000). Altough one of the disadvantages is the computational time, e.g. it would take a few days to run only one case. To analyze the engine performance under varying conditions requires a parametric variation and thus several cases to be run in a short time. Moreover, the 2-D treatments use simplified or skeleton reaction mechanisms. The advantages of the present simulations are the short computational time and the detailed-chemistry mechanism.

As suggested by B. Kee (Kee et al.; Minh et al., 2008), the compromise would be to solve the problem of axisymmetric flames in two dimensions using boundary layer approximation techniques. The Differential Algebraic Equations (DAE) will be solved and the present simulations used for the detailed-chemistry calculations. This approach is left for future work.

In conclusion, the similarity solution in one dimensional solution allows for fast computations with detailed chemistry. The main benefit of computational time enables studies with wide parametric variation. Yet the comparison of axisymmetric laminar flames experiments to opposed jet flow simulations does not yield satisfactory results in physical space.

CHAPTER V

FLAME SCALAR STRUCTURE

While the comparison of 2-D experiments to 1-D computations proves somewhat problematic in physical space, a better agreement can be achieved by examining the scalar structure of the flame, i.e. by examining the thermochemistry results in a scalar axis.

Flamelet approach

The equations describing the reacting flow problem in chapter III are highly non-linear PDEs. The source terms $\dot{\omega}_i$ are mainly responsible for the complexity of the problem. With the present state of the calculations, this term is a vector of 53 species by 325 reactions.

Recalling the species conservation equation in vector form:

$$\rho\frac{\partial Y_i}{\partial t} + \rho\bar{u}.\nabla Y_i - \nabla.(\rho D_i \nabla Y_i) = \dot{w}_i \tag{5.1}$$

Choosing a variable ξ, conserved scalar that does not react in the flame, the dependent variable Y_i is replaced and the reaction terms $\dot{\omega}_i$ are identically zero, realizing here the separation of the fluid flow from the chemistry problem.

$$\rho\frac{\partial \xi}{\partial t} + \rho\bar{u}.\nabla \xi - \nabla.(\rho D_\xi \nabla \xi) = 0 \tag{5.2}$$

Without the source term, the equation is easily solved. The change in variables can be summarized as:

$$\pounds(Y_i) = \dot{\omega}_i \quad \longleftrightarrow \quad \pounds(\xi) = 0$$

where the linear operator $\pounds$ acting on Y is:

$$\pounds(\cdot) = [\frac{\partial \rho}{\partial t} + \rho\bar{u}\frac{\partial}{\partial z} - \frac{\partial}{\partial z}(\rho D_\xi \frac{\partial}{\partial z})](\cdot) \tag{5.3}$$

The main assumption is the equal diffusivities of chemical speces i: $D_i = D_\xi$.

The flamelet mapping is a non-unique *ad hoc* relationship. The originality of the present work is in the formulation of the conserved scalar. The variable ξ could be a combination of elemental mass fraction or a single element such as Z_H:

$$\rho\frac{\partial Z_H}{\partial t} + \rho\bar{u}.\nabla Z_H - \nabla.(\rho D_{Z_H}\nabla Z_H) = 0 \tag{5.4}$$

using the assumption of a single diffusivity D_{Z_H} for the non-reactive scalar. The conserved scalar Z_H is defined in the present study as the atom of hydrogen. At any point in the flame the number of hydrogen atoms should vary from the maximum value at the fuel inlet to zero at the oxidizer inlet[1]. The value of Z_H should be conserved, meaning no atom would be created, or destroyed. The atoms are transfered from the fuel molecules to the intermediates species containing hydrogen, and finally to water molecules in the products (Rosner, 1986).

Past studies have used the Bilger mass fraction, where the conserved scalar, ξ_B is a combination of the mass fractions of different elements such as the carbon, hydrogen, and oxygen atoms (Bilger et al., 1990):

$$\xi_B = \frac{2(Y_C - Y_{C,2})/w_C + (Y_H - Y_{H,2})/2w_H - (Y_O - Y_{O,2})/w_O}{2(Y_{C,1} - Y_{C,2})/w_C + 2(Y_{H,1} - Y_{H,2})/2w_H - 2(Y_{O,1} - Y_{O,2})/w_O} \tag{5.5}$$

where Y are elemental mass fractions of carbon, hydrogen and oxygen, w are the respective atomic weights, and subscripts 1 and 2 refer to the fuel and co-flowing air

[1]On the oxidizer side, there is no atoms of hydrogen. I assume here that there is no humidity and the oxidizer is air composed of pure oxygen and nitrogen.

streams respectively. The variable ξ_B takes values between zero at the oxidizer side and one at the fuel side. Later Barlow et al. (2005) modified Bilger's formulation by eliminating the atomic oxygen mass fraction.

I define the conserved scalar, ξ as a single element mass fraction: $\xi = Z_H$. Unlike past studies, the scalar is not normalized. This scalar definition brings out the similarities of flames with different equivalence ratio. The term flamelet is used here for every mapping between the thermochemistry (temperature and chemical species) and the conserved scalar Z_H. Figure 22 shows the comparison between normalized and primitive scalar: the data collapses on the lean side of the flame and differences appear only on the rich side of the flame. The variation of fuel in the partially-premixed jet results in different final values of Z_H.

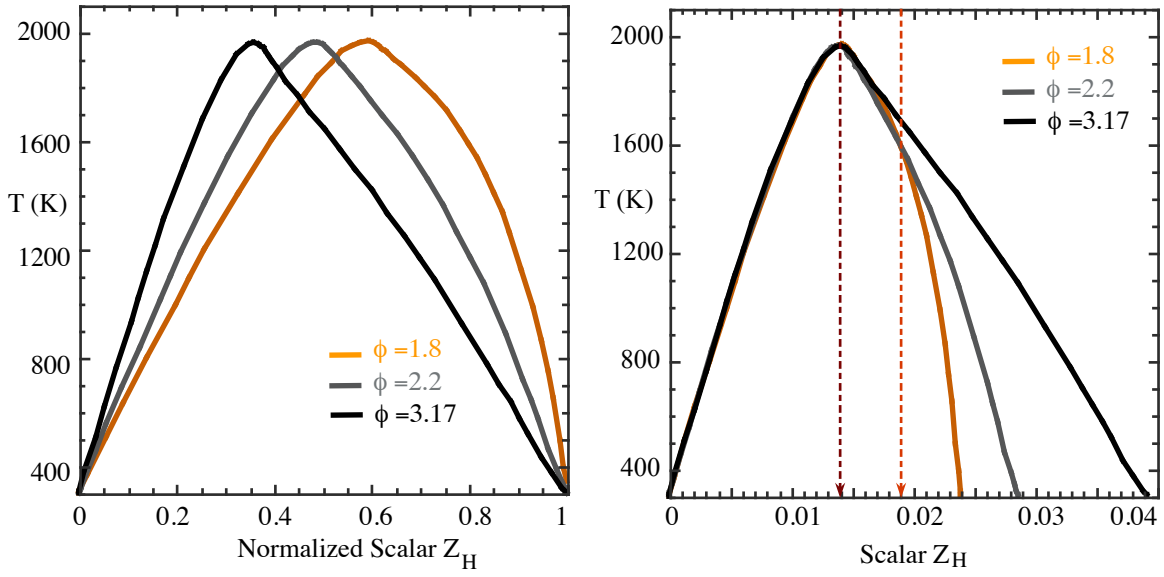

Figure 22. Flamelet profile comparing the normalized with primitive scalar. The three flamelets plotted are for ϕ of 1.8, ϕ of 2.2, and ϕ of 3.17. Simulations case (c), d=8 cm.

The scalar dissipation is defined as:

$$\chi = 2D_{\xi}(\nabla\xi \cdot \nabla\xi) \tag{5.6}$$

It quantifies the rate of molecular mixing of the scalar (ξ) and is similar to a time scale: the inverse of the diffusion time. The scalar dissipation appears in the flamelet equation originally derived by Bilger in 1977 (Bilger, 1976a). The derivation starts with the species conservation equation for the scalar ξ or for the temperature, T, using the assumption of unity Lewis-number ($Le_i = \lambda/c_p\rho D_i) = 1$).

$$\rho\frac{\partial\xi}{\partial t} + \rho\bar{u}.\nabla\xi - \nabla.(\rho D_{\xi}\nabla\xi) = 0 \tag{5.7}$$

$$\rho\frac{\partial T}{\partial t} + \rho\bar{u}.\nabla T - \nabla.(\rho D_{\xi}\nabla T) = \sum_{k=1}^{M}\frac{q_k\dot{\omega}_k}{c_p} \tag{5.8}$$

where q_k is the heat of reaction k. The time derivatives are assumed to vanish as well as the radiation term. The independent variables (x,y,z) are transformed with a new coordinate system normal to the surface of the stoichiometric mixture.

$$\frac{\partial}{\partial x} = \frac{\partial\xi}{\partial x}\frac{\partial}{\partial\xi}$$

As explained by (Peters, 1998), the Crocco transformation is used to formulate a new set of equations:

$$-\rho\frac{\chi}{2}\frac{d^2T}{d\xi^2} = \sum_{k=1}^{M}\frac{q_k\dot{\omega}_k}{c_p} \tag{5.9}$$

If the reactions are assumed to be infinitely fast, the second derivative is negative and indicates a maximum as shown in figure 23. This single point correspond to the flame temperature of a single equilibrium reaction. For regions where there is no reaction, i.e. the source term $\dot{\omega}_k$ is equal to zero, the second derivative is zero and the

solution should show a linear relationship between the temperature and the scalar.

$$\dot{\omega}_k \to \infty \quad \Rightarrow \quad \frac{d^2T}{d\xi^2} \to -\infty \quad \Rightarrow \quad reaction$$

$$\dot{\omega}_k = 0 \quad \Rightarrow \quad \frac{d^2T}{d\xi^2} = 0 \quad \Rightarrow \quad T = f(\xi)$$

In general the flamelet will lead to this simple description of the flame structure: a straight line represents the absence of reaction; the regions with curvature represents a reaction.

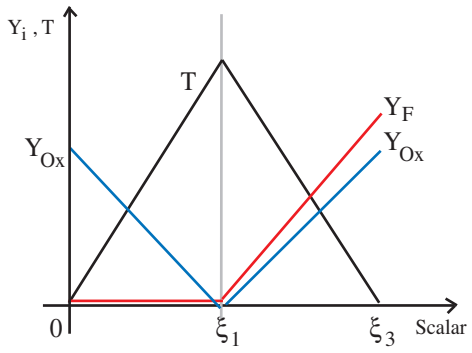

Figure 23. Schematic of an equilibrium flamelet.

In the present case the scalar is zero on the oxidizer side, where no hydrogen atoms are present. The last value of the scalar (ξ_3) varies with the amount of fuel in the mixture. This position can be determine using the stoichiometric rich premixture value:

$$\phi \mathrm{CH_4} + 2\mathrm{O_2} + 7.43\mathrm{N_2}$$

where

$$\xi_3 = \ Z_{H,3} \ = \frac{4\phi}{16\phi + 272}$$

The position (ξ_1) corresponding to the peak flame temperature can be determined by

the overall stoichiometric methane oxidation

$$CH_4 + 2O_2 + 7.43N_2 \longrightarrow CO_2 + 2H_2O + 7.43N_2$$

$$\xi_1 = Z_{H,1}^{eq} = \frac{4}{16 + 272} = 0.0138$$

To continue building the flamelet mapping, the position of the second reaction zone needs to be calculated with a simple reaction. Examining the water-gas-shift reaction described in chapter IV as:

$$CO + H_2O \quad \leftrightarrow \quad CO_2 + H_2$$

it should produce CO or H_2 depending on the sign of the progress of reaction variable $\omega^{'}$ or direction of the reaction. Using the calculations and extracting the progress of reaction variable of the water-gas-shift reaction[2] ($\omega_{WGSR}^{'}$) this hypothesis is not fully confirmed. Figure 24 shows the progress of variable in scalar space. The first maximum corresponds to the main reaction zone, indicating that the reaction would increasingly shift to the right as ϕ increases. The minima corresponds to the reaction shifting to the left, or producing CO and H_2O. The CO production should subsequently increase as ϕ increases, but this is refuted by the CO trend seen in the experimental and computational results (see figure 25 and 26). The second maxima corresponds approximately to the second reaction zone (as defined by the bend in temperature profile) and indicates a shift of the reaction to the right or production of CO_2 and H_2. Indeed this time the trend is confirmed by the H_2 concentrations. The decrease in production with increasing ϕ might be related to the decreases in H_2 mass fraction as will be seen in figure 25.

[2]The net progress of reaction variable $\omega_{WGSR}^{'}$ is determined by adding the net progress of reaction variable for the CO oxidation reaction ($CO + OH \leftrightarrow CO_2 + H$) to the shuffle reaction: $H + H_2O \leftrightarrow OH + H_2$.

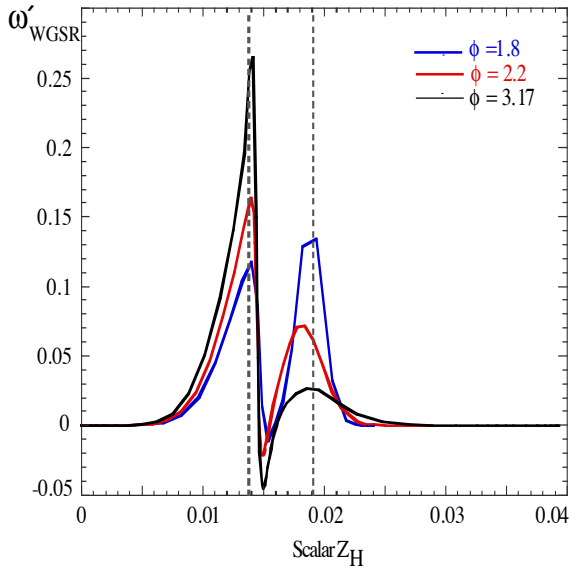

Figure 24. Net progress of reaction variable for the water-gas-shift reaction in scalar space.

Although the water-gas-shift reaction might be involved, it does not explain all the trends seen in the second reaction zone. Both the experiments and simulations show concentration of intermediate species peaking in the rich premixed zone before the main reaction zone. Figure 25 and figure 26 show the simulation and experimental results for the three flames under study. In both cases CO, H_2 and H_2O flamelets show a bend. The curvature seen in the figure around $Z_{H,2} \approx 0.018$ points to a reaction as described by the flamelet equation. It is possible that the partial oxidation of methane is responsible for the production of intermediate species and the displacement of the temperature profile. As shown in the schematic figure 27, the heat released from this partial oxidation would increase the temperature.

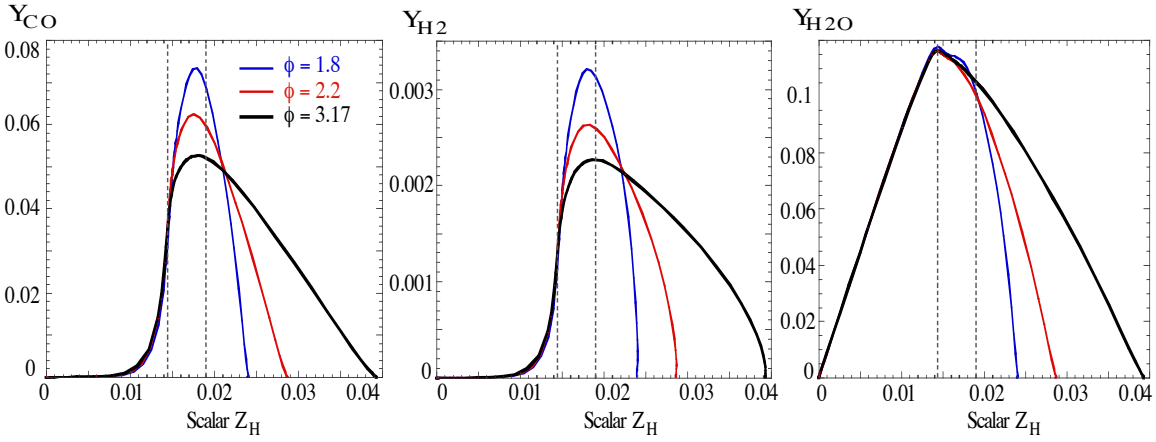

Figure 25. Flamelet of species CO, H_2 and H_2O, simulation results. The vertical line at z_H=0.0138 marks the location of peak flame temperature. The vertical line at z_H=0.018 marks the possible location of second reaction zone. Numerical simulation case (b), d=1.95 cm, varying ϕ.

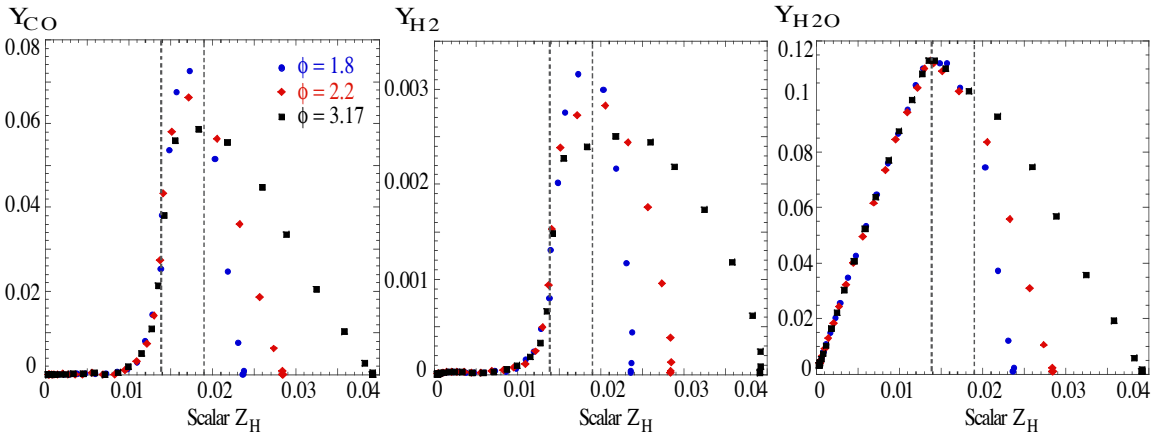

Figure 26. Flamelet of species CO, H_2 and H_2O, experimental results.

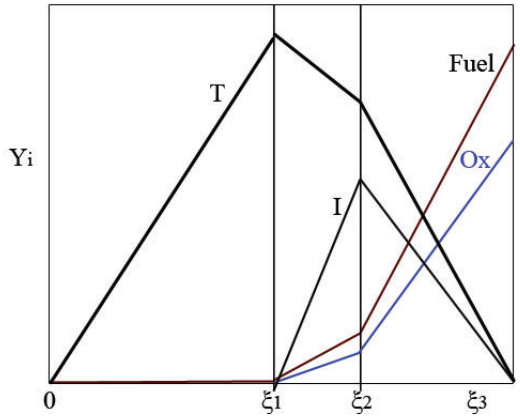

Figure 27. Schematic of the second reaction zone (ξ_2) in scalar space.

Li & Williams Li and Williams (1999) propose an overall order of that reaction in the form:

$$\phi CH_4 + 2O_2 + 7.43N_2 \longrightarrow \phi CO + (3\phi - 4)H_2 + (4 - \phi)H_2O + 7.43N_2$$

Upon full completion, that reaction would predict an increasing equilibrium mass fraction for CO with increasing ϕ, while the opposite trend can be seen in the measurements. We identify another global reaction step as the most likely candidate for a unique second premixed zone, namely the reaction Peters (2000):

$$CH_4 + \frac{3}{4}(2O_2 + 7.43N_2) \longrightarrow CO + 2H_2O + \frac{3}{4}7.43N_2$$

This predicts a position for the rich premixed zone at $Z_2 \approx 0.018$ for all flames in agreement with the experimental data. Yet another advantage of the global step mentioned above is the correct prediction of the maximum CO production in the flames, taking place at the same location in scalar space. Its main drawback is the inherent lack of H_2 production, since all hydrogen is supposed to be converted to

water by the above chemical reaction. It should be emphasized that such extremely reduced representations of the complicated chemical kinetics that take place in a flame would be useful for industrial-type computations, where only few major species would be accounted for, and where multiscalar experiments and/or detailed-chemistry computations such as the ones presented here are completely impractical. This simple scalar structure enables the visualization of the double flame structure[3]. Ultimately the flamelet mapping will enable the resolution of the thermochemistry in the flame ($Y_i = f(\xi)$) when given the variation of the scalar in space ($Y_i = f(\xi(z,t))$. So when non-reactive species are traced in a complex geometry flow, the thermochemistry may be inferred from the scalar variation through the flamelet mapping and for example the amount of CO might be predicted. With the available flamelet mapping of the partially premixed flames under study, radiation and cross-transport effects can now be analyzed in scalar space.

Results of radiation models on the scalar structure

The first simulations using the partially-premixed flame examples from Cantera showed a difference in the peak temperature of 90 K. Figure 28 shows the differences in temperature profile between the experimental data from Sandia laminar flames and Cantera simulation case[4] (b) with a value of ϕ=3.17. The radiative numerical results are plotted with a dashed line. They show a better fit to the experimental data which is plotted with red dots. In agreement with past research, figure 28 shows a net decrease in temperature throughout the flame and a maximum decrease in peak temperature by 110 K, as compared to the adiabatic calculations, previous simulation are plotted

[3]If fuel was added to the oxidizer side, this would lead to the triple flame structure as described by Qin et al. (2004).

[4]See chapter IV for the parameters tabulation.

with a dashed line. The optically-thin radiative model show closer results than an optically-thick model which would show somewhat higher temperatures overall.

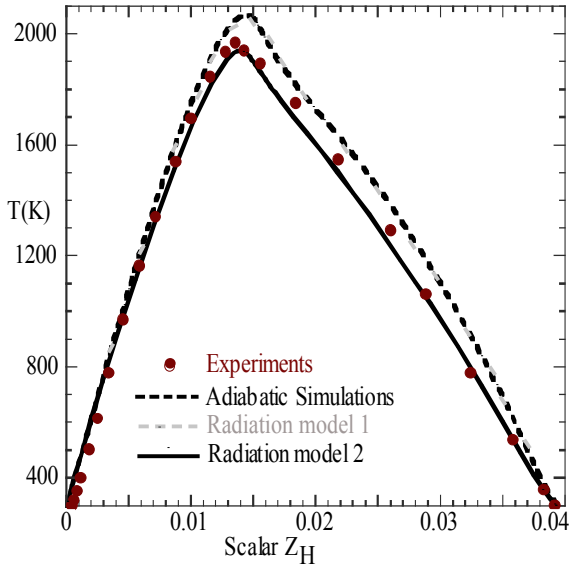

Figure 28. Comparison of radiation models adiabatic simulations. Case (b), d= 1.95 cm, ϕ=3.17, and experimental data in scalar space.

The radiative heat flux equation from chapter III evidently exhibits a strong dependence on temperature, yet the additional effect of the mole fractions and the Planck mean absorption coefficients should not be overlooked.

$$\nabla . \bar{q_r} = 4\sigma \sum a_{p,i} p_i (T^4 - T_b^4)$$

In order to examine that effect, opposed-jet simulations results for two adiabatic flames are used to calculate each term of the heat flux equation. These simulation results do not include the radiation model described above, rather the radiative terms are calculated from the adiabatic solution. When the radiative heat loss shown in the example below (figure 29) is calculated through the flame domain two factors affect its value: the temperature and the product of mole fractions with Planck coefficients.

Results are plotted in physical space with the fuel side on the left and the oxidizer side on the right. The temperature peak location is shown by the black vertical line at z=10 mm. Acknowledging that the dependency of radiation on wavelength is already accounted for, notice the Planck mean absorption coefficient dependency on temperature, figure 8 in chapter III. The four species have a higher coefficient for temperature below 1500 K. Therefore, the term $\sum a_i P_i$ has stronger effect outside of the peak flame temperature, as seen in figure 29b. The main products, CO_2 and H_2O, will play a greater role on the outside of the thin flame region because of their larger mass fraction. CO and CH_4 mole fraction add to the effect on the rich premixed side of the flame. In the radiative flux equation the temperature is raised to the forth power thus will have the strongest effect with the maximum temperature at the location of the flame front. Figure 29c, shows the total heat of radiation. Due to high temperature at the flame peak, previous trends are undermined. This example illustrates the combined effect of Planck's mean-absorption coefficient and the flame peak temperature on radiative flux. The resulting total reduction in temperature and unequal decrease in flame thickness will be seen in both physical space and scalar space.

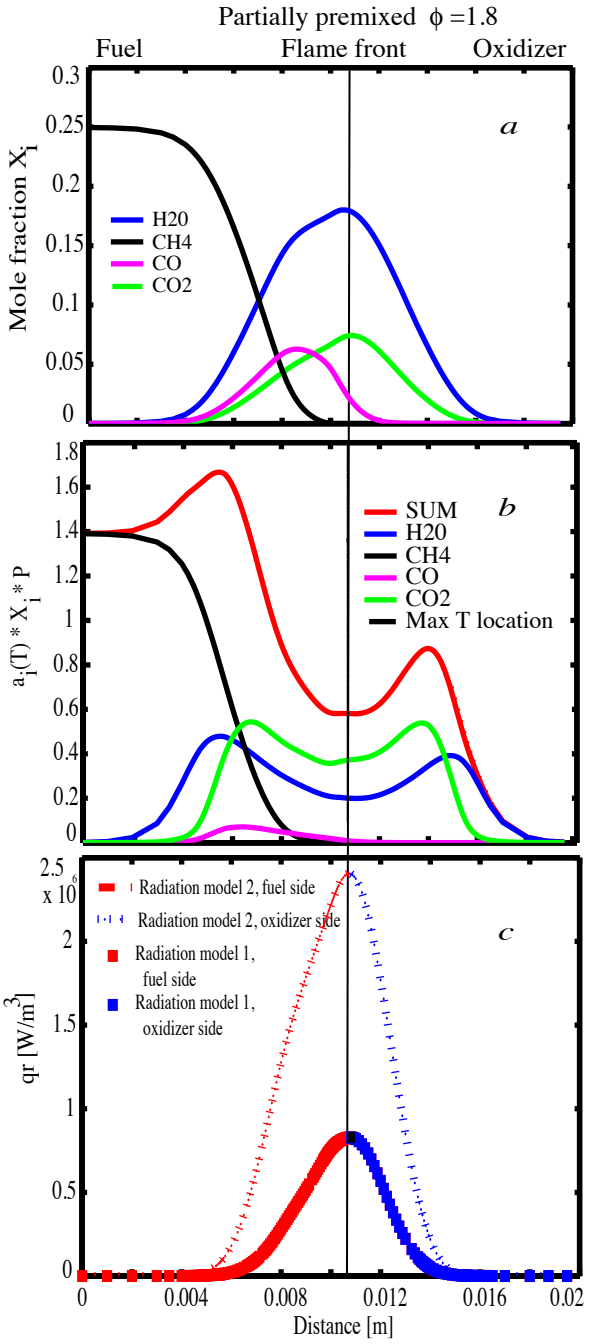

Figure 29. Steps in the calculation of radiative heat flux. Case (b), d=1.95 cm, $\phi = 1.8$, spatial structure. Figure **a** shows mole fraction of species. Figure **b** shows mole fraction times Planck's coefficient. Figure **c** shows the total heat of radiation. Flame peak temperature is shown by the vertical line.

Comparison of the two radiation treatments

Radiative heat flux for model 1 (plotted with square symbols) and 2 (dashed line) are shown in figure 29c. Comparing the peak value of q_r, model 2 radiative heat loss should be three times larger than model 1. A few test cases have been used to verify the validity of the models. A burner stabilized ethane flame was studied as well as an opposed-jet methane-air non-premixed flame. The different flame configurations have in common the numerical solution that employs the stagnation flow configuration. Indeed the modification in Cantera software package was included in the stagnation flow routine only and not in propagating flame solutions.

The effects of the radiation model and adiabatic simulations are shown in table V and briefly discussed.

Table V. Comparison of radiative treatment for different test cases. Cantera simulations results. Peak temperature of the flame is given in Kelvin. The solution grid points are indicated in parenthesis

Flame type	Adiabatic Case	Radiation Model 1	Radiation Model 2
Burner stabilized C_2H_6 flame	1990 (177)	1989 (182)	1989 (182)
Opposed jet non-premixed methane/air flame	2063 (199)	2058	2001(187)
Opposed jet partially-premixed methane/air flame $\phi = 3.17$	2061 (41)	2052 (41)	1950 (41)
	2066 (173)	2057 (173)	1955 (173)

Radiative heat transfer shows a small effect for the ethane burner stabilized. For the opposed-jet methane flames, both non and partially-premixed flames, the

radiative heat flux effects are more pronounced with the RADCAL-based model, particularly in the case of the partially premixed flames where the peak flame temperature decreases by 110 K (figure 28). The inclusion of a RADCAL-based heat loss model yields a better agreement between numerical and experimental results. The importance of grid refinement should not be overlooked as a under-resolved grid may lead to erroneous temperatures.

Major results

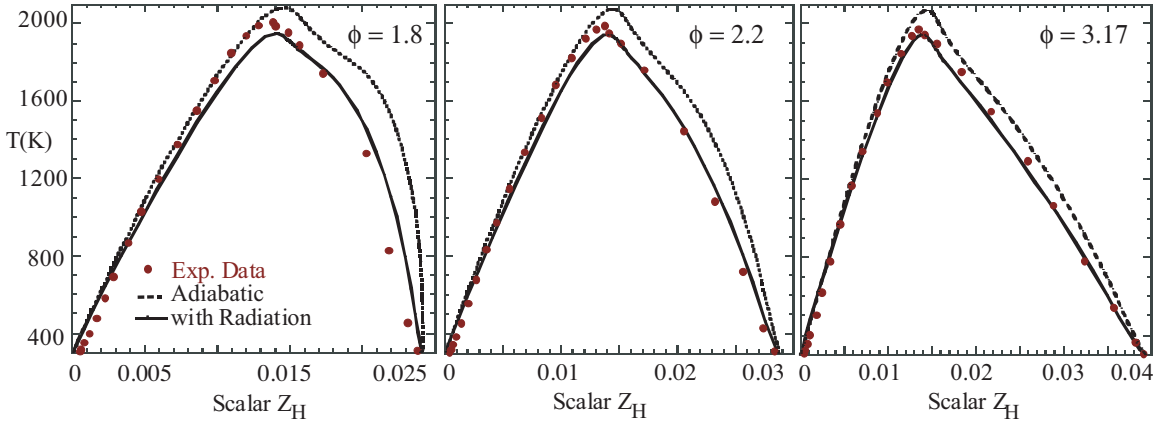

Figure 30. Comparison of the scalar structure from experimental data, adiabatic and radiative simulations. Case (b), d= 1.95 cm, variation of ϕ, radiation model 2.

Not only the maximum temperature but the structure of the flame itself is affected:

- The peak temperature moves slightly toward the rich side, i.e the left side in physical space;
- The whole temperature profile shrinks;
- The second reaction zone appears further away from the rich side and closer to the main reaction zone.

When examining the scalar structure, the radiative treatment provides a better comparison with the experimental data. Figure 30 shows the change in the temperature profile of the flame as premixture strength increases. One can see the effect on flame width and peak temperature.

A similar effect can be identified when examining the spatial structure, as shown in figure 31 where the temperature and water mass fraction results are plotted against the flow axis. For all three premixture strength, the profile width decreases. H_2 and CO are markers of the second reaction zone. One can see a small shift in the location of the peaks as the general structure of the radiative flame shrinks.

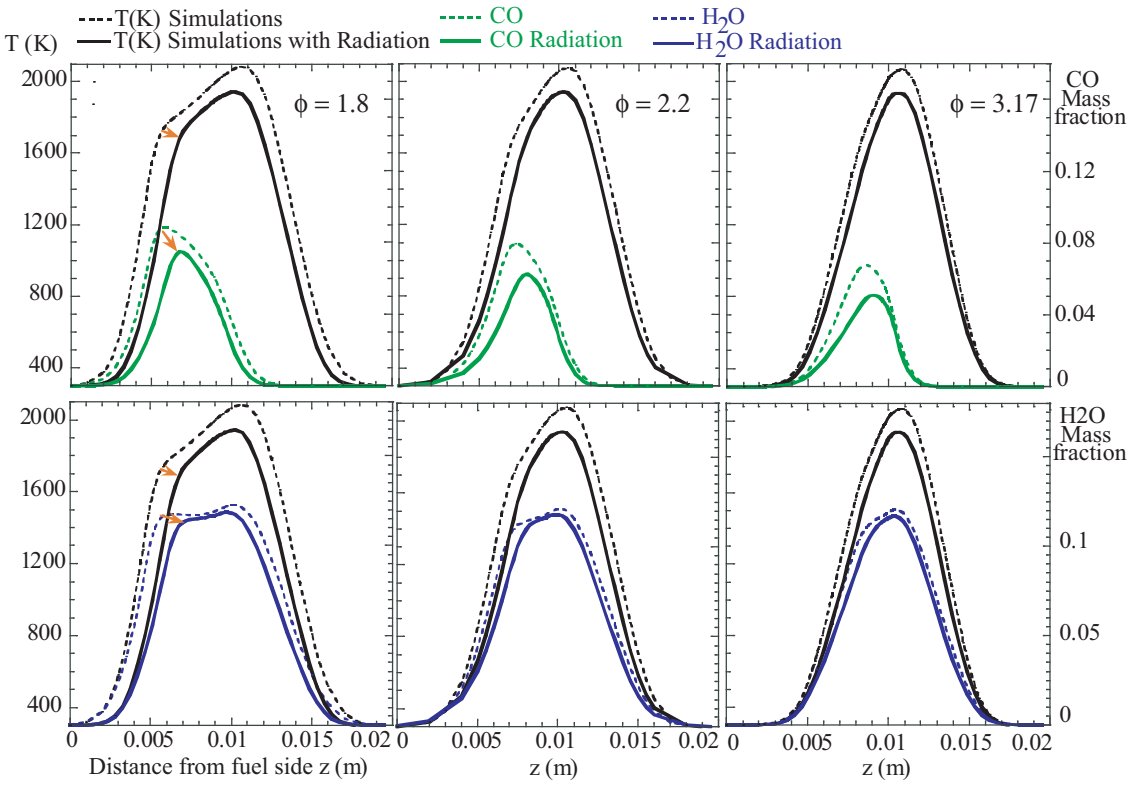

Figure 31. Comparison of flame spatial structure from adiabatic and radiative calculations. Case (b), d= 1.95 cm, variation of ϕ, radiation model 2. The x-axis is the flow axis with fuel premixture on the left side and oxidizer on the right side.

The radiation-treatment improvement on the double flame structure can be seen in the scalar space with a plot of the variation of premixing strength as illustrated by figure 32. The second reaction zone is slightly shifted closer to the flame, or farther from the rich side to $Z_H = 0.018$.

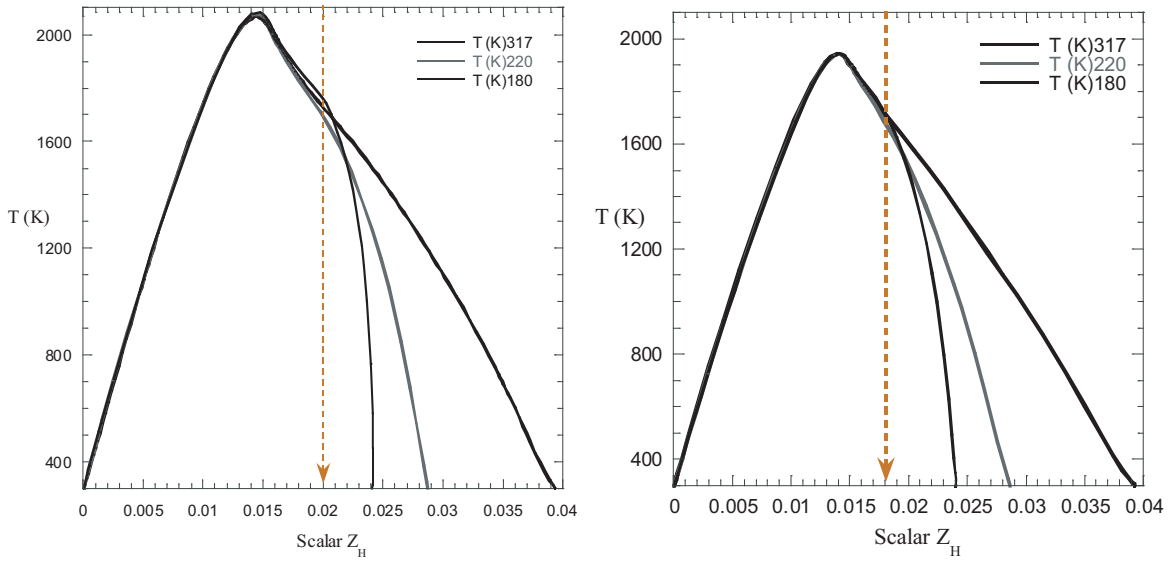

Figure 32. Parametric variation of ϕ with adiabatic and radiative Cantera simulations.

Examining figure 31, the effect of radiation in the rich partially premixed zone is larger at low ϕ but not enough to perfectly match the data. At larger ϕ, the effect is smaller but almost underpredicts the data. The curvature on the rich side at ϕ=1.8, is diminished due to the inclusion of species-dependent radiation as explained in section . It confirms the findings of Barlow et al. (2001) and Zhu et al. (2002) with respect to Sandia Tsuji flames. The study used ChemKin as a simulation tool. In a few references (Barlow et al., 2001; Daguse et al., 1996) self-absorption in this type of flame was considered of importance and was assumed responsible for the discrepancy at low strain. But a later study by Kim et al. (2003) investigated different radiation model including self-absorption, such as weighted sum of gray

gas model and made a comparison with the optically-thin model. The opposed-jet reacting flow problems studied were methane diffusion flames at varying flow rates and partially premixed flames at ϕ of 2 and 4. Their conclusion indicated clearly that self-absorption does not affect the flame structure. If self-absorption is ruled out, the questions still remains as to why the radiation treatment is less effective on the rich side at low equivalence ratios. Based on figure 29b, it is possible that the product of mole fractions and Planck's mean absorption coefficients is responsible. It is left to future work to investigate a different radiation heat loss equation or different radiation model.

Discussed in the literature, radiation models might have either a direct effect on species concentration or an effect on their formation rates (Zhu et al., 2002). This radiation effect was explored here for CO and NO concentrations specifically. The production rate of both species and reaction rates will be used to explain the effect of radiation on the NO and CO reaction mechanisms. From figure 31, it was noted that CO mass fraction decreases and shift. In figure 33 results for CO and CO_2 mass fraction are plotted in scalar space. The latter figure shows the effect of RADCAL-based radiation model on the intermediate species and the trend when the equivalence ratio ϕ is varied.

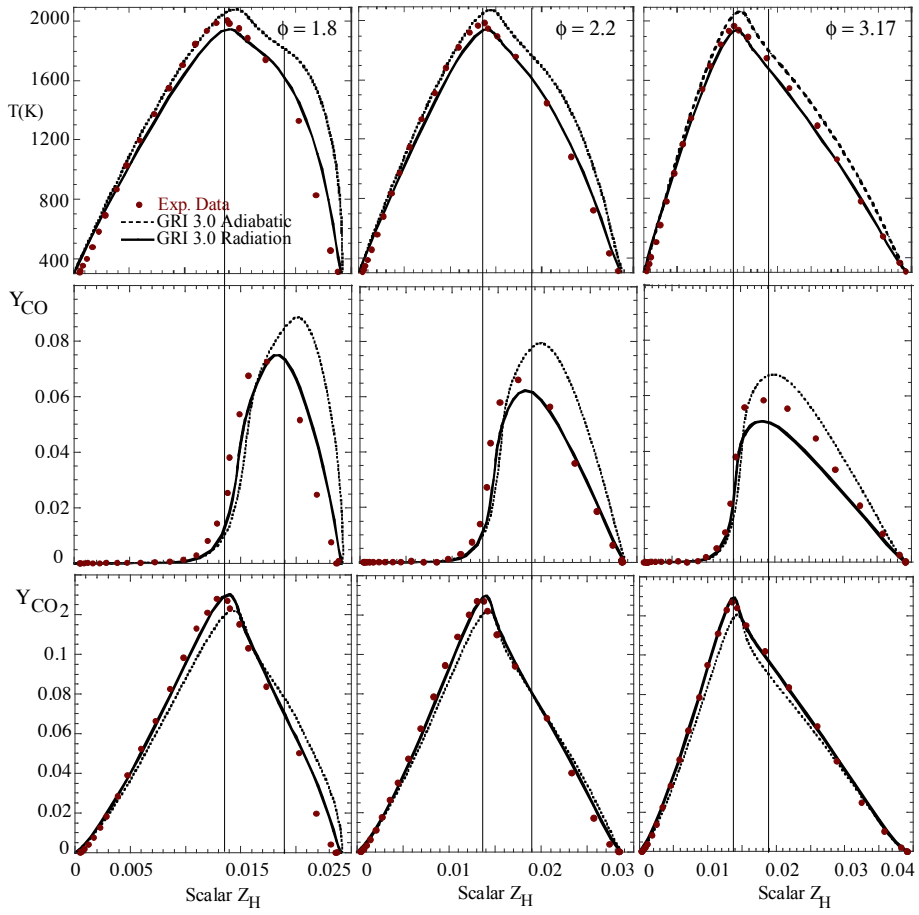

Figure 33. Effect of radiation model on intermediate species: temperature profile, CO, and CO_2 mass fraction in scalar space. Numerical simulation Case (b), d=1.95 cm, varying ϕ.

In agreement with previous studies, e.g. Barlow et al. (2001), we find that the GRI 3.0 mechanism over-predicts CO in adiabatic calculations. The implementation of radiative loss produces a better agreement between computations and experiments at least for the leaner flames, as shown in figure 33. As the premixture strength is increased, i.e. less air is added to the fuel in the partially premixed stream, the CO mass fraction tends to decrease. This is a counter-intuitive trend that has been shown in past studies (Karpetis and Barlow, 2003; Datta et al., 2004) and which is qualitatively captured by the GRI 3.0 calculations, both adiabatic and radiative. Including

radiation preserves this trend of decreasing CO for increasing ϕ, and produces a better quantitative agreement for the flames (excluding the richer case $\phi = 3.17$). At richer ϕ, CO is under-predicted as noted by Zhu et al. (2002). The question arises as of why the radiative heat loss has such a strong effect on the CO species at $\phi = 3.17$. Examining the CO formation by plotting the net molar production/destruction rate, $\widehat{\omega}_{CO}$, versus the scalar axis in figure 34, shows the same counterintuitive trend, i.e. CO production decreasing with increasing premixture strength, and the same general effect of the radiation model, i.e. decreasing the net CO production and shift in the second reaction zone. For the three equivalence ratios, the net production/destruction rate of CO has 3 peaks (figure 34): a first minima corresponding to the main reaction zone (where CO is consumed); a second peak between the main reaction zone and the second reaction zone; and a third maxima corresponding to the second reaction zone. As the premixing strength is increased the production of CO in the rich premixed zone decreases, resulting in the counterintuitive trend of decreasing CO mass fraction. It might be postulated that there exist a reaction responsible for the production of CO in the rich premixed zone and it has the time to occur at low equivalence ratios, when the two reaction zones are separated, and it is inhibited due to the increase in destruction rate at higher equivalence ratios.

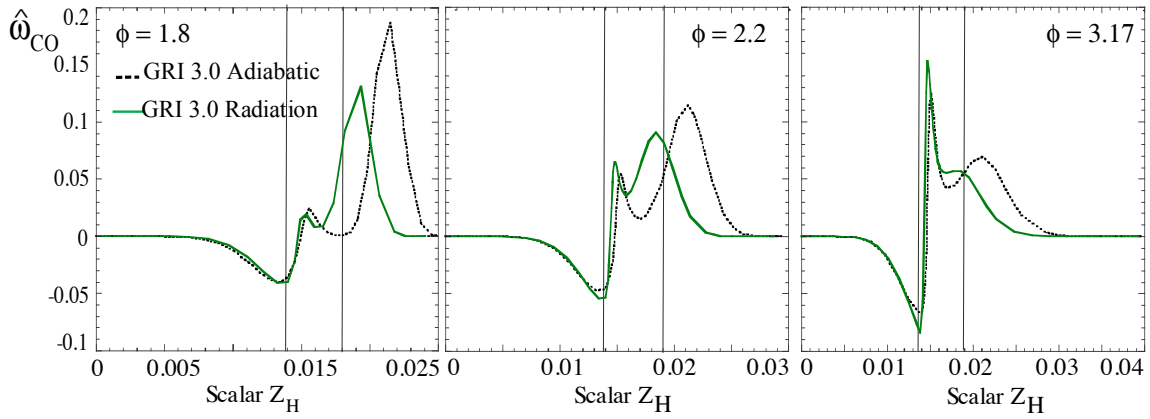

Figure 34. Effect of radiation model on intermediate species: net molar production/destruction rate of CO in scalar space. Case (b), d=1.95 cm, varying ϕ.

Another minor species of interest here is the pollutant NO. It exists in flames in small concentrations and it is rather difficult to measure experimentally, hence detailed-chemistry calculations such as the ones presented here are important for NO prediction. Nitric oxide (NO_x) formation and the reaction mechanisms involved in its generation have been the subject of numberous past studies (e.g. Li and Williams (1999); Kim et al. (2002); Ravikrishna and Laurendeau (2003)). At the beginning of this work, calculations with GRI 3.0 adiabatic mechanism over-predicted NO confirming the work by Zhu et al. (2002). As is evident from figure 35, the radiative calculations produce a better match with the experimental data, in the non-premixed high-temperature zone of the flame. Net molar production/destruction rates of species can be extracted from the flame results. In figure 36, $\widehat{\omega}_{NO}$ is plotted versus scalar space. A slight decrease in NO production can be seen at the peak flame temperature location. in between the two zone the minima, denoting a re-burn mechanism, increases with increasing ϕ. From the flamelet equation, this bend or curvature shown in scalar space (figure 35) could be associated with a reaction. As ϕ increases, the

reaction burning NO seems to be more and more pronounced: the difference between the maximum and minimum production/destruction rate increases.

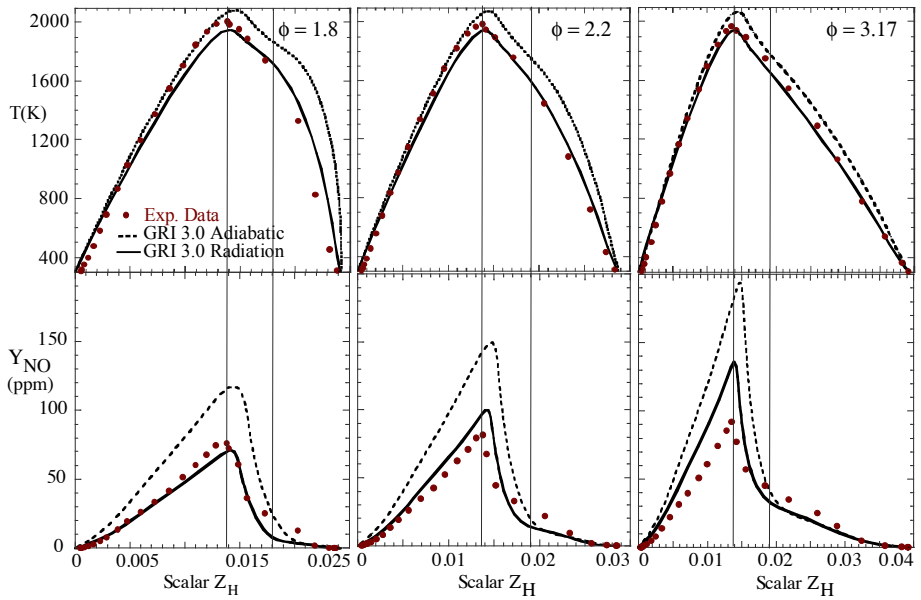

Figure 35. Effect of radiation model on intermediate species: temperature profile, NO mass fraction in scalar space. Case (b), d=1.95 cm, varying ϕ.

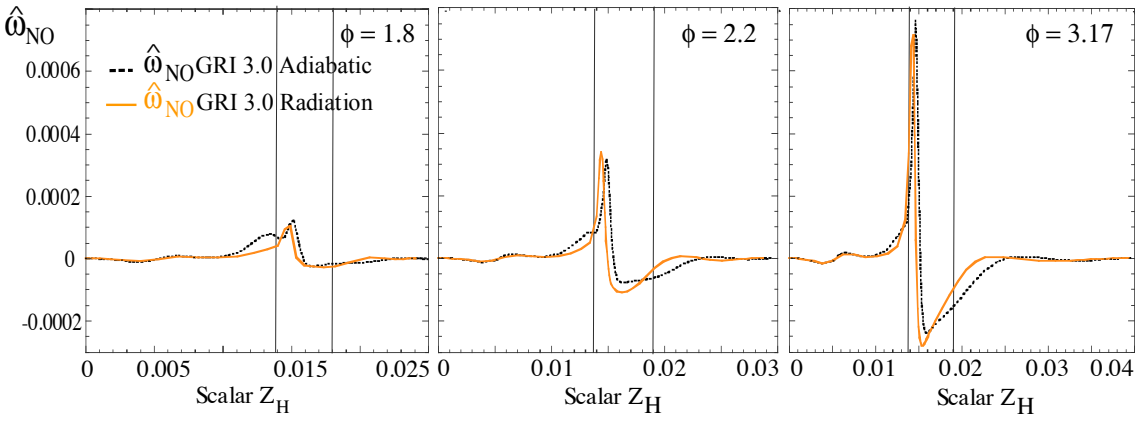

Figure 36. Effect of radiative treatment on intermediate species: net molar production/destruction rate of NO in scalar space. Case (b), d=1.95 cm, varying ϕ.

The global production of NO does not give enough information on the effect of the radiation treatment. By plotting the progress variables of the reactions responsible for NO formation, it is possible to better understand which reactions are affected by the decrease in temperature. The following figures show NO formation via the thermal (Zel'dovich) mechanisms (figure 37) and the prompt (figure 38). The thermal mechanism for NO formation consists of the following three main reactions. Once again progress of reaction variable ($\omega_k^{'}$) is plotted for each reaction producing NO (reaction T1: backward; reaction T2: forward; reaction T3: forward).

$$N + NO \leftrightarrows N_2 + O \ (T1)$$

$$O_2 + N \leftrightarrows O + NO \ (T2)$$

$$OH + N \leftrightarrows H + NO \ (T3)$$

While reaction T3 is only slightly affected, reaction T1 of the thermal mechanism is largely affected. The adiabatic trend of this reaction is a decrease with increasing ϕ, while the radiative reaction T1 has approximately the same value for all ϕ. In contrast, the reaction T2 adiabatic and radiative trend is an increasing positive progress of reaction variable with increasing ϕ. The effect of the radiation treatment is more pronounced in this reaction at low ϕ and inversely effective at larger value $\phi = 3.17$. One can deduce that in the radiative calculations, the initial reaction T1 is reduced for all equivalence ratio but the conversion of oxygen and nitrogen atoms to NO via the reaction T2 is only reduced at low equivalence ratio. For $\phi = 3.17$ the progress of reaction variable for reaction T2 is actually increased and responsible for NO formation resulting in an over-prediction of NO mass fraction.

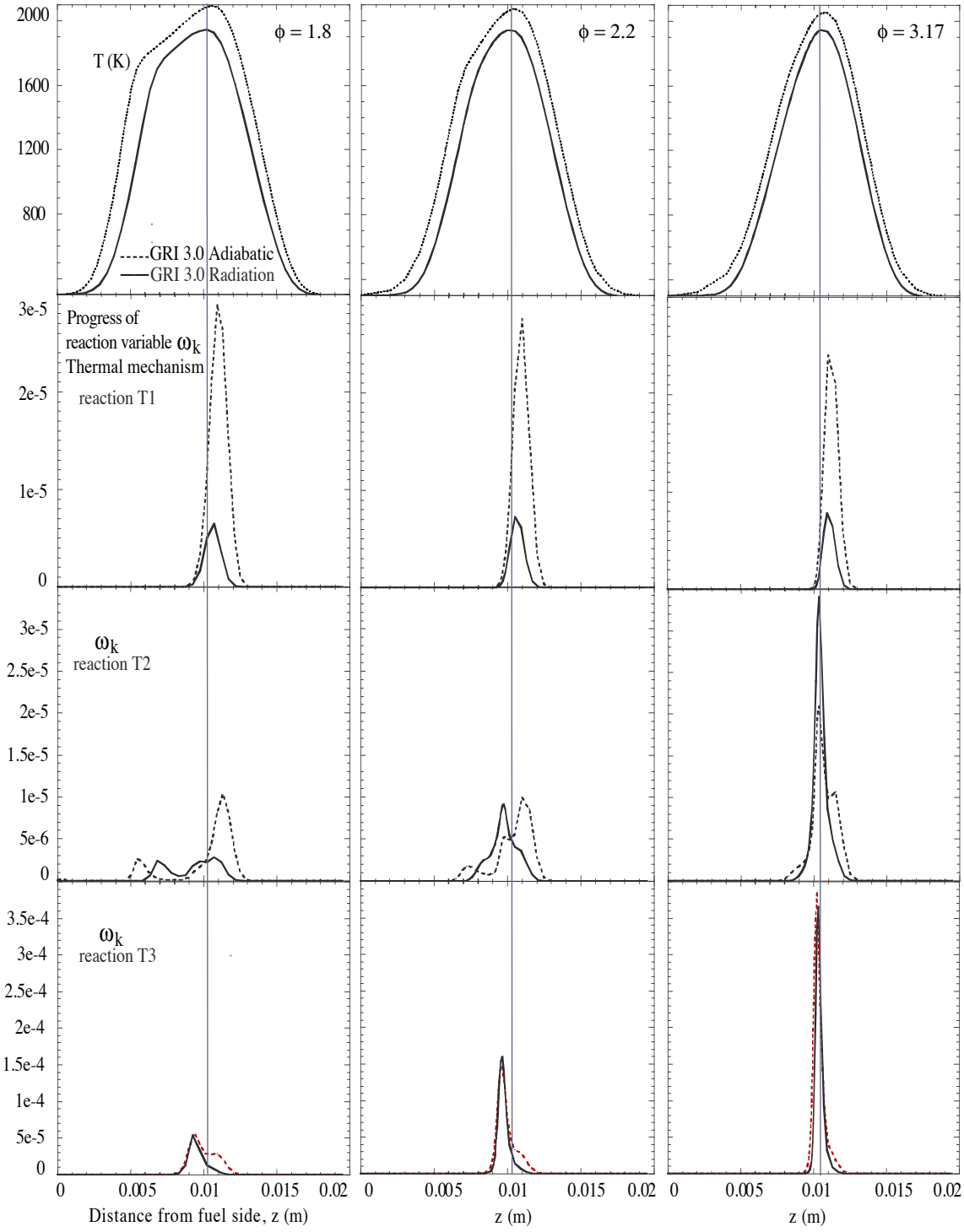

Figure 37. Progress of reaction variables for NO thermal reaction mechanism. Vertical line marks the location of peak flame temperature. Numerical simulation Case (b), d=1.95 cm, varying ϕ.

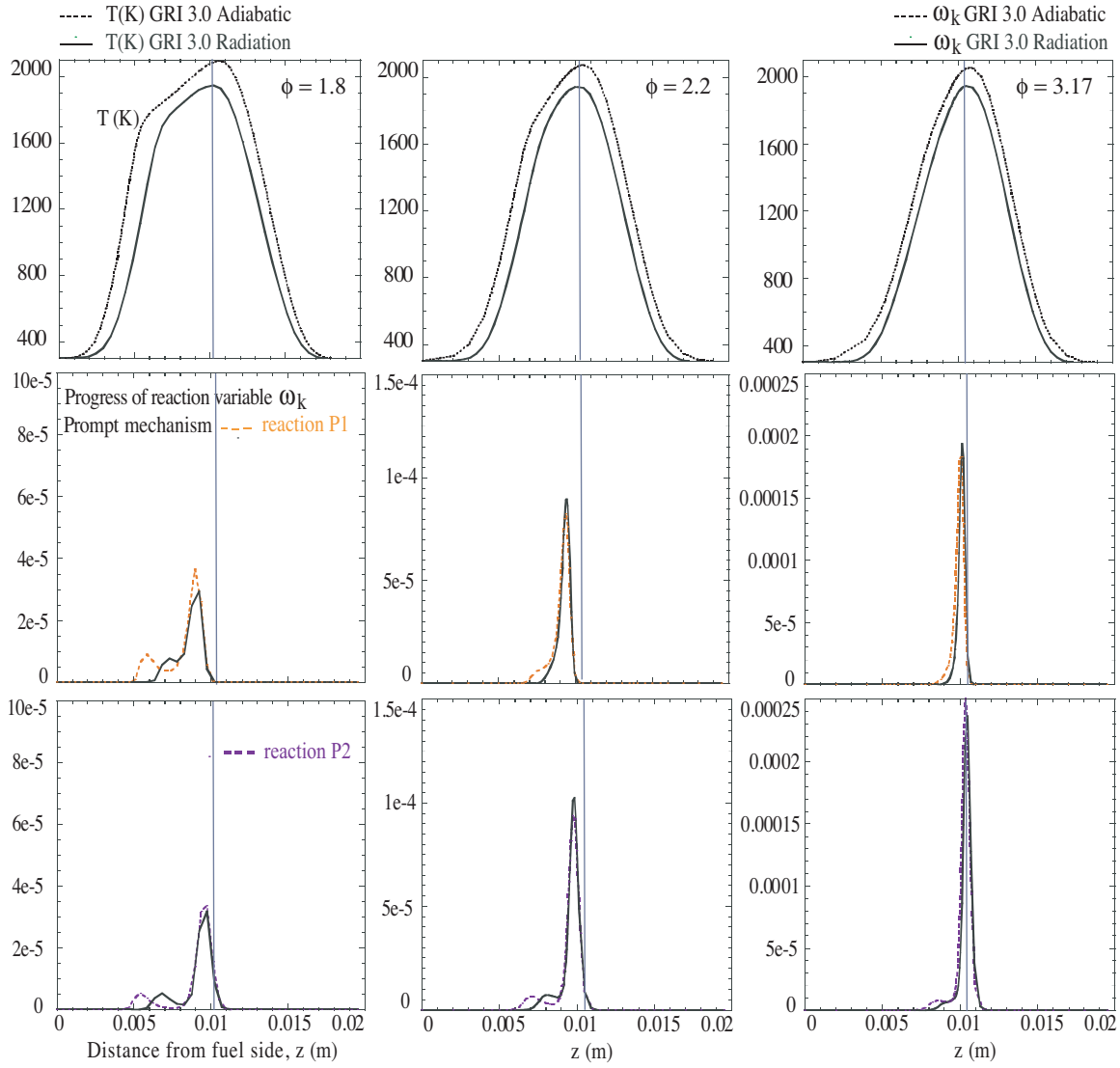

Figure 38. Progress of reaction variables for NO prompt mechanism. The vertical line marks the location of peak flame temperature. Case (b), d=1.95 cm, varying ϕ.

The prompt mechanism as described in Li and Williams (1999) takes two reactions to initiate the formation of NO:

$$N_2 + CH \leftrightarrows N + HCN \ (P1)$$

$$O + HCN \leftrightarrows H + NCO \ (P2)$$

The reaction rate or progress of reaction variable $\omega_k^{'}$, in kmol/m^{3}s, is plotted for each reaction forward. The prompt mechanism shown in figure 38 shows an increase with increasing equivalence ratio and the production peak moves closer to the main reaction zone. Noticeably, NO production shows a local maxima before the main reaction zone at low ϕ. The radiative calculations show a slight decrease in production rate.

Figure 39 shows the nitrous oxide reaction[5]:

$$N_2O + O \rightarrow 2NO$$

The reaction occurs in the lean side of the flame. The progress of reaction variable shows an increase with increasing ϕ and the radiative calculation conserve this trend.

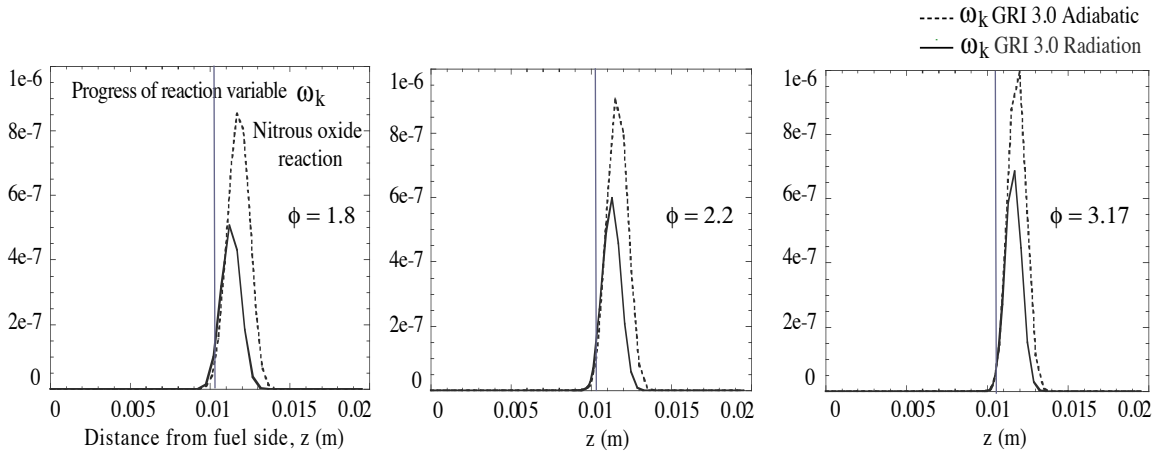

Figure 39. Progress of reaction variables for NO formation, Nitrous oxide mechanism. Case (b), d=1.95 cm, varying ϕ.

It is safe to conclude that the decrease in temperature affects the levels of NO in the flame mostly through the thermal (Zel'dovich) mechanism of NO formation. Confirming the findings of Zhu et al. (2002), NO mass fraction values are still over-

[5]Also not considered a principal mechanism in NO formation, it is included here to show the effect of radiation.

predicted for the richer flame (ϕ=3.17). Similarly, the CO mass fraction values are under-predicted for the richer flame, where the radiation model has stronger effect. The problem of over-prediction of NO has been attacked in a different manner by Sutton and Fleming (2008). By modifying GRI 3.0 to include intermediate reactions for a new prompt NO formation pathway, several reaction for NCN consumption were included. The simulations were performed for three different flames at lean, stoichiometric and rich ϕ. The results of the modified GRI 3.0 mechanism show little improvement from the original case, leaving the causality of the over-prediction unknown.

Although it is beyond the scope of the present work, it would be possible to investigate different Arrhenius coefficients for the reaction responsible for NO formation. The present work augmented the calculations with a radiation model, it is conceivable to improve and fine tune the reaction mechanism in the future.

To conclude, the software package with GRI 3.0 reaction mechanism is augmented with a radiation model based on RADCAL. The final simulations are in good agreement with experimental results, and the software might be use to confidently predict certain pollutants such as NO where they cannot be measured. The new results agree with the scientific community assumption (Zhu et al., 2002) that an optically-thin model is a reasonable assumption for thin laminar flames, a self-absorption model is unnecessary, but the radiative model provides better results. Questions remain about the under-prediction of intermediate species for richer flames.

Computation run time

The inclusion of the radiation treatment obviously increases run times compared to earlier computations. The increase in computational time is due two phenomena:

- The radiation model add to the complexity of the equation

- Grid refinement at low strain increases the computational time considerably, due to the thickness of the lean flame structure

A comparison of run time between different flames (Table VI) shows the richer flames run faster, or the solution is easier to find due to the thin or simple structure of the flame, but for lower strain or leaner flame at ϕ =1.8, the run times become considerably expensive. The grid refinement increased the computational time and for low strain flames convergence was not always achieved. For these flames, some adjustment to the initial grid was necessary to obtain more than 60 to 80 points in the solution. Indeed the solution for flames simulations are more expensive with the radiation treatment, but the run time is keep within one hour and still around 10 minutes for the richer flames. Thus the advantages of a radiation treatment as explained in the sections above are worth the penalty when considering industrial scale parametric variation with detailed chemistry for different combustion regimes.

Table VI. Computational time for adiabatic and radiative models. Simulation results from Case (b), d=1.95 cm. Computational time is shown in min, the number of grid point is shown in parenthesis

Simulation case	No Radiation	Radiation Model 2	Grid refinement
$\phi = 3.17$	4 min (41)	10 min (41)	no
$\phi = 3.17$	7 min (153)	49 min (68)	yes
$\phi = 1.8$	10 min (40)	68 min 41)	no

Dufour effect

After the Dufour effect is included in the calculations, the computational time is greatly increased (see table VIII on page 92) up to one hour for the lean flame. The

results both on the physical and scalar axis are negligible as can be seen in figure 40. Dufour effect is often neglected for this reason (Williams, 1985), the computational time is not worth the minor effect in partially premixed flames. This confirms the work of Ern and Giovangigli (1998) and the same outcome from hydrogen-oxygen counterflow-flames study by Ribert et al. (2008).

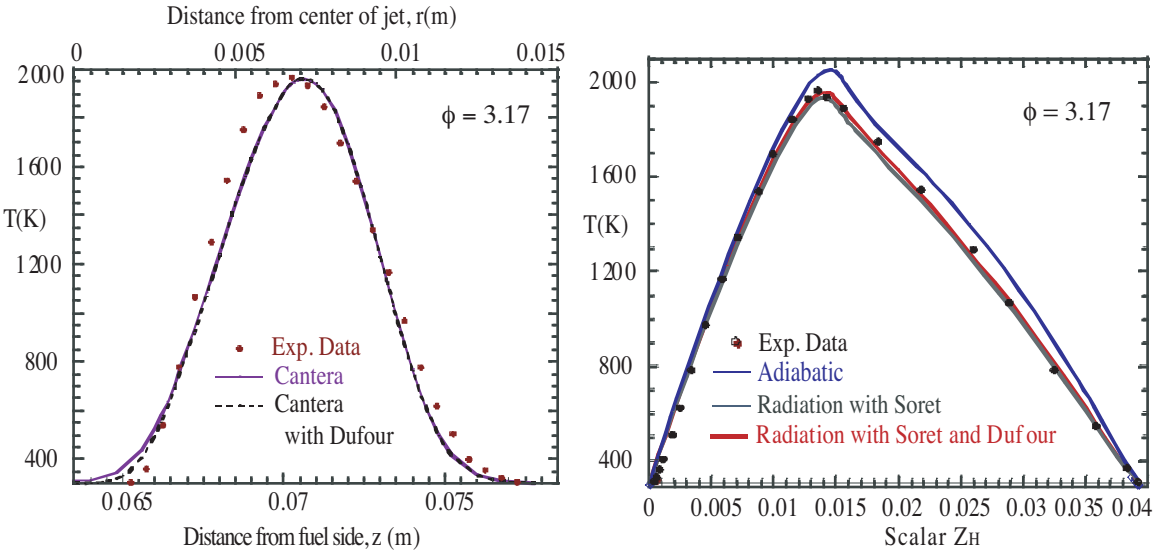

Figure 40. Simulation comparison with Dufour effect.

Soret effect

The Soret effect was examined for the three laminar partially premixed methane-air flame with equivalence ratios of 1.8, 2.2 and 3.17. When the temperature profile is plotted in physical space, very subtle changes in the flame structure are noticed. Contrary to the findings of Ern and Giovangigli (1998), the maximum temperature was unchanged. This might be attributed to the fact that the Ern and Giovangigli computations were adiabatic.

Since water and hydrogen have a large thermal diffusion coefficient, their mass fraction are plotted (figure 41) to observe the Soret effect on chemical composition. At lower equivalence ratio, water is slightly affected on the rich side. The profile is slightly thinner and the maximum of water mole fraction increased by 8 %. Species such as CO and NO also show a small change in mass fraction (figure 42) and their trends with varying ϕ are conserved.

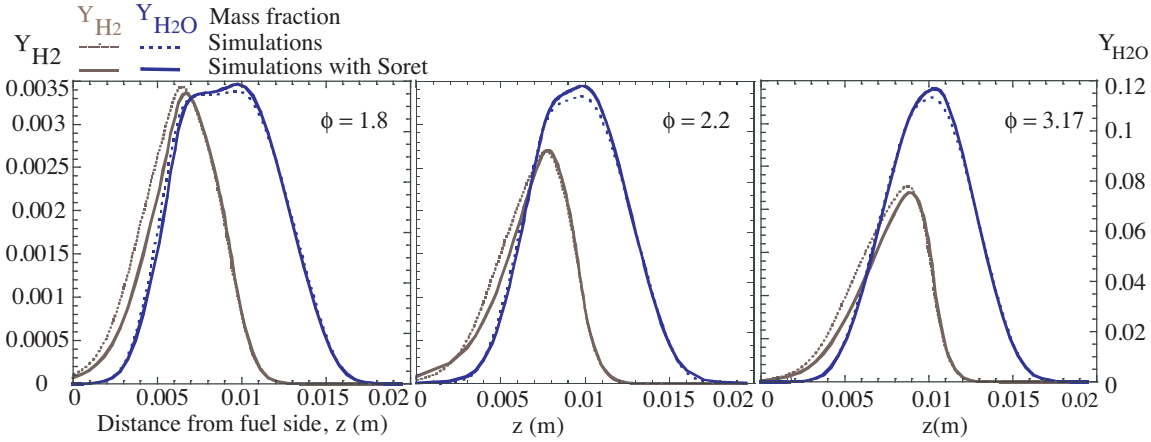

Figure 41. Soret effect on hydrogen species, water and hydrogen mole fraction.

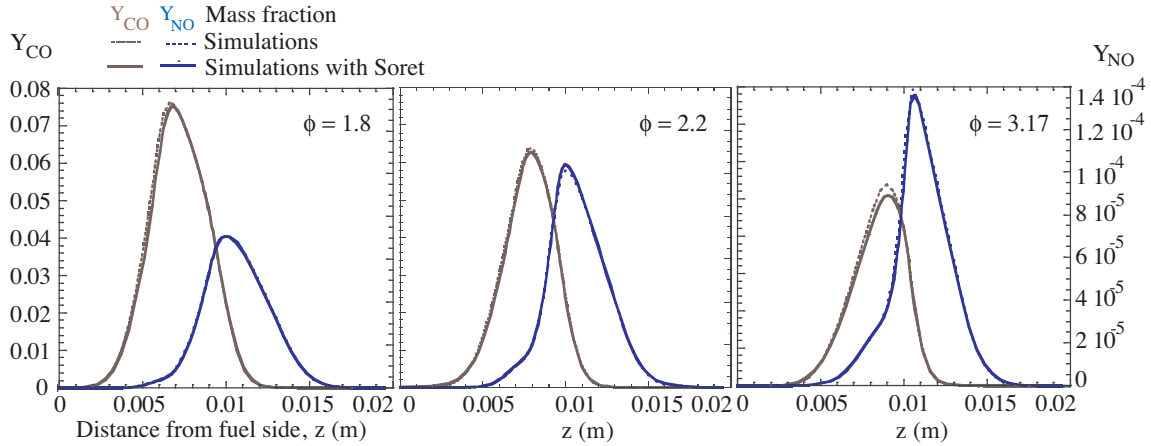

Figure 42. Soret effect on species CO and NO.

More interesting is the shift in hydrogen mass fraction profile on the rich side (figure 43). With the Soret effect hydrogen was reduced by 3.5 % (see Table **??**). The Soret effect is a combination of both the temperature gradient and the molecular weight of hydrogen as seen in the equations from chapter III:

$$\bar{\Gamma}_i = \rho Y_i \bar{V}_i$$

$$\bar{V}_i = \frac{1}{X_i \overline{MW}_i} \sum_{j \neq i}^{N} MW_i D_{i,j} \nabla X_i - \frac{1}{\rho T} \frac{D_{T,i}}{Y_i} \frac{\nabla T}{T} \tag{5.10}$$

where the first term is the multi-component diffusion and the second term represents the Soret effect. While the temperature gradient is steeper on the rich side of the second zone (figure 43), the Soret term will become more important. Mass diffusion of hydrogen and the temperature gradient are combined in this region (both terms in equation 5.10 have identical signs) thus the Soret effect is a co-gradient to Fick diffusion. While the temperature gradient is smaller on the right of the second zone, closer to the maximum temperature, the Soret effect will be smaller too. Mass diffusion of hydrogen in that region actually counteracts the temperature gradient. Because the Soret term is less the effect is not as effective as on the rich side and no noticeable change in hydrogen mass fraction is seen.

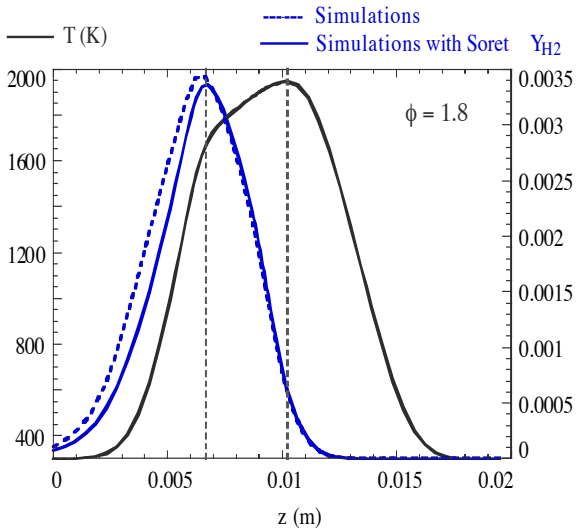

Figure 43. Soret effect on the hydrogen mass fraction.

This effect seems negligible, but when the scalar Z_H is plotted in physical and scalar space (figure 44 and 45) the change in hydrogen values has a clear effect. For the case of $\phi = 1.8$ especially, on the rich side, the curvature is reduced and the problem that would arise with double value of Z_H is avoided. Figure 44 shows in detail the value of scalar Z_H changing to a monotonic curve after the Soret effect is included. For each value of Z_H there is only one value of temperature. After the inclusion of the higher order term, the relationship between Z_H and the temperature profile is finally a one-to-one mapping, a valid flamelet.

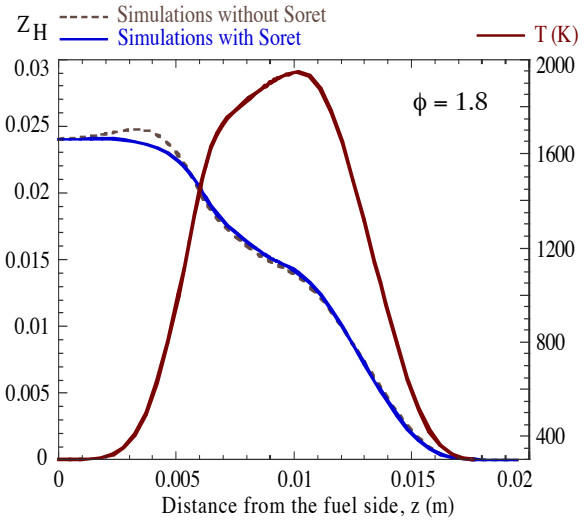

Figure 44. Soret effect on the scalar Z_H, physical space.

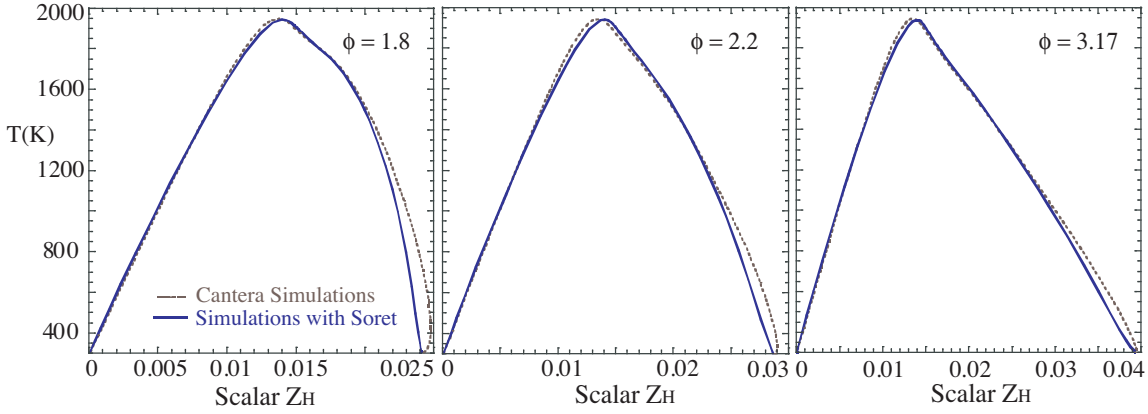

Figure 45. Soret effect on the scalar structure.

Table VII. Effect of cross-transport terms on species H_2, CO, and NO. Simulations results. Percentage difference of mole fraction at maximum value

Intermediate species	H_2	CO	NO
$\phi = 3.17$	-3.5%	-5.3%	-2.1%
$\phi = 2.2$	-0.1%	-2.4%	-1.9%
$\phi = 1.8$	-2%	-1.9%	+0.5%

Table VIII. Computational time for different transport models

Simulation case	Radiation	Radiation and Soret	Radiation, Soret and Dufour	Grid refinement
$\phi = 3.17$	6 min (51)	4 min (51)	11 min(51)	no
$\phi = 3.17$	14 min, 5min (172)	29 min, 21min (172)		yes
$\phi = 2.2$	9 min (51)	16 min (51)	54 min(51)	no
$\phi = 1.8$	6 min, 12s (41)	7 min, 1min 41)	56 min (51)	no

Computation run time

The multi-component transport increases computational time. Table VIII shows a comparison of simulations with and without the multi-component transport and the Soret option. The total time followed by the multi-component-transport fraction of computational time are indicated. The number of grid points in the solution is shown in parenthesis. Run times are doubled when grid refinement is used. The multi-component transport option takes 37 % more time of the total computation with Soret included. When the grid is fixed, run time barely increases. Only for lower strain flames, when ϕ decreases, it becomes noticeable. In this case the computational time increases by 16 % and the contribution of multi-component transport with Soret is increased by 11 %. De Charentenay and Ern (2002) report a contribution of 3 % to the overall CPU time but does not specify the total increase in CPU time due

to the inclusion of multi-component model on H_2-O_2 turbulent flames. With only this information, the increase seems comparable. For the present work the relative computational time expense is judged reasonable since most computation falls well within one hour and parametric variations are needed.

Scalar axis: comparison between experiments and simulations

The comparison on the scalar axis between the experimental laminar flames and the opposed jet simulations yields very good results. The temperature profile can be match precisely and the species profile too. This was possible with simulations case (b) and case (c). A complete series of graph is included in Appendix A. Graphs for all species (from experiments evaluation) and temperature are plotted for case (c). The effect of partial premixing on the flame structure can be analyzed with a parametric variation of the equivalence ratio ϕ. More importantly the formulation of the flamelet with a primitive scalar enables a clear visualization of the second reaction zone in the rich side of the partially premixed flame. Both the experiments and simulations temperature flamelets show this results. The discussion of the reaction responsible for the second reaction zone started in the present work may lead to future research with the new and future computations.

CHAPTER VI

CONCLUSIONS

Through the combination of previously unpublished data with simulations including detailed reaction mechanism and full transport scheme, the flame structure was compared in both physical and scalar space.

- The experimental data set is a series of single-point multi-scalar measurements which include nine species and temperature. They validated the 1-D simulations performed with the Cantera software package.

- The advantage of the numerical simulations relies in the detailed-chemistry kinetics which gives access to 53 species and 325 reactions.

- The computations are augmented to include a radiation treatment for an optically-thin model. Two models were tested here, a model similar to RADCAL was finally implemented. Radiative heat flux was characterized and the emission of the following species taken into account: CH_4, H_2O, CO_2 and CO. Adiabatic and radiative calculations were compared to each other. The radiation model affect maximum flame temperature as well as the whole flame profile. Species concentrations such as CO and NO are also affected. The NO production is reduced through the thermal mechanism. NO mass fraction is adequately predicted at low equivalence ratios with the radiative Cantera but still over-predicted at higher equivalence ratios. Nonetheless the decreasing trend in NO mass fraction with decreasing ϕ shown by the experiments is captured with the adiabatic and radiative computations. In the same manner, the counter-intuitive trend of decreasing CO mass fraction as the flame becomes richer is observed in both

experiments and computations. In summary, the radiative calculations capture most of the trends observed in experiments in a more precise manner than the adiabatic calculations.

- As past studies have shown cross-transport effects such as Soret and Dufour may be important in certain flames. The inclusion of both cross-transport terms in the calculations shows that only the Soret effect, i.e. temperature gradient giving rise to mass flux, is important. The Dufour term, i.e. concentration gradient giving rise to heat flux, has no results on the flame structure or species concentrations in the flames studied here. The Soret effect is noticeable in the rich zone of the flames due to a combination of reasons: large temperature gradients; low molecular weights; the relatively high concentration of hydrogen molecules; and large thermal diffusion coefficients. Even though the Soret term is proven to be rather small, it has a profound effect on the spatial profile of the conserved scalar through the hydrogen mass fraction. Specifically, the presence of cross-transport makes the conserved scalar behavior monotonic and allows for a unique one-to-one flamelet mapping transformation.

- A single-element mass fraction, namely Z_H, was chosen as the conserved scalar. The present study differs from past research by the fact that the scalar was not normalized. This primitive scalar actually produces a better flamelet mapping, and allows for the identification of the flame scalar structure. A second premixed zone can be discerned in the partially premixed flame structure by examination of both major and intermediate species scalar profiles such as CO, H_2 and H_2O.

- The 1-D opposed jet flame calculations give very good and fast comparison to the axisymmetric flame experimental results in scalar space. Nevertheless the comparison between experiments and simulations in physical space proves to

be difficult and incomplete. The differences are attributed to the inherent 2-D nature of the axisymmetric flames. Solving the problem in 2-D requires either a full solution to the 2-D equations -which is time consuming and involves a reduced mechanism- or a boundary-layer approximation solution using detailed chemistry. In the latter, axial diffusion would be neglected compared to axial convection and a computational scheme would resolve the problem in 2-D. This is an exciting potential route for future research.

REFERENCES

Aggarwal, S., Puri, I., and Qin, X. (2001) A numerical and experimental investigation of "inverse" triple flames. *Physics of Fluids*, **13**, 265.

Arias-Zugasti, M. and Rosner, D.E. (2008) Soret transport, unequal diffusivity, and dilution effects on laminar diffusion flame temperatures and positions. *Combustion and Flame*, **153**, 33.

Arrighetti, C., Cordiner, S., and Mulone, V. (2007) Heat and mass transfer evaluation in the channels of an automotive catalytic converter by detailed fluid-dynamic and chemical simulation. *Journal of Heat Transfer*, **129**, 536.

Barlow, R., Frank, J., Karpetis, A., and Chen, J.Y. (2005) Piloted methane/air jet flames: Transport effects and aspects of scalar structure. *Combustion and Flame*, **143**, 433.

Barlow, R., Karpetis, A., Frank, J., and Chen, J.Y. (2001) Scalar profiles and no formation in laminar opposed-flow partially premixed methane/air flames. *Combustion and Flame*, **127**, 2102.

Barlow, R.S., Fiechtner, G.J., Carter, C.D., and Chen, J.Y. (2000) Experiments on the scalar structure of turbulent CO/H2/N2 jet flames. *Combustion and Flame*, **120**, 549.

Benezech, L.J.M. (2006) *Experimental investigation of planar strained methane-air and ethylen-air flames*. M.S., California Institute Of Technology.

Bennett, B., McEnally, C., Pfefferle, L., and Smooke, M. (2000) Computational and experimental study of axisymmetric coflow partially premixed methane/air flames. *Combustion and Flame*, **123**, 522.

Berg, P., Hill, D., Noble, A., Smith, G., Jeffries, J., and Crosley, D. (2000) Absolute CH concentration measurements in low-pressure methane flames: comparisons with model results. *Combustion and Flame*, **121**, 223.

Bergthorson, J. and Dimotakis, P. (2007) Premixed laminar C1-C2 stagnation flames: Experiments and simulations with detailed thermochemistry models. *Proceedings of the Combustion Institute, University of Heidelberg, Germany*, **31**, 1139.

Bergthorson, J., Goodwin, D., and Dimotakis, P. (2005a) Particle streak velocimetry and CH laser-induced fluorescence diagnostics in strained, premixed, methane-air flames. *Proceedings of the Combustion Institute, Orlando, FL*, **30**, 1637.

Bergthorson, J., Sone, K., Mattner, W., Dimotakis, P., Goodwin, D., and Meiron, D. (2005b) Impinging laminar jets at moderate Reynolds numbers and separation distances. *Physical Review E*, **72**.

Bergthorson, J.M. (2005) *Experiments and modeling of impinging jets and premixed hydrocarbon stagnation flames*. Ph.D. thesis, California Institute Of Technology.

Bilger, R. (1976a) The structure of diffusion flames. *Combustion Science and Technology*, **13**, 155.

Bilger, R. (1976b) Turbulent jet diffusion flames. *Prog. Energy Combustion Science*, **1**, 87.

Bilger, R. (2000) Future progress in turbulent combustion research. *Progress in Energy and Combustion Science*, **26**, 367.

Bilger, R., Starner, S., and Kee, R. (1990) On reduced mechanisms for methane air combustion in nonpremixed combustion. *Combustion and Flame*, **80**, 135.

Blanquart, G., Pepiot-Desjardins, P., and Pitsch, H. (2009) Chemical mechanism for high temperature combustion of engine relevant fuels with emphasis on soot precursors. *Combustion and Flame*, **156**, 588.

Brahmi, L., Vietoris, T., Torero, J.L., and Joulain, P. (1999) Estimation of boundary layer diffusion flame temperature by means of an infrared camera under micro-gravity conditions. *Measurement of Science Technology*, **10**, 859.

Burke, S. and Schumann, T. (1928) Diffusion flames. *Ind. Engin. Chem.*, **20**, 998.

Chapman, S. and Cowling, T. (1970) *The Mathematical Theory Of Non-uniform Gases*. Cambridge Unversity Press, Cambridge, UK.

Charest, M. (2008) Numerical study on the effect of gravity on flame shape and radiation in laminar diffusion flames. *Proceedings of the Combustion Institute, Ontario, Canada*, **33**, 84.

Chung, S.H. and Law, C. (1984) Burke-schumann flame with streamwise and preferential diffusion. *Combustion Science and Technology*, **37**, 21.

Daguse, T., Croonenbroek, T., Rolon, J.C., Darabiha, N., and Soufiani, A. (1996) Study of radiative effects on laminar counterflow H2/O2/N2 diffusion flames. *Combustion and Flame*, **106**, 271.

Datta, A., Beyrau, F., Seeger, T., and Leipertz, A. (2004) Temperature and CO concentration measurements in a partially premixed CH_4/air coflowing jet flame using coherent anti-Stokes Raman scattering. *Combustion Science and Technology*, **176**, 1965.

Davis, S., Law, C., and Wang, H. (1999) Propene pyrolysis and oxidation kinetics in a flow reactor and laminar flames. *Combustion and Flame*, **119**, 375.

De Charentenay, J. and Ern, A. (2002) Multicomponent transport impact on turbulent premixed H2/O2 flames. *Combustion Theory and Modelling*, **6**, 439.

Dworkin, S.B., Smooke, M.D., and Giovangigli, V. (2009) The impact of detailed multicomponent transport and thermal diffusion effects on soot formation in ethylene/air flames. *Proceedings of the Combustion Institute, McGill University, Montreal, Canada*, **32**, 1165.

Ern, A. and Giovangigli, V. (1998) Thermal diffusion effects in hydrogen-air and methane-air flames. *Combustion Theory and Modelling*, **2**, 349.

Gasnot, L., Desgroux, P., Pauwels, J., and Sochet, L. (1999) Detailed analysis of low-pressure premixed flames of CH4 + O2 + N2: a study of prompt-NO. *Combustion and Flame*, **117**, 291.

Giovangigli, V. (1999) *Multicomponent Flow Modelling*. Birkhauser, Boston, MA.

Glassman, I. (1996) *Combustion*. 3rd edition, Academic Press, New York, NY.

Goodwin, D.G. (2003) An open-source, extensible software suite for CVD process simulation. *Proceedings of CVD XVI and EuroCVD Fourteen, Electrochemical Society, Delft, The Netherlands*.

Gore, J. and Zhan, N. (1996) NOx emissions and major species concentrations in partially premixed laminar methane/air co-flow jet flames. *Combustion and Flame*, **105**, 414.

Grçar, J., Bell, J., and Day, M. (2008) The soret effect in naturally propagating premixed, lean hydrogen-air flames. *Technical Report LBNL-669E*, Lawrence Berkeley National Laboratory.

Grosshandler, W. (1993) A narrow-band model for radiation calculations in a combustion environment. *Technical note 1402*, NIST.

Grosshandler, W.L. (1990) Radiative heat transfer in non-homogeneous gas: a simplified approach. *International Journal of Heat Transfer*, **23**, 1447.

Hirschfelder, J.O., Curtiss, C.F., and Bird, R.B. (1954) *Molecular Theory of Gases and Liquids*. John Wiley & Sons, Inc, Hoboken, NJ.

Karpetis, A. and Barlow, R. (2003) Structure of laminar partially premixed jet flames. In *3rd U. S. National Combustion Meeting, Chicago IL*, Presentation.

Kee, R., Coltrin, M., and Glarborg, P. (2003) *Chemically Reacting Flow, Theory and Practice*. John Wiley & Sons, Inc, Hoboken, NJ.

Kee, R. and Miller, J. (1978) A split-operator, finite-difference solution for axisymmetris laminar-jet bidiffusion flames. *AIAA Journal*, **16**, 169.

Kee, R., Modak, A., and Delplanque, J. () A boundary-layer formulation for modeling steady-state, laminar, confined, co-flowing, axisymmetric, non-premixed flames, Colorado School of Mines, unpublished.

Kim, J., Libby, P.A., and Williams, F. (1992) On the displacement effects of laminar flames. *Combustion Science and Technology*, **87**, 1.

Kim, O.J., Gore, J.P., Viskanta, R., and Zhu, X.L. (2003) Prediction of self-absorption in opposed flow diffusion and partially premixed flames using a weighted sum of gray gases model (wsggm)-based spectral model. *Numerical Heat Transfer, Part A*, **44**, 335.

Kim, S.H., Kim, M., Yoon, Y., and Jeung, I.S. (2002) The effect of flame radiation on the scaling of nitrogen oxide emissions in turbulent hydrogen non-premixed flames. *Proceedings of the Combustion Institute, Sapporo, Japan*, **29**, 1951.

Kluzek, C., Karpetis, A.N., and Barlow, R.S. (2009) Scalar structure of laminar partially premixed flames. In *6th U.S. National Combustion Meeting*, Ann Arbor, MI, Presentation.

Law, C. (2005) *Combustion Physics*. Cambridge University Press, New York, NY.

Li, S.C. and Williams, F.A. (1999) Nox formation in two-stage methane-air flames. *Combustion and Flame*, **118**, 399.

Lyle, K., Tseng, L., Gore, J., and Laurendeau, N. (1999) A study of pollutant emission characteristics of partially premixed turbulent jet flames. *Combustion and Flame*, **116**, 627.

Masri, A.R., Dibble, R.W., and Barlow, R.S. (1996) The structure of turbulent non-premixed flames revealed by raman-rayleigh-lif measurements. *Progress in Energy and Combustion Science*, **22**, 307.

Minh, H., Bock, H., Tisher, S., and Deutshmann, O. (2008) Fast solution for large-scale 2-d convection-diffusion reacting flows. In *ICCSA*, 1121–1130, University of Karlsruhe, Germany.

Mueller, M., Blanquart, G., and Pitsch, H. (2009) Hybrid method of moments for modeling soot formation and growth. *Combustion and Flame*, **156**, 1143.

Mungekar, H. and Atreya, A. (2006) Flame radiation and soot emission from partially premixed methane counterflow flames. *Journal of Heat Transfer*, **128**, 361.

Palle, S., Nolan, C., and Miller, R. (2005) On molecular transport effects in real gas laminar diffusion flames at large pressure. *Physics of Fluids*, **17**, 103601.

Pepiot-Desjardins, P., Pitsch, H., Malhotra, R., Kirby, S.R., and Boehman, A.L. (2008) Structural group analysis for soot reduction tendency of oxygenated fuels. *Combustion and Flame*, **154**, 191.

Peters, N. (1984) Laminar diffusion flamelet models in non-premixed turbulent combustion. *Prog. Energy Combustion Science*, **10**, 319.

Peters, N. (1988) Laminar flamelet concepts in turbulent combustion. *Symposium (International) on Combustion*, **21**, 1231.

Peters, N. (1998) *Fifteen lecture on laminar and turbulent combustion*. RWTH Aachen, Aachen, Germany.

Peters, N. (2000) *Turbulent Combustion*. Cambridge University Press, Cambridge, UK.

Pillier, L., El Bakali, A., Mercier, X., Rida, A., Pauwels, J., and Desgroux, P. (2005) Influence of C2 and C3 compounds of natural gas on NO formation: an experimental study based on LIF/CRDS coupling. *Proceedings of the Combustion Institute, University of Illinois at Chicago, IL*, **30**, 1183.

Pitsch, H. and Peters, N. (1998) A consistent flamelet formulation for non-premixed combustion considering differential diffusion effects. *Combustion and Flame*, **114**, 26.

Pitsch, H., Riesmeier, E., and Peters, N. (2009) Unsteady flamelet modeling of soot formation in turbulent diffusion flames. *Combustion Science and Technology*, **158**, 389.

Pitsch, H. and Steiner, H. (2000) Large-eddy simulation of a turbulent piloted methane/air diffusion flame (Sandia flame D). *Physics of Fluids*, **12**, 2541.

Plessing, T., Terhoeven, P., Peters, N., and Mansour, M. (1998) An experimental and numerical study of a laminar triple flame. *Combustion and Flame*, **115**, 335.

Qin, X., Choi, C., Mukhopadhyay, A., Puri, I., Aggarwal, S., and Katta, V.R. (2004) Triple flame propagation and stabilization in a laminar axisymmetric jet. *Combustion Theory and Modelling*, **8**, 293.

Ravikrishna, R. and Laurendeau, N. (2003) Evaluation of nitric oxide kinetics in high-pressure flames (up to 5 atm). *Journal of Power and Energy*, **217**, 529.

Ribert, G., Zong, N., Yang, V., Pons, L., Darabiha, N., and Candel, S. (2008) Counterflow diffusion flames of general fluids: Oxygen/hydrogen mixtures. *Combustion and Flame*, 319.

Rightley, M. and Williams, F. (1997) Structure of CO diffusion flames near extinction. *Combustion Science and Technology*, **125**, 181.

Rosner, D. (1986) *Transport Processes in Chemically Reacting Flow Systems*. Butterworth-Heinemann, Boston, MA.

Rosner, D. and Gomez, A. (1993) Thermophoretic effects on particles in the counterflow laminar diffusion flames. *Combustion Science and Technology*, **89**, 335.

Rosner, D., Israel, R., and Mantia, B.L. (2000) Heavy species Ludwig-Soret transport effects in air-breathing combustion. *Combustion and Flame*, **123**, 547.

Seshadri, K. and Peters, N. (1990) The inner structure of methane—air flames. *Combustion and Flame*, **81**, 96.

Shields, E. (2007) *Performance Modeling of a H2 fueled proton exchange membrane fuel cell*. M.S., University of Maryland.

Smith, G., Golden, D., Frenklach, M., Moriarty, N., Eiteneer, B., Goldenberg, M., Bowman, C., andW.C. Gardiner, R.H., Lissianski, V., and Qin, Z. (Accessed July 2008) GRI-Mech web site.
URL: http://www.me.berkeley.edu/gri-mech

Smith, N., Gore, J., Kim, J., and Tang, Q. (Accessed November 2008) TNF radiation models.
URL: http://www.ca.sandia.gov/TNF/radiation.html

Smooke, M.D., Xu, Y., Zurn, R.M., Lin, P., Frank, J.H., and Long, M.B. (1992) Computational and experimental study of oh and ch radicals in axisymmetric laminar diffusion flames. *Symposium (International) on Combustion*, **24**, 813.

Sung, C.J., Wang, H., and Law, C.K. (1996) On the structure of nonsooting counterflow ethylene and acetylene diffusion flames. *Combustion and Flame*, **107**, 321.

Sutton, J. and Fleming, J. (2008) Towards accurate kinetic modeling of prompt no formation in hydrocarbon flames via the ncn pathway. *Combustion and Flame*, **154**, 630.

Van Essen, W., Sepman, A., Mokhov, A., and Levinsky, H. (2007) The effects of burner stabilization on fenimore NO formation in low-pressure, fuel-rich premixed CH4/O2/N2 flames. *Proceedings of the Combustion Institute, University of Heidelberg, Germany*, **31**, 329.

Vincenti, W. and Kruger, C. (1965) *Introduction to Physical Gas Dynamics*. John Wiley & Sons, Inc, Hoboken, NJ.

Vranos, A. and Hall, R.J. (1993) Influence of radiative loss on nitric oxide formation in counterflow diffusion flames at high pressure. *Combustion and Flame*, **93**, 230.

Westbrook, C. and Dryer, F. (1981) Simplified mechanism for the oxidation of hydrocarbon fuels in flames. *Combustion Science and Technology*, **27**, 31.

Williams, B. and Fleming, J. (2007) Experimental and modeling study of NO formation in 10 torr methane and propane flames: Evidence for additional prompt-NO precursors. *Proceedings of the Combustion Institute, University of Heidelberg, Germany*, **31**, 1109.

Williams, F. (1985) *Combustion Theory*. 2nd edition, Benjamin/Cummings, Menlo Park, CA.

Williams, F. (Accessed March 2008) Chemical mechanisms for combustion applications, Center for Energy Research (Combustion Division).
URL: http://maeweb.ucsd.edu/ combustion/cermech/

Xue, H. and Aggarwal, S. (2001) Effect of reaction mechanisms on structure and extinction of partially premixed flames. *AIAA Journal*, **39**, 637.

Yamaoka, I. and Tsuji, H. (1974) Flame structure of rich methane-air counterflow flame. *Proceedings of the Combustion Institute, Tokyo, Japan*, 843.

Yamaoka, I. and Tsuji, H. (1976) Flame structure of rich methane-air counterflow flame. *Proceedings of the Combustion Institute, Massachusetts Institute of Technology, Boston, MA*, 1145.

Zhu, X., Gore, J., Karpetis, A., and Barlow, R. (2002) The effects of self-absorption of radiation on an opposed flow partially premixed flame. *Combustion and Flame*, **129**, 342.

APPENDIX A

FLAMES PROFILES IN SCALAR AND PHYSICAL SPACE

A.1 Flame profiles: comparison in physical space

Comparison of numerical simulations with experimental data. The measurements from Sandia Nat'l Labs constitute of the temperature flame profile and mass fraction profiles for 9 species ($CH_4, N_2, O_2, CO, CO_2, H_2O, H_2, OH, NO$) at 25 mm above nozzle exit. The simulation results are from case (c), d= 8 cm, varying ϕ, low strain rate $a \sim 14$. The results are plotted with respect to the physical space, the top x-axis for the experimental data and the bottom x-axis for the simulation results. The first figure A.1 shows the comparison of temperature profiles for all three ϕ and the error bars or RMS values of the experiment's temperature profile.

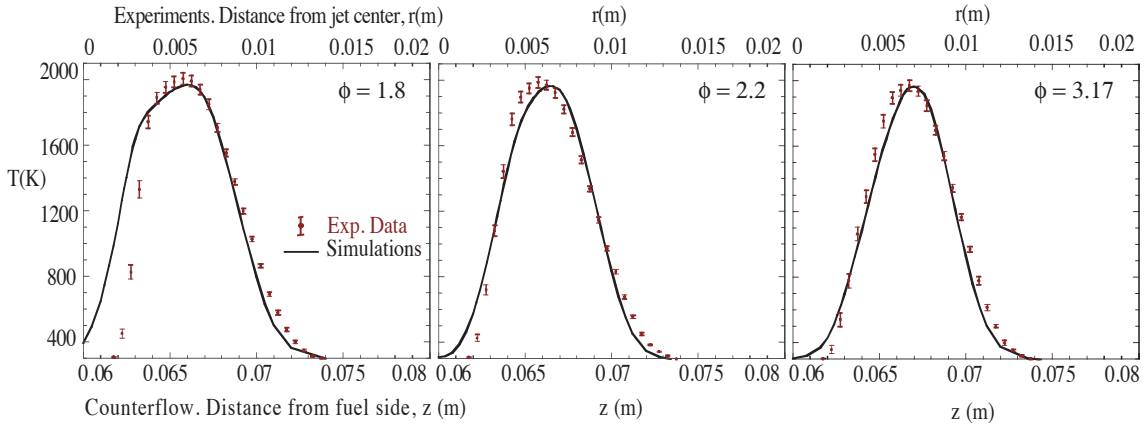

Figure A.1. Comparison of experimental data with simulations temperature profiles in physical space. Experimental results are plotted with error bars.

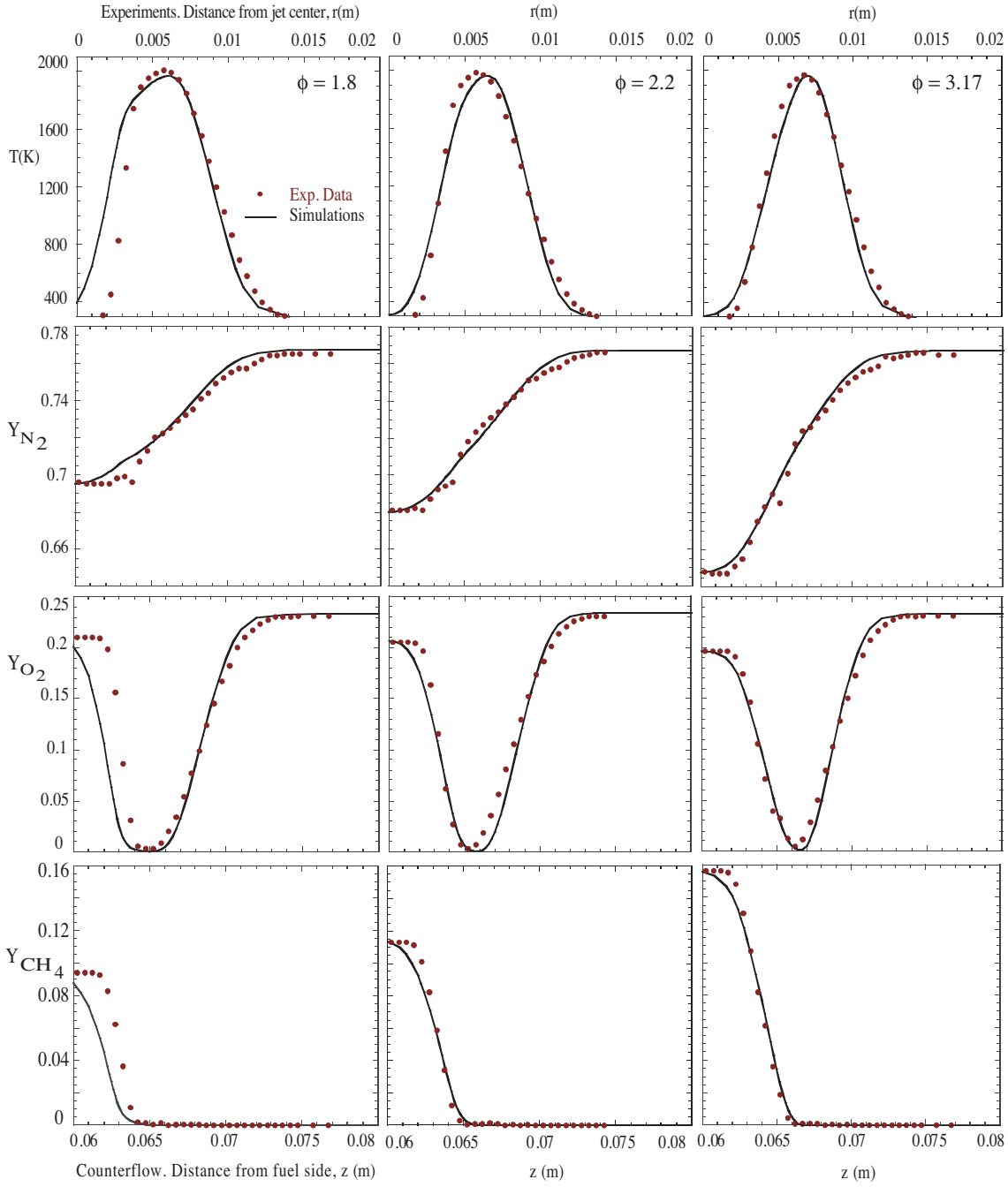

Figure A.2. Species N_2, O_2, CH_4 mass fractions, and temperature in physical space.

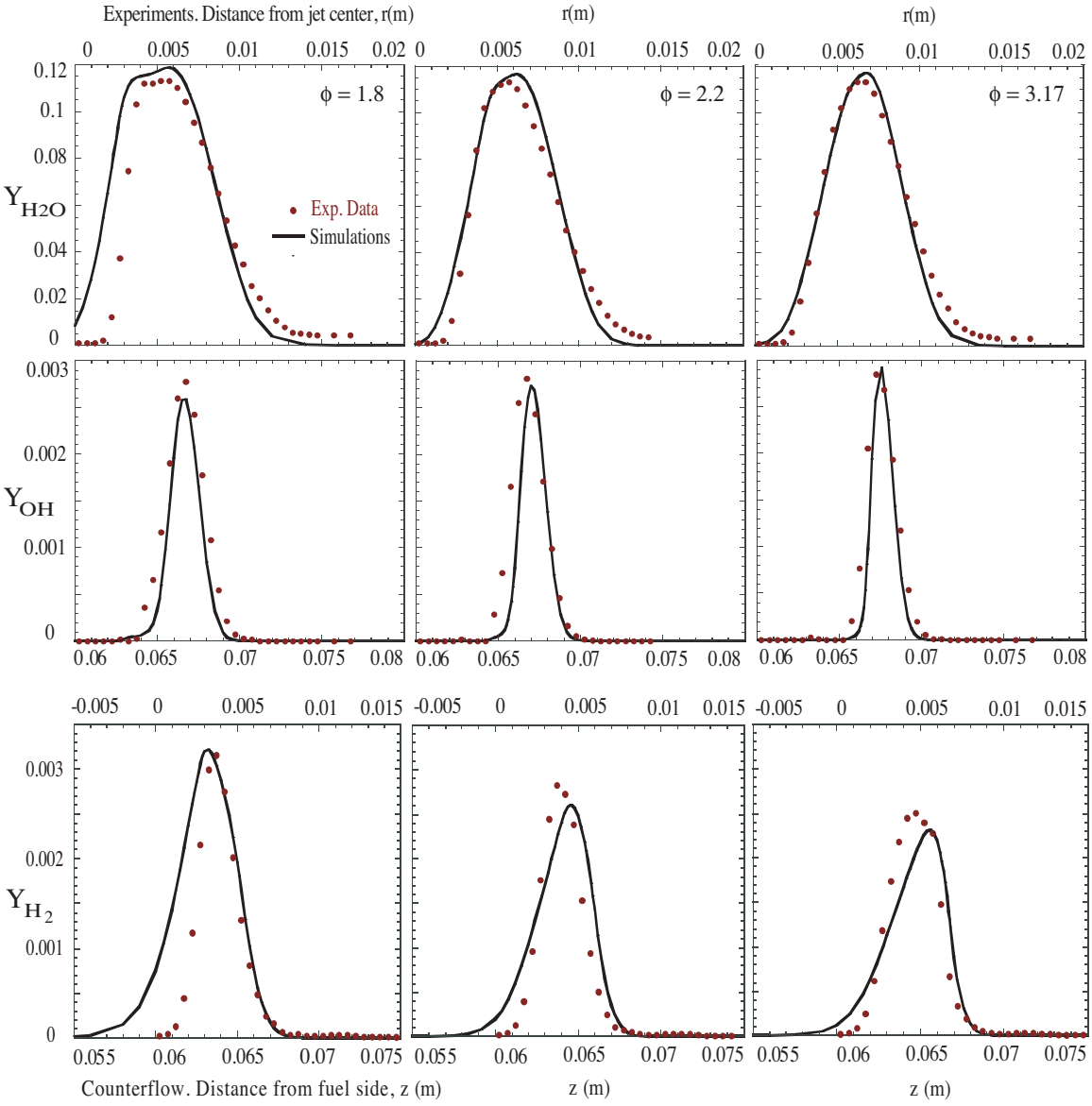

Figure A.3. Species H_2O, OH, H_2 mass fractions in physical space.

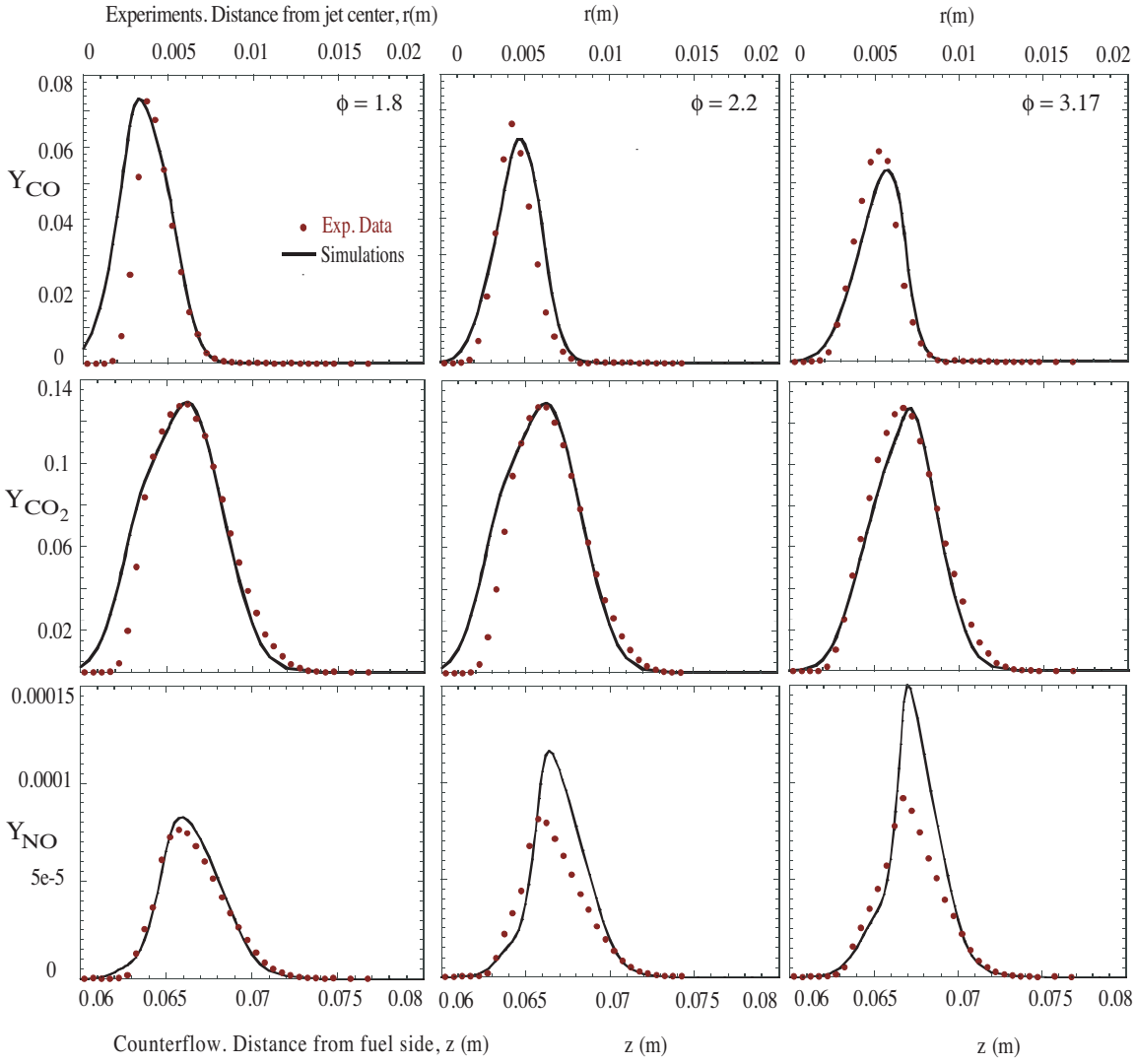

Figure A.4. Species CO, CO_2, NO mass fractions in physical space.

A.2 Flame profiles: comparison in scalar space

Comparison of numerical simulations with experimental data. The measurements from Sandia Nat'l Labs constitute of the temperature flame profile and mass fraction profiles for 9 species $CH_4, N_2, O_2, CO, CO_2, H_2O, H_2, OH, NO$ at 25 mm above nozzle exit. The simulation results are from case (c), d= 8 cm, varying ϕ, low strain rate

$a \sim 14$.

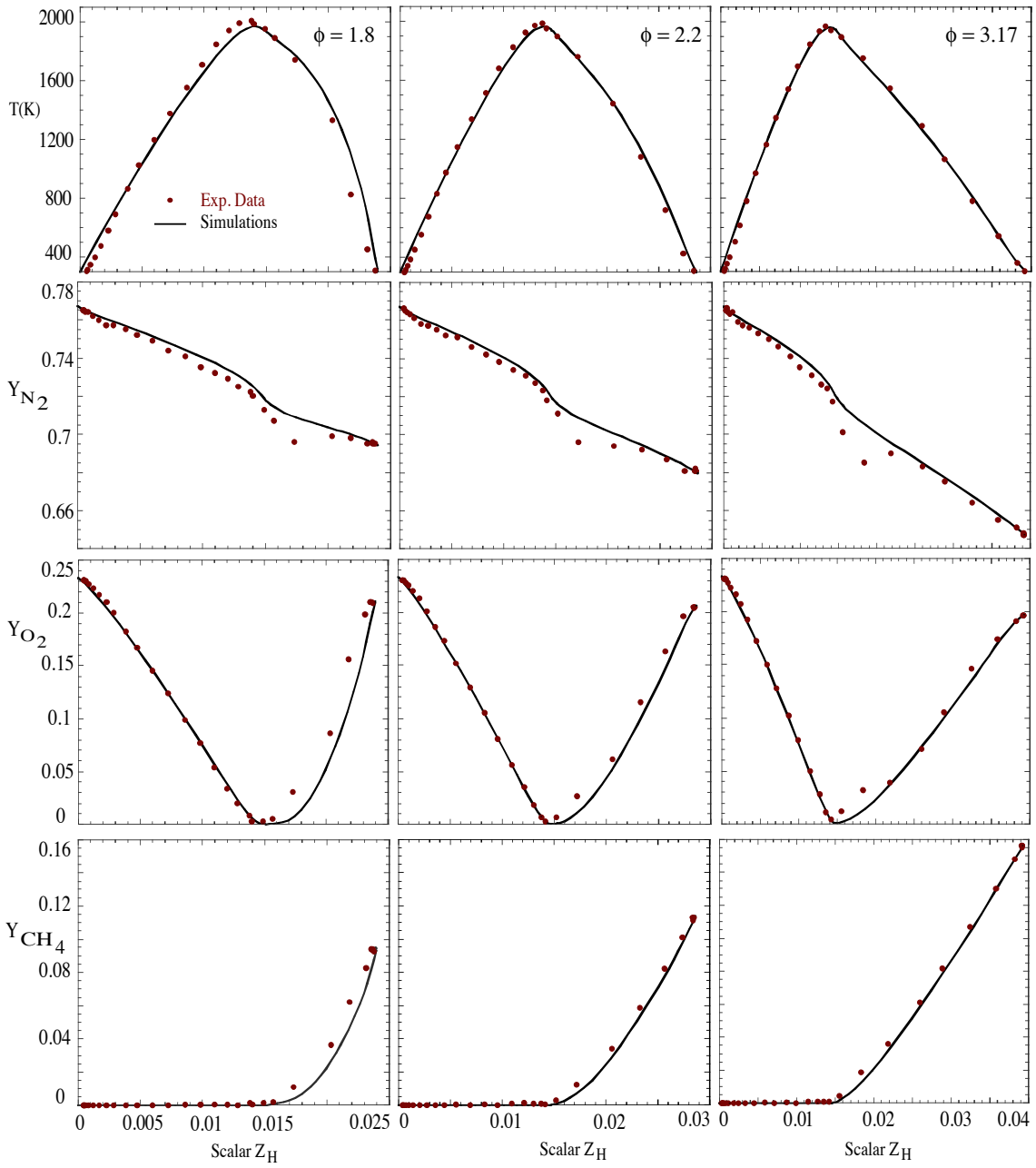

Figure A.5. Species and temperature in scalar space. Major species mass fractions are plotted under the temperature profiles with respect to the scalar Z_H.

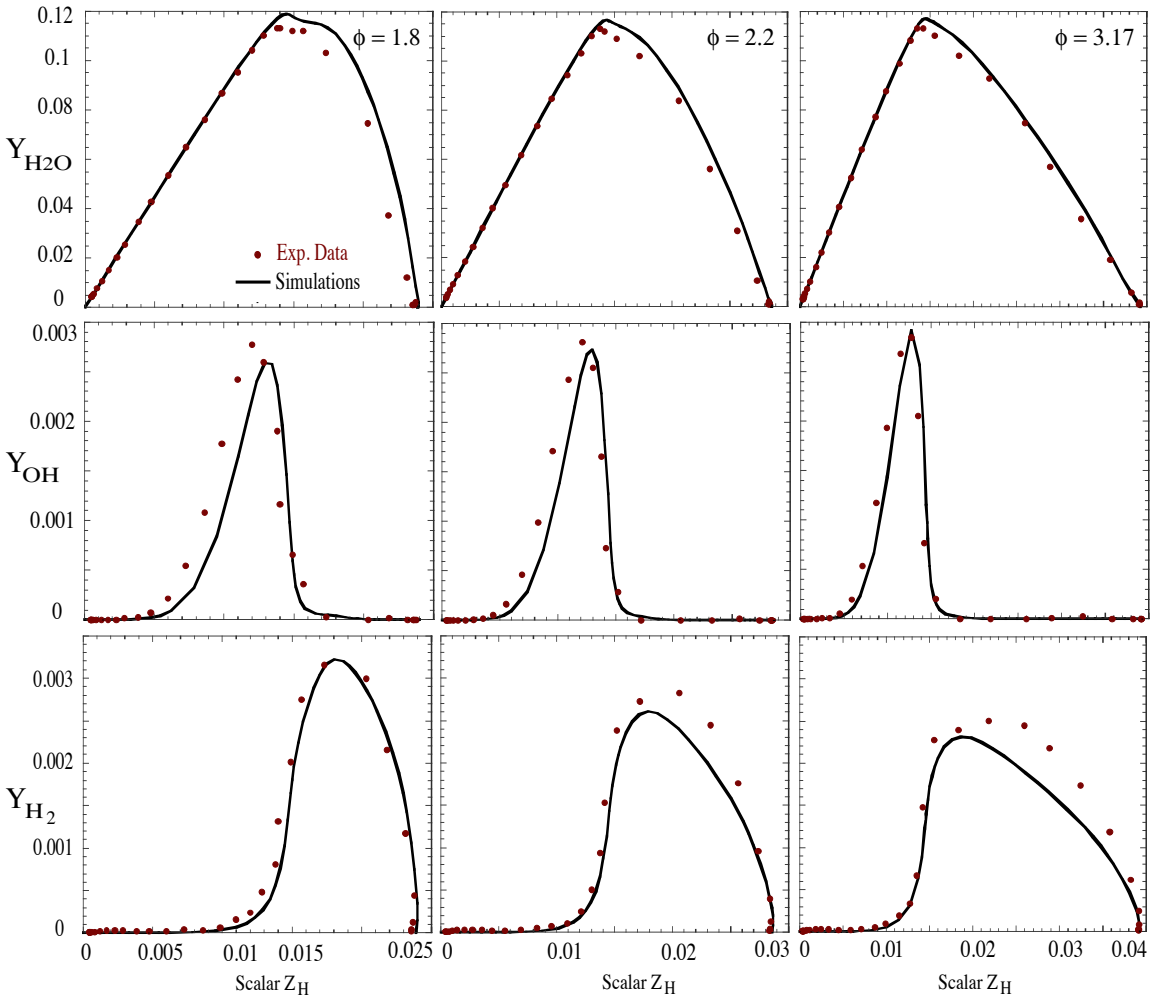

Figure A.6. Species H_2O, H_2, OH mass fractions in scalar space.

A.3 Reaction rate for CO and NO in scalar space

The simulation results presented here are from case (c), d= 8cm, varying ϕ, low strain rate $a \sim 14$.

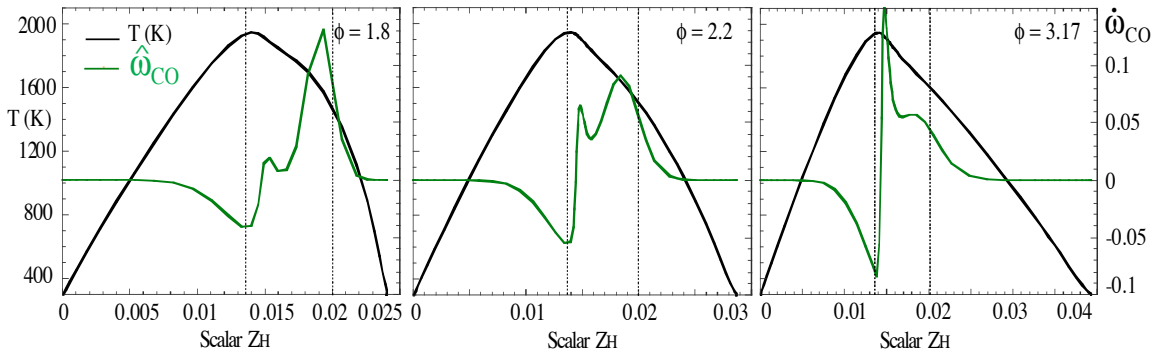

Figure A.7. Effect of radiation model on intermediate species: net molar production/destruction rate of CO in scalar space

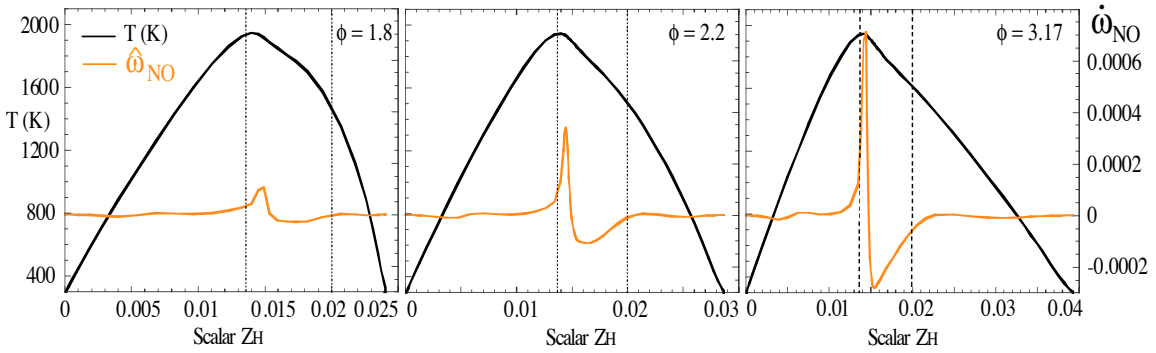

Figure A.8. Effect of radiation model on intermediate species: net molar production/destruction rate of NO in scalar space

VITA

Celine Delphine Kluzek

Contact address: Texas A&M University, Department of Aerospace Engineering
H.R. Bright Building, Rm. 701, TAMU 3141
College Station, TX 77843-3141

Email address: celinekluzek@mac.com

Web-site: http://flight.tamu.edu/personnel/index-pilots.html

Education: B.S. Aeronautical Science, Florida Instiute of Technology, 2001
M.S. Aeronautical Engineering, Purdue University, 2004